C

35

NASA CR-54569
FEBRUARY 1968
Allison EDR 5658

Single-Stage Experimental Evaluation of Boundary Layer Bleed Techniques for High Lift Stator Blades

I - Compressor Design

Prepared for

NATIONAL AERONAUTICS AND SPACE ADMINISTRATION

Contract NAS3-7900

N68-28621
(ACCESSION NUMBER)
105
(PAGES)
CR-54569
(NASA CR OR TMX OR AD NUMBER)
(THRU)
1
(CODE)
01
(CATEGORY)
FACILITY FORM 602

JUL 1968
RECEIVED
NASA STI FACILITY
INPUT BRANCH

Allison Division • General Motors

Indianapolis, Indiana

NOTICE

This report was prepared as an account of Government sponsored work. Neither the United States, nor the National Aeronautics and Space Administration (NASA), nor any person acting on behalf of NASA:

A. Makes any warranty or representation, expressed or implied, with respect to the accuracy, completeness, or usefulness of the information contained in this report, or that the use of any information, apparatus, method, or process disclosed in this report may not infringe privately owned rights; or

B. Assumes any liabilities with respect to the use of, or for damages resulting from the use of any information, apparatus, method or process disclosed in this report.

As used above, "person acting on behalf of NASA" includes any employee or contractor of NASA, or employee of such contractor, to the extent that such employee or contractor of NASA, or employee of such contractor prepares, disseminates, or provides access to, any information pursuant to his employment or contract with NASA, or his employment with such contractor.

Requests for copies of this report should be referred to

National Aeronautics and Space Administration
Scientific and Technical Information Facility
P.O. Box 33
College Park, Maryland 20740

NASA CR-54569
FEBRUARY 1968
Allison EDR 5658

Single-Stage Experimental Evaluation of Boundary Layer Bleed Techniques for High Lift Stator Blades

I - Compressor Design

by

M. L. Miller and D. C. Chapman

Prepared for

NATIONAL AERONAUTICS AND SPACE ADMINISTRATION

Contract NAS3-7900

Technical Management
NASA-Lewis Research Center
Cleveland, Ohio

Lewis Project Manager: William L. Beede
Lewis Research Advisor: L. Joseph Herrig

Allison Division • General Motors

Indianapolis, Indiana

PRECEDING PAGE BLANK NOT FILMED.

TABLE OF CONTENTS

Section	Title	Page
	Summary	1
	Introduction	2
	Symbols	3
	Overall Aerodynamic Design	7
	Selection of Basic Design Parameters	7
	Loss Determination Procedures	8
	Inlet Guide Vane Loss Correlation	8
	Rotor Loss	9
	Stator Loss Correlation	9
	Velocity Diagram Calculations	10
	Inlet Guide Vane Design	11
	Rotor Blade Design	12
	Stator Blade Design	12
	Deviation Angle or Flow Turning	13
	Design Incidence Angle	14
	Flow Range Analysis	17
	Off-design Inlet Guide Vane Design	19
	Boundary Layer Control Design	20
	Pressure Distribution	20
	Boundary Layer Growth and Separation	20
	Slot Design	24
	Mechanical Design and Stress Analysis	28
	Rig Design	28
	Stress and Vibration Analysis	30
	Rotor System	30
	Stator Blades	31
	Bearing Supports	31
	References	32
	Appendix, Compressor Flow Analysis	33

LIST OF TABLES

Table	Title	Page
I	Inlet guide vane design parameters	36
II	Rotor blade properties	37
III	Incidence angle-camber variation for 65-series airfoil with 53.9° flow turning, 1.7 solidity, and a=1 meanline	38
IV	Stator aerodynamic and airfoil geometric properties—65-series airfoil on circular arc meanline	39
V	Comparison of stator exit flow angles calculated using Method 2 and design flow angles	40
VI	Rotor blade dovetail serration stresses	41
VII	Stator vane slot deflection and natural frequencies without slot ties	42

LIST OF ILLUSTRATIONS

Figure	Title	Page
1	Midstage stator hub and rotor tip loadings for $(R_H/R_T)_2 = 0.7$	43
2	Preliminary design study—stator hub Mach number and turning angle	44
3	Rotor design total pressure loss coefficient distribution	45
4	Wake momentum thickness with and without boundary layer control	46
5	Comparison of annular and two-dimensional cascade losses	47
6	Rotor design radial work gradient	48
7	Velocity diagrams for flow generation rotor	49
8	Velocity diagrams for 0.75 hub D_f stator	50
9	Velocity diagrams for 0.65 hub D_f stator	51
10	Inlet guide vane total pressure loss coefficient distribution	52
11	Stator design total pressure loss coefficient distribution	53
12	Test rig flow path	54
13	Velocity triangle compressible-incompressible relationship for compressibility effect	55
14	Air turning angle as a function of equivalent circular arc camber with $\beta_2 = 45°$ and $\sigma = 1.0$	56
15	Air turning angle as a function of equivalent circular arc camber with $\beta_2 = 60°$ and $\sigma = 1.0$	57
16	Air turning angle as a function of equivalent circular arc camber with $\beta_2 = 60°$ and $\sigma = 1.5$	58
17	Estimated 0.75 hub D_f stator performance with and without boundary layer control	59
18	Drag coefficient as a function of equivalent circular arc camber for $\beta_2 = 60°$ and $\sigma = 1.5$	60
19	Stalling incidence and onset of leading edge velocity peak for $\beta_2 = 45°$ and $\sigma = 1.0$	61
20	Stalling incidence and onset of leading edge velocity peak for $\beta_2 = 45°$ and $\sigma = 1.5$	62
21	Stalling incidence and onset of leading edge velocity peak for $\beta_1 = 60°$ and $\sigma = 1.5$	63
22	Crossplot for stator incidence and camber selection	64
23	Estimated flow generation rotor performance with design inlet guide vanes	65
24	Operating range of 0.65 hub D_f stator at design inlet Mach numbers	66
25	0.75 hub D_f stator operating range at design inlet Mach numbers	67

Figure	Title	Page
26	Margin between stator design inlet angle and stator inlet angle at rotor stall—design inlet guide vanes . .	68
27	Margin between stator design inlet angle and stator inlet angle at rotor choke point—design inlet guide vanes	69
28	Estimated flow generation rotor performance with off-design inlet guide vanes	70
29	Margin between stator design inlet angle and stator inlet angle at rotor choke point—off-design inlet guide vanes	71
30	Margin between stator design inlet angle and stator inlet angle at rotor stall—off-design inlet guide vanes. . .	72
31	Typical cascade airfoil pressure coefficient variation . .	73
32	0.75 hub D_f stator pressure distribution.	74
33	0.65 hub D_f stator pressure distribution.	75
34	Incompressible boundary layer form factor for 0.75 D_f stator.	76
35	Incompressible boundary layer form factor for 0.65 D_f stator.	77
36	Boundary layer schematic at bleed slot location.	78
37	Incompressible form factor distribution downstream of bleed slot for 0.75 D_f stator	79
38	Incompressible form factor distribution downstream of bleed slot for 0.65 D_f stator	82
39	Schematic of slot geometry and bleed flow summary . . .	85
40	Portions of blade span assigned to hub, mean, and tip section for slot calculation	86
41	Single-slot bleed flow for various slot configurations for 0.75 D_f stator	87
42	Single-slot bleed flow for various slot configurations for 0.65 D_f stator	88
43	Schematic of minimum area in blade suction path	89
44	Unslotted stator suction surface static pressure distribution at 80% speed and 50% streamline.	90
45	Triple slot bleed flow for various slot heights for 0.75 D_f stator	92
46	Layout of component test rig.	93
47	Rotor blade stresses	94
48	Rotor blade frequencies	95
49	Rotor wheel disk stresses at design speed.	96
50	Coned drive shaft stresses at design speed	97
51	0.65 hub D_f vane bending stress (unslotted and pinned) . .	98
52	0.65 hub D_f vane frequency (unslotted and pinned).	99
53	0.75 hub D_f vane bending stress (unslotted and pinned) . .	100
54	0.75 hub D_f vane frequency (unslotted and pinned).	101
55	Test rig critical speeds	102

SINGLE-STAGE EXPERIMENTAL EVALUATION OF BOUNDARY LAYER BLEED TECHNIQUES FOR HIGH LIFT STATOR BLADES

I—COMPRESSOR DESIGN

by

M. L. Miller and D. C. Chapman

Allison Division, GM

SUMMARY

Three stator blade sets were designed for use in investigating the effectiveness of boundary layer control by bleeding as a means of reducing losses and increasing stall-free range for highly loaded axial flow compressor blading. The concepts studied may be applicable to either rotors or stators. This study, however, was limited to stators to minimize mechanical problems. An inlet guide vane and state-of-the-art flow generation rotor were designed to produce the stator inlet flow. The stator hub inlet Mach number was 0.75, the stator hub inlet flow angle was 54 degrees, and the stator hub-to-tip ratio was 0.70. These values were considered to be representative of middle and latter stages of highly loaded axial flow compressors

The stator blade section selected was a 65-series thickness distribution with a circular arc meanline shape. Available low speed cascade data was extrapolated to determine blade camber and setting angles. The first stator was designed for a hub blade element diffusion factor of 0.65 (38.8 degrees of turning) and the second and third stators were designed for hub blade element diffusion factors of 0.75 (.4 degrees of turning). A single slot was designed for the first and second stators and a triple slot was designed for the third stator.

Boundary layer analyses were made to predict boundary layer growth and points of separation using pressure distributions that were obtained from extrapolation of cascade data. Slots were designed to remove a portion of the boundary layer air by bleeding. Boundary layer air is bled through the spanwise slot or slots in the suction surface of the blade into the vane core and is extracted through the hollow tip trunnion to an external vacuum header. The slots are formed by a simple planar cut of constant width with the minimum mechanically feasible inclination of 45 degrees to the local surface tangent.

INTRODUCTION

Advanced airbreathing propulsion systems require lightweight compact compressors capable of high levels of performance. These compressors should have a broad range of operation and a large stall margin. High reliability and relative insensitivity to inlet flow distortion are generally required of all compressors. In meeting the more demanding compressor design requirements, compromises must be made that are strongly dependent on the particular application. New applications are steadily increasing the range of requirements which the compressor must meet.

Compressor technology has been advanced continuously by extending, among other parameters, the usable rotational speeds, increasing stage loadings or diffusion factors, and reducing stage length through the use of high blade aspect ratios. Whereas further advancements can be made through optimizations and improved combinations of the aforementioned parameters, severe aerodynamic limitations such as increasing losses and decreased stall margin are being encountered. Significant advancements in compressor technology require the application of advanced concepts in terms of improved blading for high flow Mach numbers and application of high lift devices to extend the stall-free flow range for compressor rotors and stators. Advanced concepts in these areas may result in sizable reductions in the number of compressor stages and improved compressors, depending on the requirements of the application.

Limiting values of blade loading and angle of attack are associated with steep blade surface pressure (or velocity) gradients and separation of the suction surface boundary layer. Separation of the suction surface boundary layer can be delayed by removing the low energy portion of it by means of a bleed slot or slots. In view of these considerations, an experimental single-stage compressor rig was designed and constructed to test highly loaded stators using boundary layer bleed concepts to reduce losses and improve stall-free low margin.

The objectives of this program are to establish experimentally the feasibility and extent of increasing blade loading and stall-free flow margin by boundary layer bleed. A secondary objective is to obtain blade element data for design use. Three slotted stator designs are to be made which are representative of those for middle and latter stages of highly loaded axial flow compressors. Stator inlet flow is to be generated by a state-of-the-art flow generation rotor. This report presents the details of the aerodynamic and mechanical design of the facility and the three slotted stator configurations.

A similar program using blowing boundary layer control on highly loaded stators will also be tested on this compressor rig. The design of those stators is reported in Reference 1.

SYMBOLS

a	Meanline shape definition and sound velocity, ft/sec
A	Area, ft^2
b	Solidity exponent in deviation equation
c	Airfoil chord, in.
C	Correlation factor = 0.42, Equation (6), degrees
C_p	Specific heat of air at constant pressure, Btu/lb_m-°R
C_D	Drag coefficient
C_{L_O}	Camber level, expressed in terms of isolated airfoil lift coefficient
C_{W_1}	Wake momentum difference coefficient
D_{eq}	Equivalent diffusion ratio
D_f	Diffusion factor
E_C	Compressibility correction, degrees
E_{SF}	Secondary flow correction, degrees
g	Gravitational constant, 32.2 $ft\text{-}lb_m/lb_f\text{-}sec^2$
h	Height of bleed slot, in.
ΔH	Enthalpy change across rotor, Btu/lb_m
H	Boundary layer form factor
i	Incidence angle based on mean camber line, degrees
J	Mechanical heat equivalent, 778 $ft\text{-}lb_f/Btu$
K	Empirical constant, Equation (8)
K_A	Bleed slot aspect ratio coefficient
K_T	Bleed slot flow coefficient
$(K_\delta)_{sh}$	Deviation correction for blade other than 65-series
$(K_\delta)_t$	Deviation correction for blade thickness other than 10%

L_{ax}	Axial projected chord, in.
$m_{\sigma = 1}$	Slope of deviation angle variation with inlet flow angle for unity solidity
$\dot{m}$	Mass flow rate, lb_m/sec
M	Mach number
n	Denominator in exponent of velocity profile, Equation (18), and number of blades
N	Rotational speed, rpm
O	Cascade throat dimension, in.
p	Static pressure, psia
P_t	Total pressure, psia
q	Dynamic pressure, psia
q_n	Normal induced velocity component, ft/sec
R	Radius, in.
R_c	Pressure ratio
Re	Reynolds number
$\mathcal{R}$	Gas constant, 53.3 lb_f-ft/lb_m-°R
S	Airfoil surface pressure coefficient, $(P_{t_2}-p)/q_2$, dimensionless, or entropy, Btu/lb_m-°R
s	Blade spacing, in.
t/c	Thickness-to-chord ratio
t	Static temperature, °R
T_t	Total temperature, °R
u	Suction surface velocity, ft/sec
U	Wheel tangential velocity, ft/sec
V	Air velocity, ft/sec

W_a	Compressor airflow, lb_m/sec
X	Distance along chord, in.
y	Coordinate normal to suction surface

Greek

α	Angle of attack or streamline slope, degrees
β	Air angle, degrees
$\Delta\beta$	Air turning angle, degrees
γ	Ratio of specific heats
γ°	Blade chord angle, degrees
δ	Boundary layer thickness, ft, or ratio of total pressure to standard sea level pressure of 2116.2 psfa
δ^*	Displacement thickness, ft
δ°	Deviation angle, degrees
$(\delta_o^\circ)_{10}$	Deviation angle for 65-series airfoil with zero camber and 10% t/c, degrees
μ	Viscosity, $lb_m/ft\text{-}sec$
η	Adiabatic efficiency
θ	Momentum thickness, ft, or ratio of total temperature to standard sea level temperature of 518.6°R
κ	Blade metal angle, degrees
ρ	Density, lb_m/ft^3
σ	Blade row soiidity, c/s
ϕ	Camber angle, degrees
ψ	Angle of inclination between center line of bleed slot and tangent to suction surface, degrees
$\bar{\omega}$	Loss coefficient

Subscripts

A	**Annulus**
b	Boundary layer bleed
BL	Boundary layer
BLC	**Boundary layer control**
C	Corrected or compressibility
ch	Choking condition
des	Design
E	Stator equivalent inlet flow angle
e	Edge of boundary layer
H	Hub section
i	Incompressible or reference station
m	Mean streamline
o	At slot location
O	Throat
r	Radial direction
R	Rotor
s	Stator
SF	Secondary flow
sl	Streamlines
T	Tip section
t	Evaluated at an isentropic stagnation point in the free stream
v	Constant axial velocity condition
WBLC	Without boundary layer control
z	Axial direction
θ	Tangential direction or based on momentum thickness

0	Guide vane inlet
1	Rotor inlet
2	Rotor exit or stator inlet
3	Stator exit

Superscripts

'	Relative value
*	Sonic conditions or minimum loss

OVERALL AERODYNAMIC DESIGN

The requirements of the contract were to produce stator flow conditions and loading that would typically occur in the middle or latter stages of a highly loaded compressor. Initially, a multistage compressor design analysis was made to ensure that the stator design chosen was compatible with requirements of a multistage machine. The test stage was then designed with the stator blade row as the research blade. The inlet guide vane and flow generation rotor were designed within current state of the art to produce the desired flow into the stator. Stator loading can be increased by decreasing the solidity, diffusion of axial velocity, or by increased turning. The first two techniques, however, are not considered representative of good design practice. Therefore, for this study, high stator loading was achieved by means of high turning. To avoid excessive rotor loading or turning past the axial direction by the stator, inlet guide vanes were used.

The initial step in the design process was the selection of the basic design variables. Next, loss correlations were established for the inlet guide vane, rotor, and stator vane rows. Velocity diagrams were then calculated by an iteration between velocity diagram values and blade losses. Finally, the blade geometry in terms of blade camber and setting angle was determined.

SELECTION OF BASIC DESIGN PARAMETERS

Preliminary studies were conducted to determine design specifications which would be representative of the middle or latter stages of advanced compressors and to determine what form of velocity diagram would best satisfy the design requirements. Multistage compressors with four tip speeds were investigated in this study, each having an overall pressure ratio of 9:1. Tip speeds were 950, 1050, 1150, and 1250 ft/sec and the compressors considered for each tip speed were as follows:

- 5 stage, 1.55 average stage pressure ratio
- 6 stage, 1.442 average stage pressure ratio
- 8 stage, 1.316 average stage pressure ratio (except at 950 ft/sec)

Compressor tip diameter was 30 inches. Velocity diagrams were computed using free vortex design and axial entry into each rotor. From these analyses, the pertinent values of a middle stage were examined. Stages selected for comparison were those with a stator inlet hub-to-tip radius ratio of approximately 0.7.

Results of the study are shown in Figure 1, where both stator hub and rotor tip diffusion factors are plotted against the pressure ratio of the stage in question. Solidity values assumed were 1.0 at the rotor tip and 1.9 at the stator hub. The heavy dashed line in Figure 1 is the locus of rotor tip diffusion factors required to produce a stator hub diffusion factor of 0.75. The values range from 0.7 at a tip speed of 950 ft/sec down to 0.59 at a tip speed of 1250 ft/sec. Corresponding stator hub Mach numbers and turning angles are shown in Figure 2.

On the basis of this analysis, the stator hub Mach number for this study was chosen to be 0.75. Two stator hub diffusion factors were selected—0.65 and 0.75. Tip diameter of the test compressor was chosen to be 30 inches and is constant across the inlet guide vane, rotor, and stator vane. NACA 63-006 airfoil sections were used for the inlet guide vane and double circular arc airfoil sections for the rotor. The 63-series sections were selected because of the availability of blade element design data and the double circular arc sections for the blades because of their better performance in the transonic range.

Design of the high lift stators necessitated the use of available cascade data. Therefore, the 65-series airfoil section was selected. The 65-series section is compatible with the upper level of 0.75 inlet Mach number. To define incidence and deviation angles quantitatively, the circular arc mean-line was selected for designing the stator airfoil sections.

LOSS DETERMINATION PROCEDURES

Inlet Guide Vane Loss Correlation

The inlet guide vane is based on the basic NACA 63-006 airfoil because of the availability of cascade data. Inlet guide vane losses were calculated from the wake momentum difference coefficients (C_{W_1}) of Reference 2. Wake momentum thickness coefficient may be calculated from wake momentum difference coefficient as follows:

$$(\theta/c)_1 = \frac{C_{W_1}}{2} \left(\frac{\cos \beta_1}{\cos \beta_0}\right)^2 \left[1 - \left(\frac{\theta}{c}\right)_1 \frac{\sigma H_1}{\cos \beta_1}\right]^2 \qquad (1)$$

The total pressure loss coefficient, $\bar{\omega}$, may then be calculated from the wake momentum thickness coefficient by the relation:

$$\omega = 2\left(\frac{\theta}{c}\right)_1 \frac{\sigma}{\cos\beta_1}\left(\frac{\cos\beta_0}{\cos\beta_1}\right)^2\left(\frac{2\,H_1}{3\,H_1-1}\right)\left[1-\left(\frac{\theta}{c}\right)_1\frac{\sigma\,H_1}{\cos\beta_1}\right]^{-3} \qquad (2)$$

where H_1 is the wake form factor for which a value of 1.08 was used.

Rotor Loss

The selected total loss coefficient distribution for the rotor is shown in Figure 3. This distribution of loss is based on an existing compressor having very simi design values of blade loading and tip speed. Total pressure loss coefficients shown in Figure 3 are measured values of unpublished test results.

Stator Loss Correlation

Stator losses at design conditions were derived from Lieblein's work on equivalent diffusion ratio in Reference 3. The equivalent diffusion ratio at minimum loss is calculated as follows:

$$D^*_{eq} = \frac{\cos\beta_3}{\cos\beta_2}\left[1.12 + 0.61\,\frac{\cos^2\beta_2}{\sigma}\,(\tan\beta_2 - \tan\beta_3)\right] \qquad (3)$$

Assuming the rapid rise in momentum thickness coefficients for values of D^*_{eq} greater than about 1.9 is caused principally by separation, it was further assumed that with a practical method of boundary layer control momentum thickness coefficients at a given D^*_{eq} could be held to the lowest measured values. In Figure 4, the upper curve represents the mean of the data by which Lieblein correlated momentum thickness with D^*_{eq}. The lower curve is a line drawn through the lower edge of the data scatter; this line is assumed to represent momentum thickness as a function of D^*_{eq} with effective boundary layer control for a two-dimensional cascade. The corresponding total pressure loss coefficient may then be calculated from Equation (2) (upon replacing Subscripts 0 and 1 by 2 and 3) in which H_3 is the stator wake form factor for which a value of 1.08 was used. This loss coefficient is considered representative of two-dimensional cascade losses with boundary layer control. Losses for two-dimensional cascades and annular cascades from Reference 4 for various locations are compared in Figure 5 as functions of diffusion factor. It is possible to obtain the ratio of annular to two-dimensional losses for a given radial position by entering the curves in Figure 5 at the diffusion factor of the cascade with boundary layer control. The two-dimensional loss coefficient obtained from Equation (2) is multiplied by the foregoing ratio to obtain the final profile loss coefficient representative of the annular cascade with boundary layer control.

VELOCITY DIAGRAM CALCULATIONS

Velocity diagrams were calculated by an axisymmetric compressor analysis which accounts for curvature and entropy gradient terms in the radial equilibrium solution. The calculation procedure is described in the Appendix.

The design velocity diagram calculations were accomplished assuming no end-wall bleed. The decision to ignore end-wall bleed in the design was based on the possibility that wall bleed may not be required during test. The effect of wall bleed on diffusion through the stators was examined and was found to give only a 2 to 3% increase in stator diffusion factors for wall bleed rates to 3% of compressor inlet flow on each wall. Boundary layer blockage factors used were 0.995 at inlet to the inlet guide vanes, 0.985 at rotor inlet, 0.975 at stator inlet, and 0.965 at stator exit. All blockage was assumed to be at the hub. The rotor is designed for nearly constant total pressure rise radially. The radial variation of rotor energy addition is shown in Figure 6.

Design velocity diagrams for guide vane, rotor, and stators are shown in Figures 7, 8, and 9. The rotor tip speed is 1095 ft/sec and the tip diffusion factor is 0.414, based on the tip solidity value of 1.35. Diffusion factors at the other rotor stations are also near 0.4 and are, therefore, well within state of the art to ensure good rotor operation. The resultant inlet guide vane and stator radial loss distributions are shown in Figures 10a and 11, respectively.

The flow path is shown in Figure 12. Rotor inlet hub-tip radius ratio is 0.68 compared to the 0.7 value at stator inlet. With the blade aspect ratio of 1.66, the hub ramp angle is low and curvature effects are small.

Final design values for the flow generation rotor are:

$W_a\sqrt{\theta}/\delta$ = 88.2 lb/sec

$R_{c(rotor)}$ = 1.37

η_R = 88.8%

$N/\sqrt{\theta}$ = 8367 rpm

The stage design values for the 0.75 D_f stator are estimated at R_c = 1.35 and η = 85.5%. For the 0.65 D_f stator, the design values are R_c = 1.355 and η = 86.4%.

INLET GUIDE VANE DESIGN

The NACA 63-006 airfoil was selected because of the availability of cascade data. The guide vane design is based on free vortex tangential velocity distribution in the direction of rotor rotation and corrections are included for compressibility and secondary flow effects. Design point for the inlet guide vane is $W_a\sqrt{\theta}/\delta$ = 88.2 lb/sec at an inlet Mach number of 0.389 and mean radius design turning of 23.86 degrees.

Compressibility effects were established for each blade element using the method of Reference 5. The correction for compressibility, which is applied to the design flow turning angle (β_1), is given by:

$$E_C = \beta_{1_C} - \beta_1 \tag{4}$$

where:

$$\tan \beta_{1C} = \left(\frac{V_{z_1}}{V_{z_0}}\right) \frac{\tan \beta_{1v_i}}{\tan \beta_{1v}} \tan \beta_1 \tag{5}$$

Equation (5) describes the relation between an incompressible and compressible flow condition across the blade element and is shown schematically in Figure 13. If no other flow effects were to be considered, the guide vane design camber would be based on the turning given by $\beta_{1_C} - \beta_0$.

Secondary flow effects were established for each blade element using the method of Reference 6. The correction for secondary flow which is applied to the design flow turning angle is given by:

$$E_{SF} \equiv \beta_{1_{SF}} - \beta_1 = C \tan^{-1} (q_n/V_1) \tag{6}$$

A correlation factor "C" of 0.42 was used which was the empirically developed value of Reference 6. Boundary layer thicknesses at the guide vane inlet are required to evaluate the normal induced velocity component. These were determined using a turbulent boundary layer growth calculation based on the method of Culick and Hill in Reference 7. An 8-foot long section was assumed between the bellmouth and the compressor inlet tip section and a conventional bullet nose upstream of the hub section.

Once the compressibility and secondary flow corrections are determined, the guide vane camber is determined based on the corrected design flow turning angle for the blade element, given by:

$$(\Delta\beta)_C = (\beta_1 - \beta_0) + E_C + E_{SF} \tag{7}$$

Blade camber and angle of attack can then be obtained from Reference 2 for the corrected design flow turning and solidities.

A summary of aerodynamic and airfoil geometry data is given in Table Ia for the inlet guide vane. Thirty-four vanes are required.

ROTOR BLADE DESIGN

Double circular arc blade sections were chosen for the rotor blades. The design values of inlet Mach number range up to 0.95 and double circular arc profiles are preferred to 65-series profiles at that Mach number level. The sections were designed on a plane normal to the stacking axis, which for this blade is a radial line which passes through the center of gravity of each blade section.

The blade chord was chosen to produce a smooth flow path as well as a conservative rotor aspect ratio. The blade chord is 2.875 inches and is constant from hub to tip. Rotor aspect ratio based on inlet blade height is 1.66.

Rotor solidity was chosen to be the maximum value attainable commensurate with minimum blade thickness which fulfilled mechanical requirements and provided sufficient flow margin at all radial stations. Solidity and thickness-to-chord values respectively range from 1.37 and 0.032 at the tip to 1.97 and 0.078 at the hub with calculated choke flow margins of 6.2% at the tip and 12.0% at the hub section. Forty-five blades are required.

Incidence angles for all radial stations of the rotor blade were chosen to be zero degrees with the mean camber line. The choice of this incidence level and the constant value hub to tip was based on Allison experience on similar designs.

Deviation angle was estimated by a modified Carter's rule:

$$\delta^\circ = \frac{0.25\phi}{\sqrt{\sigma}} + K\,(t/c) \tag{8}$$

Deviation ranged from 4.6 degrees at the tip to 7.8 degrees at the hub section. Resultant camber and setting angles are listed in Table II.

STATOR BLADE DESIGN

The stator loading levels imposed by the design velocity triangles are expected to result in separated flow at some, if not all, radial stations of

conventional stators. The objective of this program is to design stators with boundary layer control devices of the bleed type which will achieve the desired levels of turning without the high losses associated with separated flow. The pressure distribution around the airfoil surfaces must be established to design the boundary layer control slots. In addition, the design incidence angle and deviation angle must be established to define the airfoil.

A review of available procedures led to the conclusion that the most expedient means of determining the aforementioned required data was to extrapolate existing low speed cascade data. The most extensive cascade data available was for the NACA 65-series airfoils. The Mach number level of the stators was compatible with this airfoil; therefore, this airfoil was chosen for the stators. The cascade data were obtained for airfoils with a = 1 meanline. Circular arc meanlines have been chosen for this application because of the easier identification of incidence and deviation angles in the test program. Inaccuracies attributable to the differences in the two meanlines were considered to be less significant than those introduced by the extrapolations of the cascade data. The cascade data, on which these stator designs were based, were taken from Reference 8.

Deviation Angle or Flow Turning

The analysis of deviation angle or flow turning angle with boundary layer control began with cross plots of flow turning angle versus lift coefficient from the cascade data of Reference 8. These plots are shown in Figures 14, 15, and 16. Also shown on these plots are the ideal flow turning line (zero deviation angle), the flow turning resulting from the deviation angle predicted by the NACA deviation angle rule, and the first approximation for flow turning with boundary layer control. Deviation angle as computed by the NACA rule is given by:

$$\delta^\circ = (K_\delta)_{sh} (K_\delta)_t (\delta^\circ_o)_{10} + \frac{m_{\sigma=1}\phi}{\sigma b} + \frac{d\delta^\circ}{di} (i - i^*) \qquad (9)$$

The third term on the right hand side of Equation (9) was neglected, since its effect is negligible for solidities much above 1.2.

Flow turning angle, $\Delta\beta$, is then defined by:

$$\Delta\beta = \phi - \delta^\circ + i \qquad (10)$$

Examination of Figures 14, 15, and 16 indicates that the flow turning predicted through application of the NACA deviation angle rule at zero incidence fits the cascade data very well in the normal ranges of camber and solidity but that the actual deviation is greater when the curves are extrapolated to the higher camber angles.

The first approximation for flow turning angle with boundary layer control was based on the assumption that the deviation angle that would be obtained without boundary layer control would be reduced by 50% by the application of boundary layer control. That is:

$$\delta^\circ_{BLC} = (1/2)\ \delta^\circ_{WBLC} \tag{11}$$

where:

δ°_{BLC} = deviation angle with BLC

δ°_{WBLC} = deviation angle without BLC at zero incidence (cascade data value)

Comparing the first approximation line with the NACA deviation angle rule line in Figures 14, 15, and 16 indicates that at a turning angle of about 50 degrees (representative of the turning of the 0.75 D_f stator), the differences between the two lines are comparatively small. At a turning of about 30 degrees (representative of the turning of 0.65 D_f stator), the flow turning degradation due to gross flow separation is not large as indicated by the agreement between the NACA deviation angle rule and the cascade data. The NACA deviation angle rule, therefore, was selected as the means of estimating flow turning with boundary layer control.

A typical example of the estimated improvement in stator flow turning due to maintaining an attached boundary layer by BLC is shown in Figure 17. The flow turning values for no BLC were taken from the extrapolated data of Figure 16. The curves indicate that, for the given conditions, it is anticipated that the flow turning could be improved from 40 to slightly over 60 degrees by the application of BLC. Also shown in Figure 17 is the estimated reduction in stator loss due to BLC. The minimum loss values were obtained from the θ/c versus D^*_{eq} curves of Figure 4 and corrected for three-dimensional flow effects using the data of Figure 5 as outlined in the stator loss analysis procedure. The shape of the loss curve for no BLC (Figure 17) was determined from the extrapolated cascade drag coefficient data of Reference 8, shown in Figure 18. This curve, along with the assumption that minimum loss will occur at zero incidence and the flow turning curve, was used in the loss bucket estimation for the stator airfoil section with BLC.

Design Incidence Angle

Initial stator vane designs using the selected deviation angle rule and the assumption of zero design incidence angle indicated that leading edge region velocity peaks were possible at zero incidence angle for blades having larger camber. For this discussion, leading edge region is defined as 0 to 5% chord. Estimated pressure distributions obtained as described in this report in the Pressure Distribution section indicated that boundary layer

separation could occur well before 50% chord. This type of velocity distribution is not expected to respond well to a bleed boundary layer control device which is primarily intended to delay separation and reduce losses near design incidence. To counteract separation on the forward part of the blade, the bleed slot location may be required to be upstream of or at the throat, which is aerodynamically not desirable.

To obtain a satisfactory estimate for design incidence angle, the cascade data of Reference 8 was analyzed to obtain the incidence angle for the onset of leading edge velocity peak and stalling incidence, defined as twice the minimum drag, as shown in Figures 19, 20, and 21. It will be appreciated that the cascade data is subject to a certain amount of interpretation, particularly in the choice of angle for onset of leading edge velocity peak. Insofar as possible, this was chosen to be the angle at which the leading edge region (0 to 5% chord) pressure coefficient had just become the highest value recorded on the blade surface. For highly cambered blades, the rise of leading edge pressure coefficient appears to occur very rapidly for small increases in incidence angle thereafter. Consequently, the angles given in Figures 19, 20, and 21 do not represent the maximum values of incidence for prospectively effective boundary layer control use but incidences which are close to the maximum.

Interpolating between the data of Figures 19, 20, and 21 for the 0.75 diffusion factor vane hub, an estimated incidence versus camber for the onset of leading edge velocity peak can be obtained. The results are shown in Figure 22 by the solid curve for the stator hub inlet flow angle of 53.9 degrees and solidity of 1.7. To estimate the required incidence and camber for the 53.9-degree flow turning at the stator hub, the NACA deviation angle rule is used for calculating deviation with boundary layer control. Combining Equations (9) and (10) and neglecting the $d\,\delta^\circ/di$ term yields:

$$\phi = \left[\beta_2 - \beta_3 - i + (\delta_o^\circ)_{10}\right] \Big/ \left[1 - \frac{m_{\sigma=1}}{\sigma^b}\right] \tag{12}$$

Since comparisons between the first approximation and NACA deviation angle rule, as shown in Figure 14, 15, and 16, were not made at incidences other than zero degrees, two methods of application were tried. This approach was selected in place of making comparisons at other incidence values since the accuracy of the extrapolation to cambers on the order of 80 degrees is marginal.

Method 1 was defined consistent with a zero-degree incidence condition, wherein $m_{\sigma=1}$, b, and $(\delta_o^\circ)_{10}$ were varied by adjusting the inlet flow value by the incidence change. For example $\beta_2 = 53.9°$ at $i = 0°$ and $\beta_{2E} = 57.9°$ at $i = -4°$. Results of this calculation are shown in Table IIIa and plotted as the broken curve in Figure 22. The intersection of the solid and broken

curves gives the required blade camber which for the 0.75 D_f stator hub gives an incidence of -3 degrees with a value of C_{L_O} = 2.86 and an equivalent circular arc camber of 72 degrees.

Method 2 is the defined approach of the NACA deviation angle rule in Reference 4. That is, the values of $m_{\sigma=1}$, b, and $(\delta_o^\circ)_{10}$ remain fixed at β_2 = 53.9°. Results of this calculation are shown in Table IIIb and plotted as the dashed curve in Figure 22. The intersection of the solid and dashed curves gives the required blade camber which for the 0.75 D_f stator hub gives an incidence of -1.8 degrees with a value of C_{L_O} of 2.75 and an equivalent circular arc camber of 69.2 degrees.

Considering that much interpretation, interpolation, and extrapolation was required at these high cambers to obtain the solid curve in Figure 22, the difference of 1.2 degrees in incidence and 2.8 degrees in camber is considered well within the accuracy of the calculations. The value from Method 1 was selected, however, since it resulted in greater deviations or higher camber which places the design values on the conservative side.

The initial blade design for this stator hub indicated choking incidence at -6 degrees at a C_{L_O} = 2.74. Calculations show that the choke incidence angle of highly cambered blades discussed herein will not change significantly with a moderate change in camber. Therefore, it is assumed that this stator will choke at an incidence angle of approximately -6 degrees. Based on experience with previous stage designs of this type, it is considered that the incidence angle operating range between choke and onset of leading edge velocity peak should be approximately 6 degrees. Figures 20 and 21 indicate an available range of 1 to 2.3 degrees between stall and onset of leading edge velocity peak at a lift coefficient of 2.88 and solidity of 1.5. The increased solidity of the stator hub section would be expected to increase that range somewhat. A value of 3 degrees seems reasonable for the incidence angle range between stator stall and onset of leading edge velocity peak for the hub section of the 0.75 D_f stator. Therefore, the design incidence for the 0.75 D_f stator of -3 degrees was confirmed as a reasonable choice.

Identical interpolation procedures using Method 1 for deviation angle determination were followed for the 0.65 D_f hub section to estimate design incidence angle. The results obtained indicated that design incidence required would be about 7 to 10 degrees. These results were considered unrealistic and due in part to the fact that velocity decelerations across the vane row in the stationary cascade were not typical for the high inlet flow angle. That is, the stator row blade sections are not required to turn the flow back to the axial direction for this diffusion factor. Therefore, it was decided to select the 3-degree incidence angle change for operating range away from the choke incidence condition. Since initial choke incidence

angles were determined to be zero degrees for the 0.65 D_f hub stator section, the design incidence angle was selected as +3 degrees.

Allison design experience indicates and supports a constant design incidence angle selection spanwise on the stator vanes as on the rotor blades. The resultant stator airfoil design sections are summarized in Table IV. A constant thickness of 10% was selected for all sections since it gave minimum thickness with sufficient core area for boundary layer control mass transfer flow rate requirements at a 3-inch chord with a hub solidity of 1.705. Thirty-eight stator vanes are required.

As stated previously, deviation angle determination by Method 1 resulted in higher camber of the stator vane relative to Method 2. For comparison purposes, the stator outlet flow angles determined by Method 2 using the inlet flow conditions and airfoil section properties from Table IV are given in Table V. Calculated results show a higher turning of 3.6 to 4.3 degrees for the 0.75 hub D_f stator and 1.0 to 1.7 degrees for the 0.65 hub D_f stator by Method 2.

FLOW RANGE ANALYSIS

Fulfillment of the test requirements of this task necessitates testing the stators over their stall-free operating range (i.e., from stator choke to stator stall). Therefore, it was necessary to determine if the flow generation rotor was capable of providing stable flow to the stators over this full range.

Estimated rotor performance with the inlet guide vanes is shown in Figure 23. Data for the estimated efficiencies were obtained from unpublished test data. The limits of each speed line in Figure 23 are taken as the stall and choke points of the rotor at that speed.

The inlet angle at which the stator chokes was calculated using the following formula:

$$\beta_{2_{ch}} = \cos^{-1} 0.95\ (A/A^*)\ (O/s) \tag{13}$$

The product of A/A^* and O/s represents the ratio of the ideal approach width-to-vane spacing for choking conditions. An empirical factor of 0.95 accounts for real flow effects. Choke incidence angle was then computed from:

$$i_{ch} = \beta_{2_{ch}} - \kappa_2 \tag{14}$$

Choke incidence values were computed at hub, mean, and tip for both stators. The results are summarized in Table IV.

An extrapolation of cascade data from Reference 8 was also used to determine the stall margin of both stators. Plots of air turning angle as a function of incidence angle were made for cascades representative of the stator sections. This data determined the shape of a curve drawn through the design incidence and design air turning angle coordinates for the stator section in question. Curves of this nature are demonstrated in Figures 24 and 25. The hub section of each stator was assumed to control the stall limit. In Figure 24, the maximum air turning angle for the 0.65 D_f stator is seen to occur at an incidence angle of 8 degrees and the angle range between the design point and stall is shown to be approximately 5 degrees. The choke ends of the curves deviate from the cascade data to reflect the choking characteristics of the stator as calculated from Equations (13) and (14). Figure 25 illustrates the results of this technique for the 0.75 D_f stator. There is no clearly defined maximum turning angle from this data extrapolation. Therefore, stall is assumed to occur when the loss is equal to twice the minimum loss. The stall incidence values are summarized in Table IV.

To relate the rotor limits to stall and choke limits of the stator, a simplified analysis based on mean radius characteristics was employed. It was assumed for this analysis that the deviation angles for the inlet guide vanes and rotor were constant over the range of speeds and flows.

Rotor inlet axial velocity was assumed constant radially at values calculated from the rotor inlet area, inlet guide vane exit conditions, and the weight flows from Figure 23. The combination of axial velocity, rotor blade speed, and guide vane exit conditions specified the rotor relative inlet conditions. These were calculated for tip, mean, and hub stations. Energy input in the rotor was assumed constant radially at the value calculated for the mean-radius station. Rotor exit conditions were calculated using the rotor exit area, blade speed, and efficiencies from Figure 23 and assuming axial velocity constant radially. From this information, stator inlet air angles and Mach numbers were calculated for the tip, mean, and hub stations. This gave sufficient information to relate stall and choke characteristics of the stator to the stall and choke limits of the rotor.

The indicated stator angle variation for changes in rotor flow from design incidence to the point of rotor stall are shown in Figure 26. The flow generation rotor flow angle range capabilities shown on Figure 26a and b are greater than the stator stall incidence angle range for the 0.65 or 0.75 D_f stator as indicated in Figures 24 and 25. Therefore, rotor stall should not restrict attainment of stator stall.

At the choke end of the characteristic, it is found that insufficient flow generation rotor flow angle range capability is predicted at low speeds. That is, the rotor will possibly choke before either the 0.65 or 0.75 D_f stator chokes as shown in Figure 27.

Rotor choke may not prevent attainment of choke angles of incidence for the stator. However, rotor choking may result in severe radial shifts of flow which would affect the stator operating conditions adversely. Another significant factor is that the test facility discharges to the atmosphere and choke of the stator and/or rotor may be restricted by the rotor pressure ratio necessary to pass the flow through the system.

On the basis of this study, it was decided that two sets of inlet guide vanes may be required to ensure complete coverage of the stator flow range at low speeds. The design inlet guide vane (initial set) will be used to obtain the major portion of the data and the off-design inlet guide vane (second set) will fill in the near choke region at low speeds if required.

OFF-DESIGN INLET GUIDE VANE DESIGN

A study was conducted to determine the inlet guide vane turning requirements which would provide sufficient flow range margin for the flow generation rotor near choke at low speed. An inlet vane which loaded the rotor was required and several iterations on inlet guide vane flow turning levels indicated that a meanline flow turning of 8.86 degrees is satisfactory. Estimated rotor performance with the off-design inlet guide vanes is shown in Figure 28.

The design point for these inlet vanes was selected at a $W_a\sqrt{\theta}/\delta$ = 84.5 lb/sec (an inlet Mach number of 0.37) and 80% corrected speed which provided rotor design incidence angle at the meanline station. The guide vane outlet whirl distribution is free vortex and the design method used for determining the vane NACA 63-006 airfoil sections was identical with the method described in the Inlet Guide Vane Design subsection. Airfoil properties for the off-design inlet guide vanes are summarized in Table Ib and the loss coefficient distribution is shown in Figure 10b.

Range of the flow generation rotor with the off-design inlet guide vanes for near choke conditions at low speed relative to stator requirements are more than necessary for both stators. Flow range results are shown in Figure 29 for the 0.75 D_f stator. The 0.65 D_f stator results are not shown since Table IV shows that its flow range from design incidence to choke incidence is less than for the 0.75 D_f stator. Although the stall flow range margin is reduced relative to the design inlet guide vane case, as shown in Figure 30, the indicated margin is sufficient for stall of both stators with the off-design inlet guide vanes.

BOUNDARY LAYER CONTROL DESIGN

It has been shown experimentally that boundary layer bleed is a very effective means of preventing boundary layer separation in an adverse pressure gradient. The mechanism of bleed is to remove the momentum deficient air adjacent to the surface. This method of boundary layer control has been applied to the airfoil surface requirements based on selected published results.

PRESSURE DISTRIBUTION

Location of boundary layer separation and subsequent location and sizing of the bleed slot require computation of suction surface boundary layer properties, and these in turn depend directly on the static pressure distribution.

Pressure distributions around the stator vane airfoil surfaces were obtained by interpolating and extrapolating available low speed cascade data from Reference 8. For given chordal locations, plots of pressure coefficient, S, as a function of C_{L_O} with lines of constant angle of attack were prepared as shown in Figure 31. Such plots were drawn to define the pressure coefficients at leading edge, trailing edge, and at several intermediate stations on both suction and pressure surfaces. In addition, the peak pressure coefficient on each surface was defined as well as the location of the peak in terms of percent chord. The plots, Figure 31, were completed for several combinations of inlet air angle and solidity to be able to interpolate to the proper inlet air angle values and to interpolate and extrapolate to the proper levels of solidity. Linear interpolation and extrapolation were used for both inlet air angle and solidity. The final pressure distributions for the 0.75 and 0.65 D_f stators are shown in Figures 32 and 33, respectively.

BOUNDARY LAYER GROWTH AND SEPARATION

The location of the bleed slot along the chord of the vane is chosen in relation to the estimated point of boundary layer separation on the suction surface. The quantity of bleed air required to maintain an attached suction surface boundary layer is also related to the properties of that boundary layer at the bleed slot. Hence, computation of the suction surface boundary layer is essential to the determination of design values for bleed control of separation.

Computation of the compressible turbulent boundary layer was made using an analysis based on Truckenbrodt's energy integral method. This analysis computes the boundary layer history for two-dimensional flow, either axisymmetric or planar. Analysis of the boundary layer is based on an application of the turbulent analog of the Stewartson-Illingworth transformation, as set forth by Culick and Hill in Reference 7.

The boundary layer history for the selected 0.75 and 0.65 stator hub diffusion factor stator vanes was computed based on the static pressure distributions shown in Figures 32 and 33. It was considered sufficiently accurate to assume that free-stream total pressure was constant along the surface and equal to the stator inlet value. It also was necessary to assume that the estimated static pressure distributions remain unchanged even though they reflect a separated boundary layer condition which must change throughout the passage if bleed reattaches the boundary layer.

A summary of the computed boundary layer incompressible form factor, H_i, is shown in Figures 34 and 35 for the 0.75 and 0.65 D_f stator vane suction surface at hub, mean, and tip streamline sections. The value of incompressible form factor for boundary layers at the separation point was established through a series of calculated boundary layer histories for cascade data given in Reference 8. This study indicated a value of $H_i = 2.2$ at the separation point as compared with the usually accepted value of 1.8. This difference in separation point value of form factor may be due to the fact that the boundary layer theory employed herein has neglected vorticity transport effects which are considered to be significant in the cascade flow passage. For this calculational scheme, the separation value of incompressible form factor was taken as 2.2.

In the application of this transformation to the control of the boundary layer formed in the compressible flow around a compressor blade, it is necessary to transform that flow into an equivalent incompressible flow and to subsequently transform design results back to their compressible counterparts. In this transformation the pressure values correspond directly; total temperature is equal to the compressible free stream value; and incompressible flow density is evaluated at P_{t_2} and T_{t_2}. The values of length and velocity are functionally related and the transformed values are unique. Relationships describing properties of the equivalent incompressible flow and thus permitting calculation of the boundary layer properties are:

$$\theta_i = \left[t_e/T_t\right]^3 \theta \tag{15}$$

$$u_i = \left[a_t/a_e\right] u \tag{16}$$

$$Re_{\theta_i} = \left[\mu_e/\mu_t\right] Re_\theta \tag{17}$$

$$u/u_e = \left[y/\delta\right]^{1/n} \tag{18}$$

$$u_i/u_{e_i} = \left[y_i/\delta_i\right]^{1/n} \tag{19}$$

The power law velocity profile exponent n has been correlated through momentum thickness Reynolds number. The values of n from Reference 7 are as follows.

$Re\theta_i$	n
100 to 5000	4
500 to 50,000	5
3000 to 600,000	6
10^5 to 10^7	7

In studying control of the boundary layer by bleed, it was necessary to restart the boundary layer history calculation just downstream of the bleed slot. To start the calculation, boundary layer parameters at the restart calculation point must be specified. With respect to the turbulent boundary layer program, these parameters consist of boundary layer edge properties, momentum thickness, and streamline length in the compressible flow field. Calculation of these boundary layer parameters after bleed is based on an approximate analysis outlined in the following paragraphs.

Compressible flow along an adiabatic wall is assumed with the power law velocity profile in the boundary layer. Figure 36 shows schematically the boundary layer just upstream of a bleed slot, indicating both that portion of the mass flow in the boundary layer which is to be removed by bleed and the remaining portion of the layer which is assumed to constitute the new attached boundary just downstream of the bleed slot. Total mass flow in a unit depth of the boundary layer and mass flow bled away are expressed as:

$$\dot{m}_{BL} = \delta \rho_e u_e \int_0^1 \frac{\rho u}{\rho_e u_e} \, d\left(\frac{y}{\delta}\right) \tag{20}$$

and

$$\dot{m}_b = \delta \rho_e u_e \int_0^{y_b/\delta} \frac{\rho u}{\rho_e u_e} \, d\left(\frac{y}{\delta}\right) \tag{21}$$

respectively. Compressible boundary layer thickness is determined from unpublished data by Prof. H. H. Korst of University of Illinois wherein boundary layer thickness has been correlated as a function of M_e, H, and n. Following the assumption of an adiabatic wall and Prandtl number near unity, constant total temperature in the boundary layer results in the following relationship of static temperature for an ideal gas:

$$t = t_e + u_e^2 \left[1 - \left(\frac{u}{u_e}\right)^2\right] \Big/ 2 g J C_p \tag{22}$$

Equation (22) was used, along with the velocity profile, to evaluate the bleed flow as a function of y_b/δ.

The momentum thickness of the bled boundary layer just downstream of the slot (or restart calculation point) was established using the expression:

$$\theta_b = \delta \left(1 - \frac{y_b}{\delta}\right) \int_{y_b/\delta}^{1} \frac{\rho u}{\rho_e u_e} \left[1 - \frac{u}{u_e}\right] d\left(\frac{y}{\delta}\right) \qquad (23)$$

where the boundary layer thickness δ is the value just upstream of the slot. After specifying the percent of mass flow to be bled from the boundary layer and hence y_b, the momentum thickness θ_b was evaluated using the power law velocity profile, the temperature relationship given by Equation (22), and the value for boundary layer thickness.

With the ability to determine the necessary initial values of boundary layer parameters downstream of the bleed slot, it is possible to compute the history of this new layer to a separation point location or to the trailing edge, whichever location is encountered first. Bleeding off more mass flow increases the value of y_b/δ and leaves the new layer downstream of the bleed slot with less momentum deficiency.

Since the turbulent boundary layer analysis is based on the no-slip velocity condition at the wall, i.e., when y = 0, n = 0 (Figure 36), an incompatibility is built into this approximate boundary layer history assessment after bleeding. The remaining portion of the boundary layer after bleeding has a finite velocity, Figure 36; however, with input values of boundary layer edge properties, velocity power law exponent, and momentum thickness after bleeding, the turbulent flow analysis effectively constructs a boundary layer with no slip velocity at the wall. This new boundary layer has a thickness of δ_b which satisfies the momentum thickness θ_b. There is also a unique displacement thickness given by:

$$\delta_b^* = \delta_b \int_0^1 \left(1 - \frac{\rho u}{\rho_e u_e}\right) d\left(\frac{y}{\delta_b}\right) \qquad (24)$$

The effect of this incompatibility on boundary layer growth after bleed, with varying amounts of bleed, is difficult to establish analytically. It would require an extensive set of calculations for arbitrary static pressure gradients each with varying amounts of bleed. It is intuitive, however, that viscous dissipation can become a predominant factor as δ_b becomes small.

SLOT DESIGN

From a purely aerodynamic point of view, it is desirable to locate the single-bleed slot for the 0.65 and 0.75 D_f stators at the point of separation. While it is well known that a bleed slot can be effective even though located a considerable distance downstream of the uncontrolled separation, more air has to be removed to obtain the same effect as described in Reference 9. If the single-bleed slot is located forward of the uncontrolled separation, then sufficient adverse pressure gradient may exist to still separate the boundary layer.

Since separation occurs at different chordal locations for the hub, mean, and tip sections as shown in Figures 34 and 35, a slot located at these separation points could not be made with a simple planar cut. For simplicity of manufacture, it was decided to specify planar-cut bleed slots and to locate these slots at a constant percent chord along the blade span. Slot location was selected through a compromise, positioning the bleed slot at the average of the maximum and minimum values of computed location (percent chord at $H_i = 2.2$) for hub, mean, and tip sections. This resulted in a slot location of 51.2% for the 0.75 D_f stator and 60% for the 0.65 D_f stator which was within ±10% chord of the computed separation point along the span of both vanes. This is considered to be within the accuracy of the method of boundary layer separation location prediction. Furthermore, the boundary layer can be reattached by slots downstream of separation with increased bleed rates if required as noted in Reference 9.

To determine the required bleed rate for maintaining attached boundary layers to the trailing edge, three different bleed rates were applied to each stator. The bleed rates used were such that the mass in 1/3, 1/2, and 2/3 of the boundary layer height was removed at the slot locations. Bleed mass flow rates, new momentum thicknesses, and new shape factors were calculated for each bleed rate using the described boundary layer growth procedure; boundary layer calculations were then restarted at the bleed slot location for each bleed rate. As Figures 37 and 38 show, in no case did separation occur downstream of the bleed slot before 95% chord ($H_i \leq 2.2$). This indicates that only one bleed slot is needed on each of these stators and that a bleed flow rate corresponding to the mass flow in 1/3 of the boundary layer height at the slot location is adequate.

An examination of Figure 37 shows that increasing bleed rates from the 1/3 boundary layer height mass removal resulted in negligible reduction in incompressible form factor. This is not surprising since approximately

60% of the momentum deficiency is removed at $(y_b/\delta) = 0.33$. Incompressible form factor results for the $(y_h/\delta) = 0.67$ bleed case on the 0.65 D_f stator are greater than for the lower bleed values as shown in Figure 38. It would be expected that the boundary layer growth, as affected by increasing bleed with a fixed pressure distribution, would become asymptotic to a set of boundary layer distribution values without previous history. This would occur at zero momentum thickness. The anomaly indicated in Figure 38 is possibly caused by either the no-slip velocity assumption or by the viscous dissipation becoming predominant in thin boundary layers.

The next step was the selection of slot geometry. The typical configuration is shown in the single-slot schematic of Figure 39. Bleed flow rate values for various slot heights and tangency angles was accomplished by accounting for ram recovery at the slot inlet. The compressible flow data from Reference 10 was used to determine the relationship between bleed flow rate and the ratio of slot inlet total pressure to stator core total pressure. Total pressure at the slot inlet, which includes ram recovery through kinetic energy head, was evaluated as:

$$P_{to} = p_o \left(1 + \frac{\gamma-1}{2} M_o^2\right)^{\frac{\gamma}{\gamma-1}} \tag{25}$$

where the slot inlet Mach number is assumed to be:

$$M_o = M_{eo} \cos \psi \tag{26}$$

This approximate method is considered to be optimistic since bleed flows of 25 to 30% of the boundary layer flow for a 0.33 δ thickness removal represents total pressures nearer to local static. As a net result, the slot width calculated for a given bleed flow and pressure differential will be smaller than the actual width required. This was considered favorable since facility vacuum capability was greater than required. Therefore, in the event that boundary layer bleed rate requirement was less than 0.33 δ , the smaller slot width would still provide a range of facility vacuum levels for positive bleed control.

Flow rate through a narrow rectangular slot or airfoil was calculated from results of Reference 10 by:

$$\dot{m}_b = K_T K_A \frac{P_t A}{\sqrt{T_{t_2}}} \tag{27}$$

where the experimental flow coefficient is defined as:

$$K_T = 2.06 \left[\left(\frac{P_{t_{core}}}{P_{t_o}} \right)^{1.43} - \left(\frac{P_{t_{core}}}{P_{t_o}} \right)^{1.71} \right]^{0.5} \qquad (28)$$

The aspect ratio coefficient, K_A, corrects for the slot end wall effects. In the slot sizing calculations reported herein, K_A was taken as 0.95. Reference 10 tabulates these values as a function of slot width to area ratios. Portions of the blade span assigned to the hub, mean, and tip section slots are shown in Figure 40.

Slot widths of 0.02, 0.03, and 0.04 inches and slot angles of 15, 30, and 45 degrees were analyzed for both stators. The slot bleed flow results are shown in Figures 41 and 42 for each stator and are plotted versus stator row design inlet total pressure to core total pressure ratio. This total pressure ratio is meaningful for evaluation of the slot configuration with respect to the facility vacuum capability. The core total pressure was assumed to be constant spanwise. Also shown in Figures 41 and 42 is the mass flow for removal of boundary layer mass corresponding to 33% of the boundary layer thickness.

For a slotted vane, there exists a critical flow limit on the bleed flow. This is the flow which the minimum area in the bleed system will pass at Mach 1.0. For the slotted vanes designed here, the minimum area is considered to be the area subtended by the core cross section and inside diameter of the trunnion tip. This subtended area is shown schematically in Figure 43 and has an area of 0.20 square inches. Twelve of the 38 stator vanes contain 5-vane surface static pressure tube leads passing through the subtended area as shown in Figure 43. These five tubes are tack welded to the inside surface of the trunnion with a metal strap resulting in an area blockage of 0.02 square inches.

Resultant maximum bleed flows through the minimum area based on the core total pressure at that bleed rate are shown in Figures 41 and 42. Since the facility minimum vacuum pressure capability just downstream of the minimum area is estimated at 4.4 psia, the stator inlet total pressure to vacuum pressure ratio is greater than 2.5. Therefore, the maximum bleed flow rate can be limited by the bleed slots or by the blade trunnion tip area shown in Figure 43.

A slot width of 0.030 inches and a slot angle of 45 degrees was chosen for both the single-slot 0.65 and 0.75 D_f stators. This choice was made to

ensure that bleed flow would be sufficient to prevent separation and that bleed flow would be sensitive to core total pressure. The single-slot configurations are summarized in Figure 39.

For the objective of increasing stall free operating range over the single-slot 0.75 D_f stator, a three-slot bleed design was made for the second 0.75 D_f stator vane. An initial design was based on the principle of providing a distributed but uniform bleed effect from 41 to 61% chord. This design was subsequently discarded as a result of mid-span suction surface static pressure measurements of an unslotted 0.75 D_f stator in Reference 11. Experimental surface pressure coefficients from this test are shown in Figure 44. The pressure distribution shown in Figure 44b indicated that a bleed slot at about 25% chord could possibly provide additional range at incidences greater than zero degrees. Slot location selections were then set at 25, 41, and 61% chord.

In the triple-slot design, the first two bleed slots are required to maintain attached flow to the following slot. The third slot is required to maintain attached flow to the 95% chord station or beyond. Required bleed flows can be minimized on this basis such that the incompressible form factor at the next slot or 95% chord station approached the separation value of 2.2. It was considered sufficient, however, to apply the 1/3 boundary layer height mass removal since the core total pressure and, therefore, bleed flow rate can be varied experimentally. The total bleed flow rate was found to be 1.5% of the primary flow for $(y_b/\delta) = 0.33$ and incompressible form factors did not exceed 1.8.

Bleed slot sizing for the three slots in series configuration was based on the conditions that (1) slot heights will be equal, (2) slot angles will be 45 degrees to the surface tangent, and (3) core total pressure is constant chordwise and spanwise. A series of calculations were then made on slot width over a range of core total pressures as described for the single-slot design.

Results of the bleed flow calculations are shown in Figure 45. A slot width of 0.009 inches for each slot was selected for the same assurances of sufficient bleed, less than critical value, and sensitivity to core total pressure as in the single slot case. The three slot configuration for the 0.75 D_f stator is summarized in Figure 39.

MECHANICAL DESIGN AND STRESS ANALYSIS

Mechanical design of the test hardware for this project involved three basic areas:

- Compressor blading
- End-wall boundary layer bleed system
- Required supporting structures and equipment

These areas will be discussed first in regard to rig construction details and secondly in regard to stress and vibration analysis.

RIG DESIGN

The general layout of the test hardware is shown in Figure 46. Bearing loads are carried to the external structure through radial struts of 410-type stainless steel at inlet and exit. The inlet strut is aerodynamically shaped and located sufficiently far away from the blading to provide negligible flow disturbance into the inlet guide vanes. The exit strut is essentially radial and made from circular rods. Hub wall support struts are located as far downstream as mechanically possible and serve as hub wall bleed ducts. Therefore, a minimum internal area was required to pass the flow. The leading and trailing edge radii of the bleed strut are equal to half the strut thickness. Thrust loads are carried by the rear ball bearing which was sized for a thrust load of 1320 pounds and a radial load of 150 pounds with life expectancy greater than 20,000 hours at 100% speed. The forward roller bearing has a life expectancy of one million hours at three hundred pounds radial load and 110% speed. This bearing and its related carbon face seals are production parts acquired from the Model 501-D13 commercial engine program.

The rotor is composed of the basic wheel disk, to which the blades are attached, with coned shafting on each side. This type of design gives excellent vibrational characteristics with low weight. The wheel disk and rotor blades are of 410 material and the coned shafts are of a D-6 material for greater strength. Blade attachment is by means of conventional dovetails with pins to restrict axial movement in the slots.

The hardware has been designed to permit rapid changes of all case components including inlet guide vanes, stator vanes, and both inner and outer wall bleed system bands. The front and rear supports are held in relation to each other through an external tram rail support system. The case assembly is split vertically and is supported from the tram rail system. The cases may be removed for stator vane configuration changes with the rig still mounted on the test stand without destroying rotor alignment.

The inlet guide vanes, also of 410 material, have been segmentized to permit vane changes without removing the cases. The 34 vanes are divided into six segments of three vanes each and four segments of four vanes each. Each segment may be removed from outside the case. The vanes are individually adjustable within each segment.

The stator vane mechanical design provides end-wall boundary layer bleed in the vicinity of the stators and permits manual resetting of the stator blade angle. This is accomplished by attach coaxial circular section of the bleed wall skin to the stator vane assem This circular disk is recessed into the remainder of the bleed wall sembly, forming an essentially complete circumferential strip of s wall at both hub and tip of the vanes. Bleed air passes through the porous wall into circumferential cavities. External hose fittings connected to the tip cavity are provided between each two successive stator vanes. Equal length hoses connect these fittings to a test stand vacuum header. The hub bleed air is ducted from the collection cavity to the hub wall struts and out through these hollow struts to a second vacuum header.

Each of the bleed walls was required to pass 2.5% of the compressor inlet flow within a pressure drop of 5 psi and still provide test facility margin on vacuum capacity. A variety of commercial porous materials were investigated for this application, but none met the design requirements. Therefore, it was necessary to fabricate special material. A thin (0.010-inch) sheet of perforated metal with holes of 0.0135-inch diameter was chosen for the bleed walls. This hole size could be photo-etched into the metal conveniently, and enough holes were included so that essentially uniform mass removal effects on the boundary layer were produced. Final hole spacing of 0.062 inch on centers was determined by flow testing.

The stator vanes are cast from Inco 713 material. Castings were chosen because of the hollow vanes and the number of pieces required. The Inco 713 material was chosen because of known characteristics with ceramic cores and dimensional stability for this type of casting. The oversize hollow tip trunnion on the stator vanes is provided to pass the vane suction surface bleed. Equal length hoses connect these trunnions to a third vacuum header.

An abradable coating on the compressor cases over the rotor blade tips permits low running clearances between blade tips and case. The rotor is designed with an interference fit such that the rotor blade tip will run into the abradable coating at design speed. Radial growth due to centrifugal force and temperature expansion are considered. Nominal design clearance for this rotor is -0.0025 inch at 100% speed and -0.0045 inch at 110% speed. Nominal static clearance is 0.0075 inch.

STRESS AND VIBRATION ANALYSIS

As a part of the mechanical design of the test rig, stress and vibration analyses were conducted for the critical components. These analyses included the rotor system, stator vanes, and bearing supports with related structural components.

Rotor System

The rotor blades were analyzed to determine stresses due to centrifugal and gas bending loads. A computer program that calculates blade element air loads and section properties at multiple radial locations was used in the analysis. Air loads were integrated spanwise and actual airfoil section properties were used to mathematically reproduce the relationship between fluid forces and blade geometry. Gas bending stresses were calculated at the leading and trailing edges and at the crown of the blade. The results of this analysis given in Figure 47 show that steady state blade element stresses are well within the design limits for the 410 stainless material which has a yield strength of 102,000 psi.

Additional blade calculations were made to determine first and second bending and first torsional vibration frequencies. The overall range of first bending, shown in Figure 48, is 405 to 525 cps between zero and 110% design speed. First torsion frequency is practically constant and is 1135 cps at the 110% speed point. Second mode bending frequencies varied from 1620 to 1750 cps. Lines representing engine orders are shown to permit identification of any excitation frequencies within the operating range such as inlet guide vane wakes or upstream bearing support struts. All calculated bending frequencies are above the third engine order line and are adequate in view of all projected disturbances within the rig design.

The blade attachment is a single-serration dovetail. Stresses calculated in the dovetail are listed in Table VI.

The rotor wheel with attached conical drive shaft was sized to reflect conservative wheel stresses and to limit rim radial growth to values acceptable to blade tip aerodynamic performance characteristics. Final stresses and rim growth are shown in Figure 49. The wheel and conical drive shaft were analyzed together as an integral system with the interaction of forces and moments considered. The free-state radial growth of the conical shafting was greater than the equivalent radial attachment point on the wheel with the result that the shafting was piloted to the wheel. This design feature was utilized to ensure that the bolt attachment was not loaded in shear. Restraining the shafting by the wheel pilot developed the shafting stresses shown in Figure 50. These calculated stresses are also well within allowable stress limits of the material which has a yield strength of 200,000 psi at the temperature to which it is subjected in this application.

Stator Blades

The bleed type vane geometries represent airfoil sections which are slotted radially at multiple locations and, in many cases, reflect unsupported airfoil strips. The first requirement for overall vane stress assessment was to assume the vanes to be hollow but with a continuous wall and calculate the bending stress and natural frequency for pinned hub attachments. The calculated frequencies are well above known excitation engine orders and the bending stresses are quite low. Calculations for both the 0.65 and 0.75 diffusion factor blading are presented in Figures 51 through 54.

The second requirement was to examine the stresses and vibration frequency of the strips formed by the single continuous slot, considering the end and side fixities as applicable. The results of this investigation prompted a deflection analysis to determine the change in slot gap dimensions under operational conditions (Table VII).

This analysis indicates that basically the bending stresses and natural frequency of these airfoil strips lie in an area of little concern. The percent change in the static gap dimensions, shown in Table VII, was in most instances considered excessive with respect to aerodynamic characteristics for all slotted airfoils. The decision was made that all airfoil slots were to have two intermediate ties. This shortening of the strips reduced the deflection directly by the third power of the length change and increased the frequency by the second power. All configurations were determined to be structurally sound.

Bearing Supports

The radial spring rates of the front and rear bearing supports were calculated using a computerized solution of spoked, stiffened concentric cylinders. The results of this calculation provided a spring rate of 1.3×10^6 pounds/inch at the front and 3.4×10^6 pounds/inch at the rear support. Using these elastic bearing support rates, the system critical speed is 17,800 rpm or 114% above design speed. Figure 55 presents the rig system critical speed in terms of a fixed spring rate of the rear support versus variable front support rates. In addition, the external rig mounting system was investigated to determine the elastic support content and was found to be almost completely rigid.

Allison design practice specifies that calculated system critical speed must be in excess of 140% design speed. This requirement has been satisfied.

REFERENCES

1. Miller, M. L. and Chapman, D. C., Single-Stage Experimental Evaluation of Boundary Layer Blowing Technique for High Lift Stator Blades, I - Compressor Design, Allison Div, GM, NASA-CR-54564, February 1968.
2. Dunavant, J. C., Cascade Investigation of a Related Series of 6 Percent Thick Guide Vane Profiles and Design Charts, NACA TN 3959, 1954.
3. Lieblein, S., "Loss and Stall Analysis of Compressor Cascades," ASME Journal Basic Engineering, September 1959, pp 387-400.
4. Aerodynamic Design of Axial Flow Compressors, NASA SP-36, 1965.
5. Lieblein, S. and Sandercock, D., Compressibility Correction for Turning Angles of Axial-Flow Inlet Guide Vanes, NACA TN 2215, 1950.
6. Lieblein, S. and Ackley, R., Secondary Flows in Annular Cascades and Effects on Flow in Inlet Guide Vanes, NACA RM E51G27, 1951.
7. Culick, F. E. and Hill, J. A. F., "A Turbulent Analog of the Stewart-son-Illingworth Transformation," Journal Aero Science, Vol 25, pp 259-262.
8. Herrig, L. J., Emery, J. C., and Erwin, J. R., Systematic Two-Dimensional Cascade Tests of NACA 65-Series Compressor Blades at Low Speeds, NACA TN-3916, 1957.
9. Goldstein, S., "Modern Developments in Fluid Mechanics," Vol. II, Oxford Press, 1957, pp 532-533.
10. Neprud, T. S., "Pneumatic Flow through Narrow Slots," Machine Design, Vol 36, No. 5, pp 163.
11. Miller, M. L. and Beck, T. E., Single-Stage Experimental Evaluation of Boundary Layer Blowing Techniques for High Lift Stator Blades, II - Flow Generation Rotor and Single-Slotted 0.75 D_f Stator Blade Test, Allison Div, GM, NASA-CR-54565, 1968.

APPENDIX

COMPRESSOR FLOW ANALYSIS

The stage velocity diagrams were calculated taking into account radial gradients of entropy and radial velocity. The analysis was made on a between blade row basis. Thus, the streamlines were assumed to form a smooth curve joining the streamline points calculated in the between row planes. Three axial stations upstream and three stations downstream of the compressor are also included in the calculation to help define the streamlines.

Assuming axisymmetric flow between blade rows, the equation of radial equilibrium is:

$$JgC_p \frac{\partial T_t}{\partial R} = Jgt \frac{\partial S}{\partial R} + V_\theta \frac{\partial V_\theta}{\partial R} + \frac{V_\theta^2}{R} + V_z \frac{\partial V_z}{\partial R} - V_z \frac{\partial V_r}{\partial z}$$

The entropy gradient term, $\frac{\partial S}{\partial R}$, is modified by using the following relationship. The entropy difference for a perfect gas between two conditions is:

$$S_2 - S_1 = \int_1^2 C_p \frac{dT_t}{T_t} - \frac{\mathcal{R}}{J} \ln \frac{P_{t_2}}{P_{t_1}} \text{ or for constant } C_p$$

$$S_2 - S_1 = C_p \ln \frac{T_{t_2}}{T_{t_1}} - \frac{\mathcal{R}}{J} \ln \frac{P_{t_2}}{P_{t_1}} = \frac{\mathcal{R}}{J} \frac{\gamma}{(\gamma-1)} \ln \frac{T_{t_2}}{T_{t_1}} - \frac{\mathcal{R}}{J} \ln \frac{P_{t_2}}{P_{t_1}}$$

or, in this case, when integrating from a reference station R_i to R:

$$\frac{\partial S}{\partial R} = \frac{\mathcal{R}}{J} \frac{\partial}{\partial R} \left\{ \ln \left[\frac{(T_t/T_{t_i})^{\frac{\gamma}{\gamma-1}}}{P_t/P_{t_i}} \right] \right\}$$

The radial velocity term, $V_z \frac{\partial V_r}{\partial z}$, is difficult to evaluate in this form because the partial differential of V_r with respect to z is by definition at constant radius while the rest of our calculations are on a streamline basis. For that reason, the curvature term is modified in the following manner:

$$\left(\frac{\partial V_r}{\partial z}\right)_{sl} = \left(\frac{\partial V_r}{\partial z}\right)_R + \left(\frac{\partial V_r}{\partial R}\right)_z \left(\frac{\partial R}{\partial z}\right)_{sl}$$

but: $V_r = V_z\left(\frac{\partial R}{\partial z}\right)_{sl}$

so: $\left(\frac{\partial V_r}{\partial z}\right)_R = V_z\left(\frac{\partial^2 R}{\partial z^2}\right)_{sl} + \left(\frac{\partial R}{\partial z}\right)_{sl}\left(\frac{\partial V_z}{\partial z}\right)_{sl} - \left\{\frac{\partial\left[V_z\left(\frac{\partial R}{\partial z}_{sl}\right)\right]}{\partial R}\right\}_z \left(\frac{\partial R}{\partial z}\right)_{sl}$

Therefore, the radial velocity gradient or curvature term is:

$$V_z\left(\frac{\partial V_r}{\partial z}\right)_R = {V_z}^2\left(\frac{\partial^2 R}{\partial z^2}\right)_{sl} + V_z\left(\frac{\partial R}{\partial z}\right)_{sl}\left(\frac{\partial V_z}{\partial z}\right)_{sl}$$

$$-V_z\left\{\frac{\partial\left[V_z\left(\frac{\partial R}{\partial z}_{sl}\right)\right]}{\partial R}\right\}_z \left(\frac{\partial R}{\partial z}\right)_{sl}$$

To find the radial variation of axial velocity between blade rows, the radial equilibrium equation with the new terms for entropy gradient and curvature is integrated from R_i to the next radius, which provides the following equation:

$$V_z^2 - {V_z}_i^2 = 2gJC_p\,(T_t - T_{t_i}) - (V_\theta^2 - V_{\theta\,i}^2) - 2\int_{R_i}^{R}\frac{V_\theta^2}{R}dR$$

$$- 2g\mathcal{R}\int_{R_i}^{R} t\,\frac{\partial}{\partial R}\left\{\ln\left[\frac{(T_t/T_{t_i})^{\frac{\gamma}{\gamma-1}}}{P_t/P_{t_i}}\right]\right\}dR + 2\int_{R_i}^{R}\left\{V_z^2\left(\frac{\partial^2 R}{\partial z^2}\right)_{sl}\right.$$

$$\left. + V_z\left(\frac{\partial R}{\partial z}\right)_{sl}\left(\frac{\partial V_z}{\partial z}\right)_{sl} - V_z\left\{\frac{\partial\left[V_z\left(\frac{\partial R}{\partial z}\right)_{sl}\right]}{\partial R}\right\}_z \left(\frac{\partial R}{\partial z}\right)_{sl}\right\}dR$$

where subscript i refers to conditions at a reference station or radius.

The conditions to solve this equation are given to the computer in the following way. Case and hub geometry for all axial stations are specified, including three stations before the first rotor or IGV inlet and three stations after the last stator exit. These six extra axial stations are to better define the flow path at the compressor inlet and exit. The geometry is given as blockage factor, hub radius, and tip radius versus compressor axial length. The increment of flow in each streamtube is specified to allow the computer to obtain intermediate radii. Mass flow, rpm, γ (ratio of specific heats), $\mathcal{R}$ (gas constant) and C_p (specific heat at constant pressure) are also specified. The following items are prescribed in polynomial form as function of radius:

- Total temperature--for first four axial stations (including IGV inlet)
- Total pressure—same as total temperature
- Δ total temperature—across each rotor versus radius at rotor exit
- Rotor adiabatic efficiency—at each rotor exit
- Stage adiabatic efficiency—at each stator exit
- Tangential velocity—inlet to each rotor and at the last stator exit

Assuming the radial velocity is zero at the inlet of the first axial station (three ahead of rotor or IGV inlet), the program can proceed through the machine solving radial equilibrium using an iterative method. After each pass through the radial equilibrium equation, continuity is checked by the following equation:

$$W_a = 2\pi \int_{R_H}^{R_T} (\rho V_Z R)\, dR \quad \text{where} \quad \rho = \frac{P_t}{\mathcal{R} T_t}\left(1 - \frac{(V_z^2 + V_\theta^2 + V_r^2)}{2gJC_pT_t}\right)^{\frac{1}{\gamma-1}}$$

If the velocity distribution obtained by the radial equilibrium equation does not satisfy continuity, the radial distribution is kept the same, but the level is changed to satisfy continuity. Another pass is then made through the radial equilibrium equation using the new value for the reference velocity. This process is continued until both the continuity and radial equilibrium equations are satisfied.

Table I.

Inlet guide vane design parameters.

a. Design inlet guide vanes

R_1 (inches)	σ	c (inches)	$\Delta\beta_{des}$ (degrees)	$C_{L_{O_{des}}}$	α_{des} (degrees)	t/c	E_C (degrees)	E_{SF} (degrees)
9.860	1.500	2.733	28.35	1.41	19.0	0.06	0.68	1.00
11.145	1.327	↓	25.98	1.24	16.7	↓	0.30	0.00
12.430	1.190	↓	23.86	1.19	15.3	↓	0.12	0.04
13.715	1.078	↓	22.06	1.15	14.2	↓	0.00	0.05
15.000	0.986	↓	20.47	1.06	12.3	↓	-0.05	-1.00

b. Off-design inlet guide vanes

9.860	1.500	2.733	11.13	0.57	7.5	0.06	0.72	0.00
11.145	1.327	↓	9.87	0.53	6.5	↓	0.65	↓
12.430	1.190	↓	8.86	0.51	6.0	↓	0.57	↓
13.715	1.078	↓	8.05	0.48	5.5	↓	0.54	↓
15.000	0.986	↓	7.37	0.46	5.0	↓	0.49	↓

Table II.

Rotor blade properties.

R_2/R_{2T}	L_{ax} (inches)	c (inches)	σ	i_{des} (degrees)	$\delta°$ (degrees)	ϕ (degrees)	$\gamma°$ (degrees)	t/c	D_f	Choke margin (%)	κ_1 (degrees)	κ_2 (degrees)
1.0	1.679	2.875	1.373	0	4.603	12.830	54.26	0.032	0.414	6.2	60.68	45.84
0.920	1.894	↓	1.493	↓	5.377	17.306	48.80	0.0333	0.417	7.7	57.45	40.15
0.832	2.180	↓	1.649	↓	6.611	24.946	40.68	0.0393	0.424	10.2	53.15	28.21
0.769	2.405	↓	1.785	↓	7.607	32.389	33.21	0.0517	0.427	11.7	49.41	17.01
0.699	2.644	↓	1.965	↓	7.802	41.897	23.10	0.078	0.421	12.0	44.05	2.15

Table III.

Incidence angle - camber variation for 65-series airfoil with 53.9° flow turning, 1.7 solidity, and a=1 meanline.

a. Method 1. Deviation at equivalent 0° incidence

			Evaluated at β_{2E}					
i (degrees)	β_2 (degrees)	β_3 (degrees)	β_{2E} (degrees)	$m_{\sigma=1}$	b	$(\delta_o^\circ)_{10}$ (degrees)	ϕ (degrees)	C_{L_O}
0	53.9	0	53.9	0.245	0.747	2.12	67.1	2.67
-4	53.9	0	57.9	0.260	0.705	2.50	73.5	2.92
-6	53.9	0	59.9	0.269	0.682	2.73	77.0	3.06
-8	53.9	0	61.9	0.277	0.657	2.97	80.7	3.20

b. Method 2. Deviation at actual incidence

			Evaluated at $\beta_2 = 53.9°$				
i (degrees)	β_2 (degrees)	β_3 (degrees)	$m_{\sigma=1}$	b	$(\delta_o^\circ)_{10}$ (degrees)	ϕ (degrees)	C_{L_O}
0	53.9	0	0.245	0.747	2.12	67.1	2.67
-4	53.9	0	0.245	0.747	2.12	72.0	2.86
-6	53.9	0	0.245	0.747	2.12	74.3	2.95
-8	53.9	0	0.245	0.747	2.12	76.7	3.05

Table IV.

Stator aerodynamic and airfoil geometric properties—65-series airfoil on circular arc meanline.

c = 3.00 inches, t/c = 10%

D_{f_H}	R_3 (inches)	ϕ (degrees)	$\gamma°$ (degrees)	σ	i_{des} (degrees)	$\delta°$ (degrees)	i_{stall} (degrees)	i_{choke} (degrees)	O (inches)	s (inches)	M_2	X_O/c (percent)	κ_2 (degrees)	κ_3 (degrees)
	10.64	74.8	19.5	1.705	-3	17.9	0	-6.0	1.100	1.759	0.748	31	56.9	-17.9
	11.66	72.2	18.4	1.556	↓	17.7	↓	—	—	—	0.701	—	54.5	-17.7
0.75	12.55	70.7	17.65	1.446		17.7		-10.1	1.424	2.075	0.666	33	53.0	-17.7
	13.82	70.2	17.0	1.313		18.1		—	—	—	0.626	—	52.1	-18.1
	15.00	72.4	16.1	1.210		20.1		-17.4	1.800	2.480	0.600	35	52.3	-20.1
	10.64	37.4	32.25	1.705	+3	9.3	+8	+0.8	1.078	1.759	0.748	39	50.9	13.5
	11.66	37.6	29.7	1.556	↓	9.3	↓	—	—	—	0.701	—	48.5	10.9
0.65	12.55	38.0	28.0	1.446		9.5		-3.6	1.416	2.075	0.666	40	47.0	9.0
	13.82	39.3	26.45	1.313		10.2		—	—	—	0.626	—	46.1	6.8
	15.00	42.4	25.10	1.210		11.6		-11.4	1.800	2.480	0.599	43	46.3	3.9

Table V.

Comparison of stator exit flow angles calculated using Method 2 and design flow angles.

D_{f_H}	R_3 (inches)	ϕ (degrees)	β_2 (degrees)	σ	$\beta_2 - \beta_3$ (degrees)	β_3 (degrees)	$\beta_{3_{des}}$ (degrees)	$\beta_{3_{des}} - \beta_3$ (degrees)
0.75	10.64	74.8	53.9	1.705	57.5	-3.6	0	3.6
	11.66	72.2	51.5	1.556	55.2	-3.7	↓	3.7
	12.55	70.7	50.0	1.446	53.8	-3.8		3.8
	13.82	70.2	49.1	1.313	53.0	-3.9		3.9
	15.00	72.4	49.3	1.210	53.6	-4.3		4.3
0.65	10.64	37.4	53.9	1.705	32.2	21.7	22.8	1.1
	11.66	37.6	51.5	1.556	32.3	19.2	20.2	1.0
	12.55	38.0	50.0	1.446	32.7	17.3	18.5	1.2
	13.83	39.3	49.1	1.313	33.6	15.5	17.0	1.5
	15.00	42.4	49.3	1.210	35.5	13.8	15.5	1.7

Table VI.

Rotor blade dovetail serration stresses.

Item	Calculated stress (psi)	Allowable stress (psi)	Safety factor
Projection shear	13,800	66,000	4.78
Contact bearing	16,100	242,000	15.0
Tensile	8,400	121,000	14.5
Projection bending	29,700	121,000	4.05

Table VII.

Stator vane slot deflection and natural frequencies without slot ties.

D_{f_H}	Type	Deflection (inches)	Static slot height (inches)	Change in slot height (percent)	Natural frequency (cps)
0.75	Single slot	(1) 0.00069 (open)	0.0315	2.2	4650 (A)
0.75	Triple slot	(1) 0.00223 (closed)	0.0105	21.2	
		(2) 0.00719 (closed)	0.0105	68.5	1129 (A)
		(3) 0.0096 (open)	0.0105	91.5	775 (B)
0.65	Single slot	(1) 0.00077 (open)	0.0315	2.4	4100 (A)

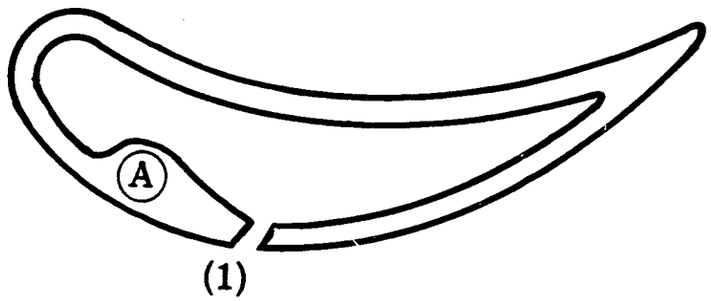

Single-slot vane

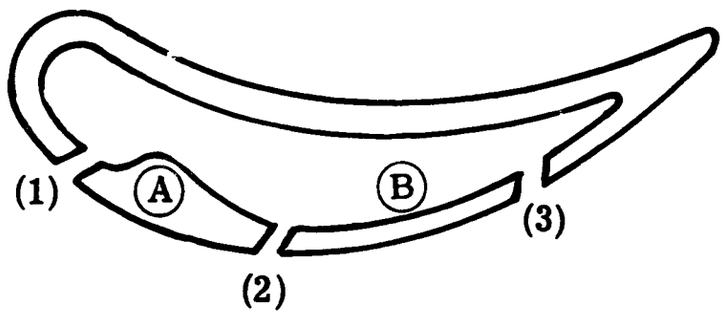

Triple-slot vane

5658-61

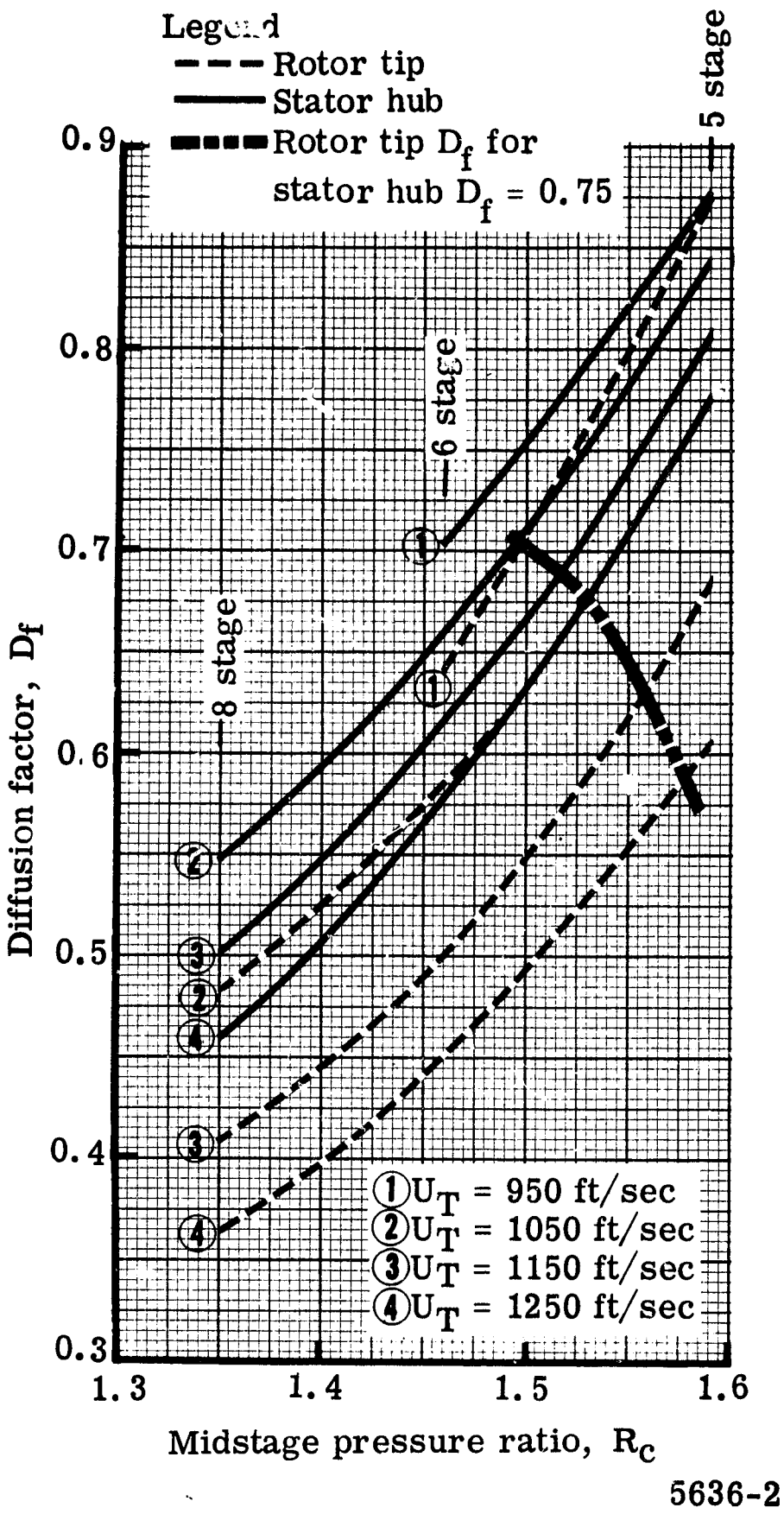

Figure 1. Midstage stator hub and rotor tip loadings for $(R_H/R_T)_2 = 0.7$.

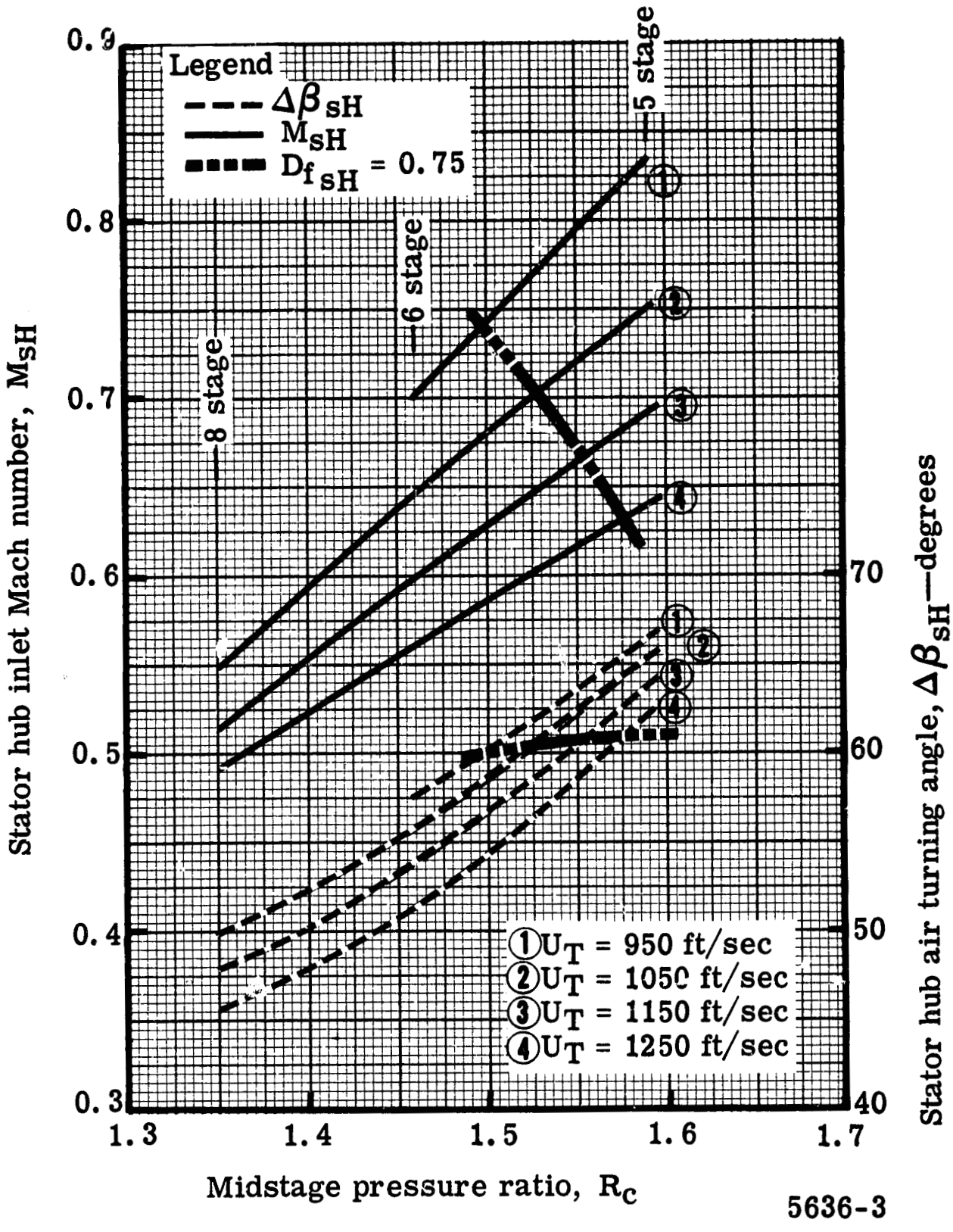

Figure 2. Preliminary design study—stator hub Mach number and turning angle.

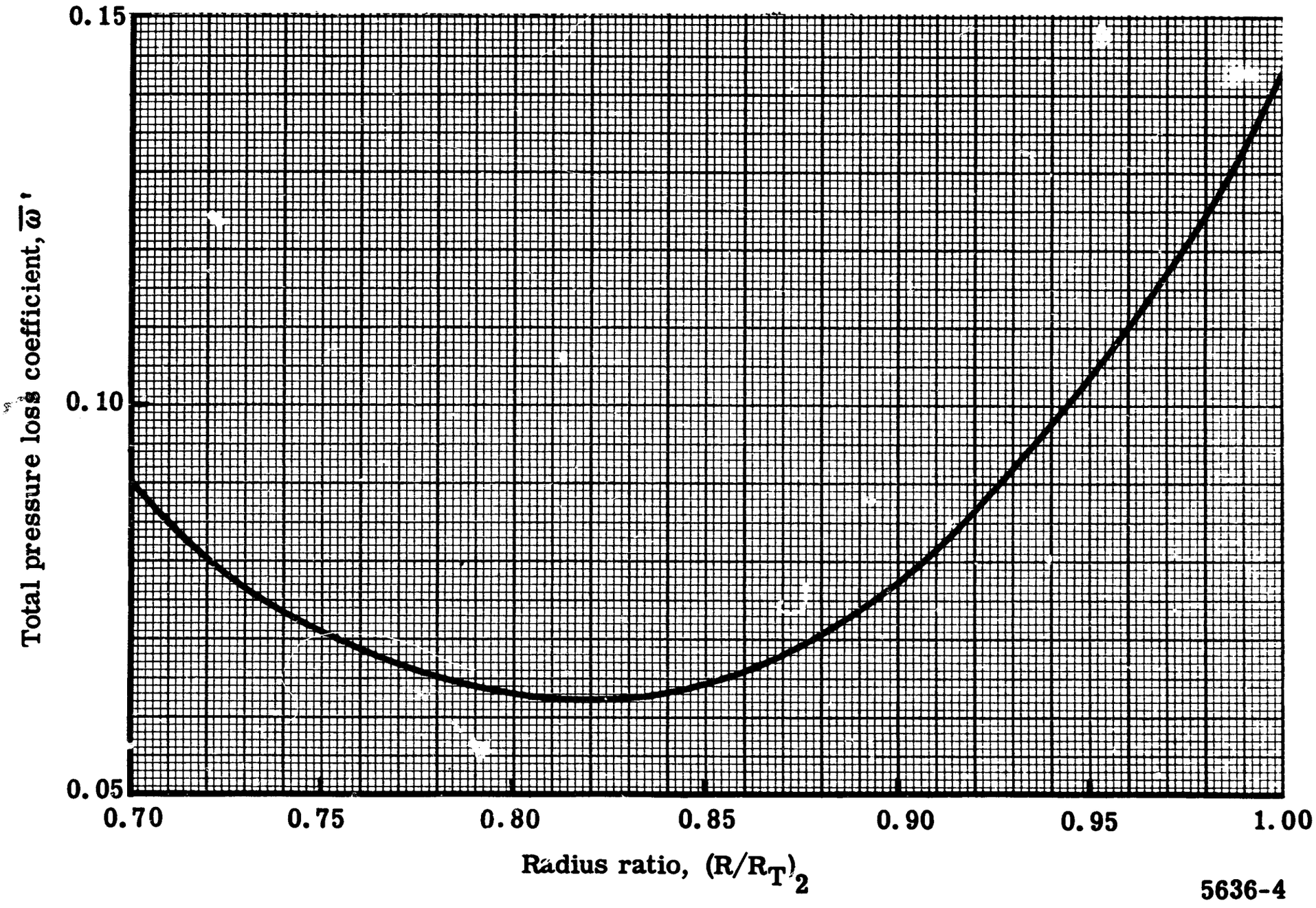

Figure 3. Rotor design total pressure loss coefficient distribution.

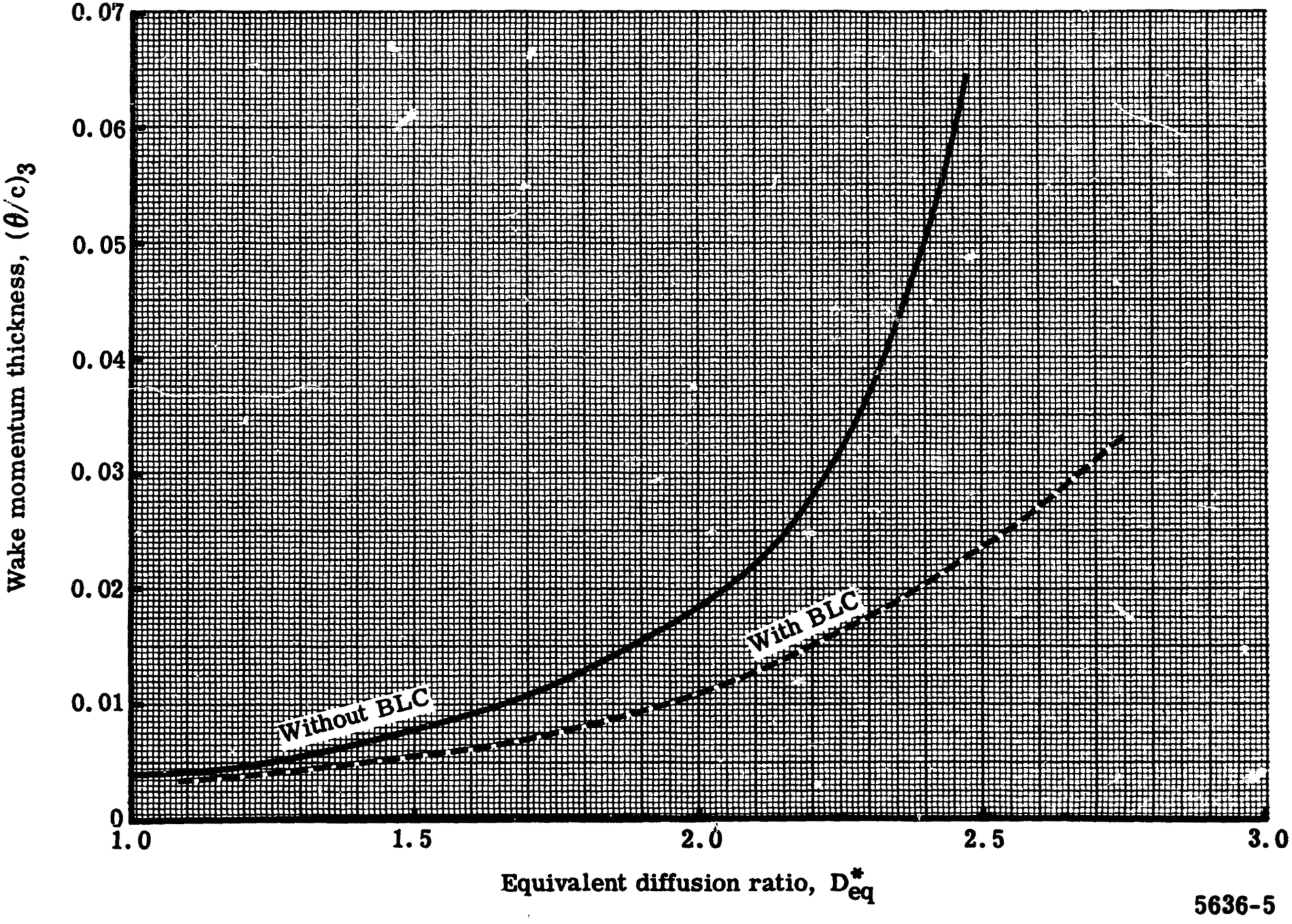

Figure 4. Wake momentum thickness with and without boundary layer control.

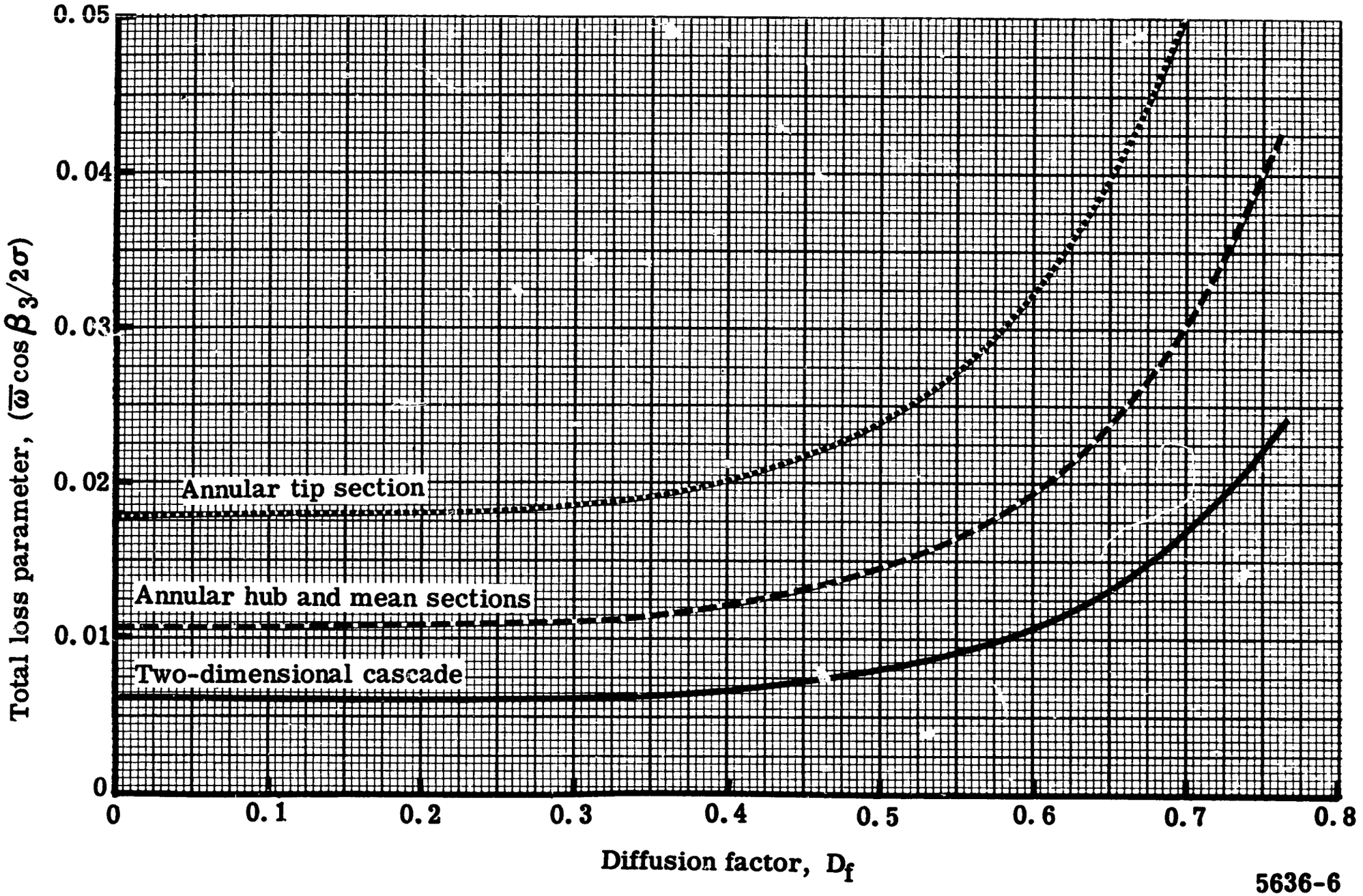

Figure 5. Comparison of annular and two-dimensional cascade losses.

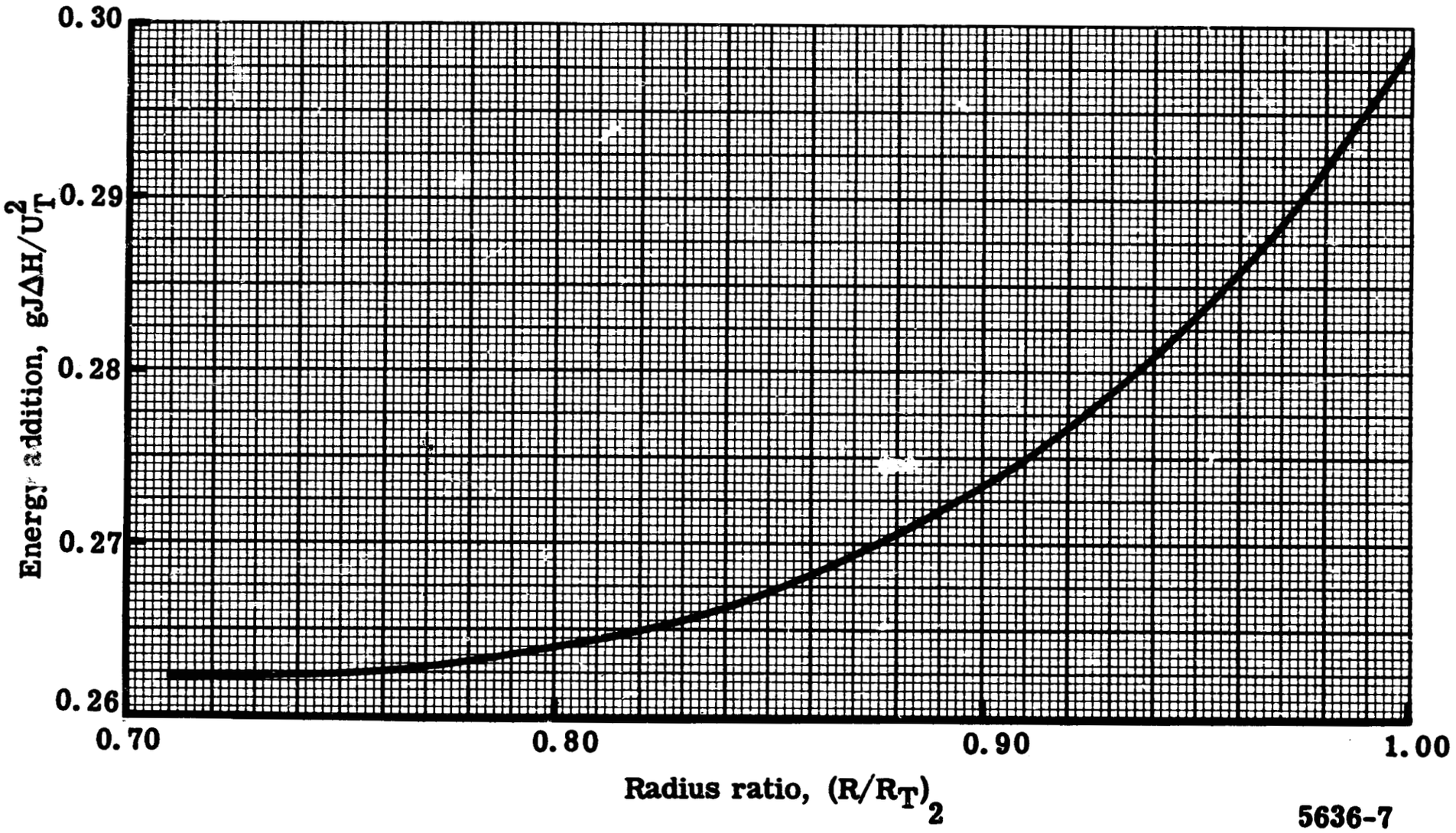

Figure 6. Rotor design radial work gradient.

Figure 7. Velocity diagrams for flow generation rotor.

M_{z_2} = 0.392
M_{z_3} = 0.372
M_2 = 0.600
M_3 = 0.372
D_f = 0.680

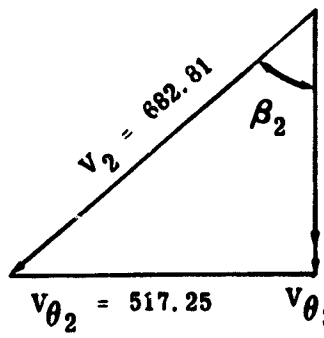

V_{z_2} = 445.73
V_{z_3} = 432.71
V_3 = 432.71

β_2 = 49.26°
β_3 = 0°
R_2 = 15.000
R_3 = 15.000
a_2 = 0°
a_3 = 0°

Tip section

M_{z_2} = 0.410
M_{z_3} = 0.364
M_2 = 0.626
M_3 = 0.364
D_f = 0.691

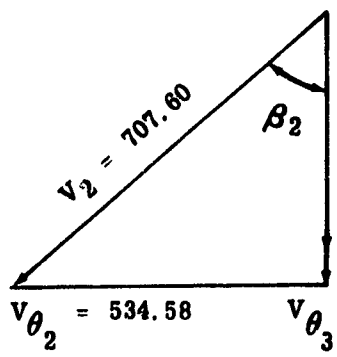

V_{z_2} = 463.53
V_{z_3} = 422.26
V_3 = 422.26

β_2 = 49.08°
β_3 = 0°
R_2 = 13.817
R_3 = 13.869
a_2 = 0° 56'
a_3 = 0° 33'

Intermediate

M_{z_2} = 0.428
M_{z_3} = 0.365
M_2 = 0.666
M_3 = 0.365
D_f = 0.702

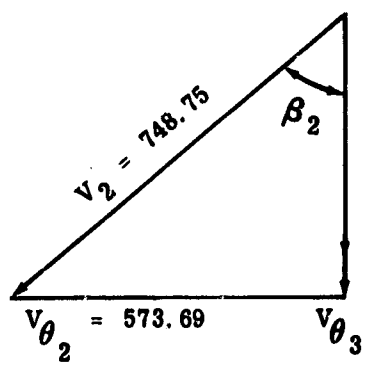

V_{z_2} = 480.87
V_{z_3} = 421.86
V_3 = 421.86

β_2 = 50.04°
β_3 = 0°
R_2 = 12.558
R_3 = 12.630
a_2 = 1° 59'
a_3 = 0° 47'

Mean section

M_{z_2} = 0.437
M_{z_3} = 0.359
M_2 = 0.701
M_3 = 0.359
D_f = 0.722

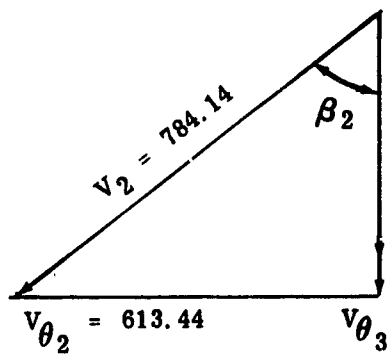

V_{z_2} = 487.87
V_{z_3} = 415.42
V_3 = 415.42

β_2 = 51.51
β_3 = 0°
R_2 = 11.646
R_3 = 11.722
a_2 = 2° 47'
a_3 = 0° 49'

Intermediate

M_{z_2} = 0.440
M_{z_3} = 0.345
M_2 = 0.748
M_3 = 0.345
D_f = 0.756

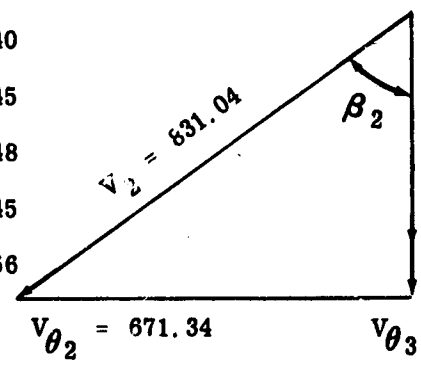

V_{z_2} = 488.91
V_{z_3} = 399.52
V_3 = 399.52

β_2 = 53.95°
β_3 = 0°
R_2 = 10.636
R_3 = 10.767
a_2 = 3° 30'
a_3 = 0° 42'

Hub section

V, velocity – ft/sec
R, radius – inches

5636-9

Figure 8. Velocity diagrams for 0.75 hub D_f stator.

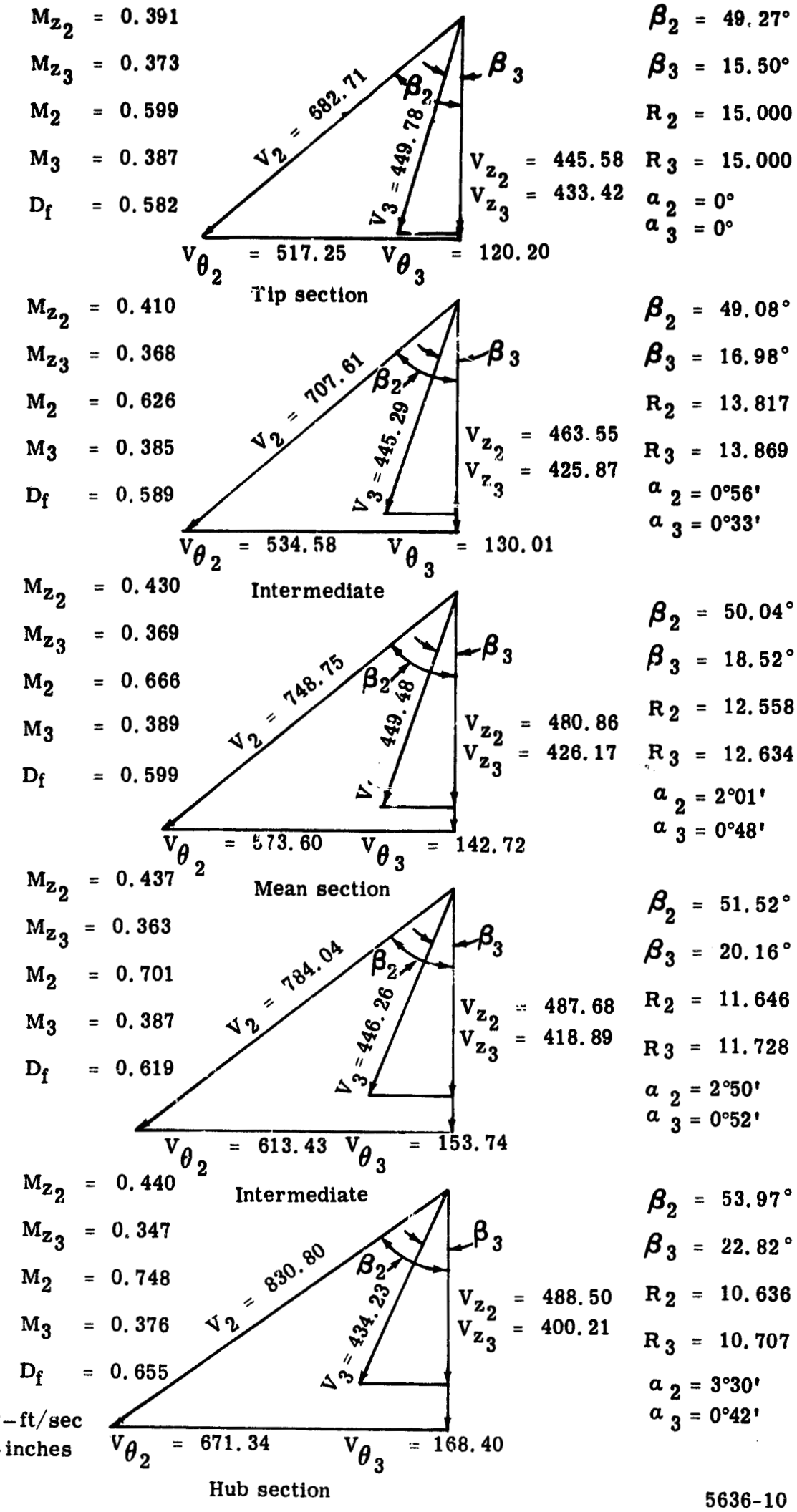

Figure 9. Velocity diagrams for 0.65 hub D_f stator.

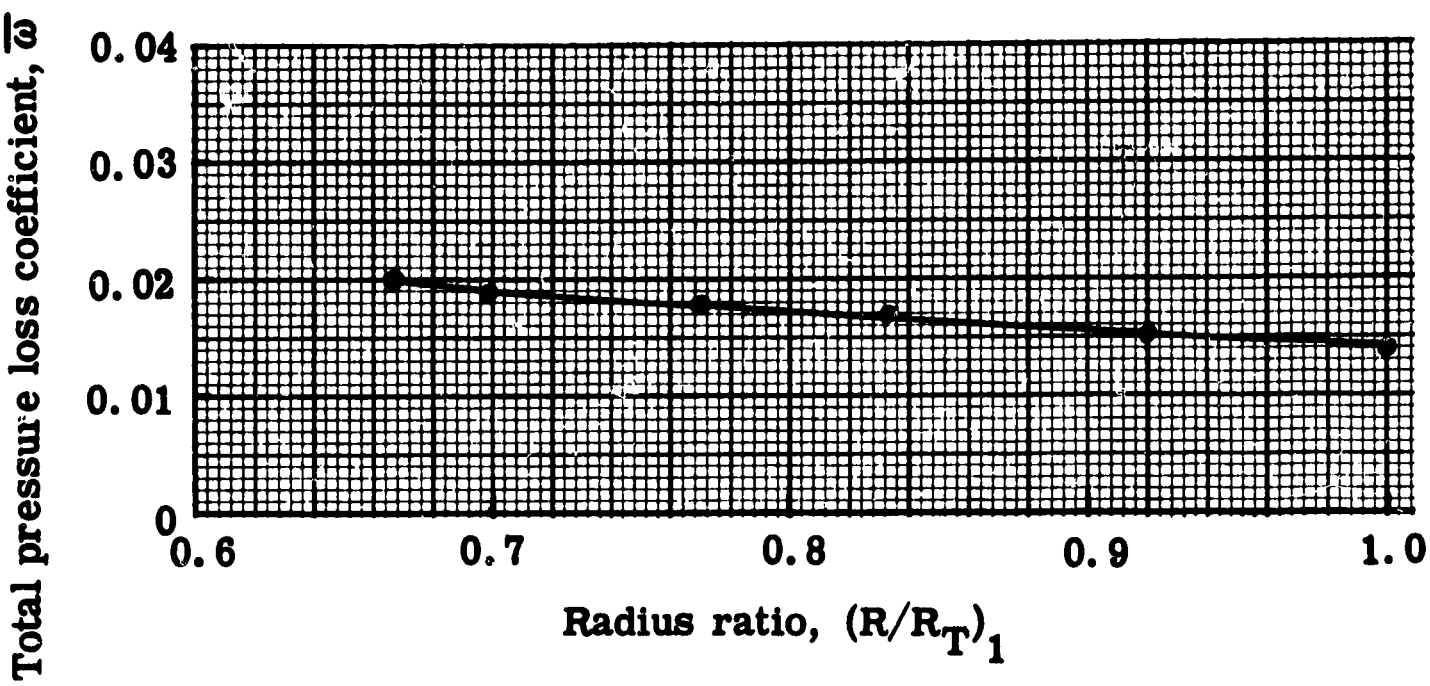

a. Design inlet guide vanes

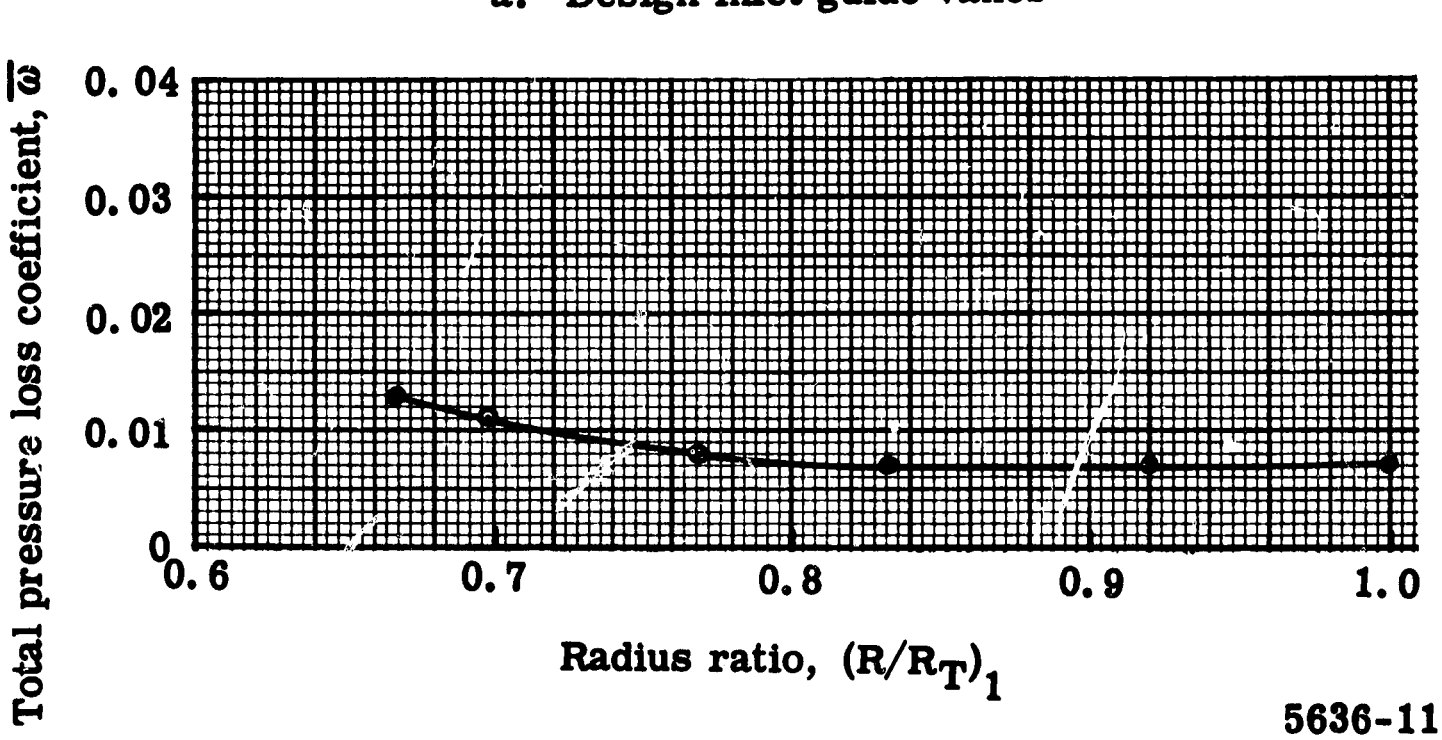

b. Off-design inlet guide vanes

Figure 10. Inlet guide vane total pressure loss coefficient distribution.

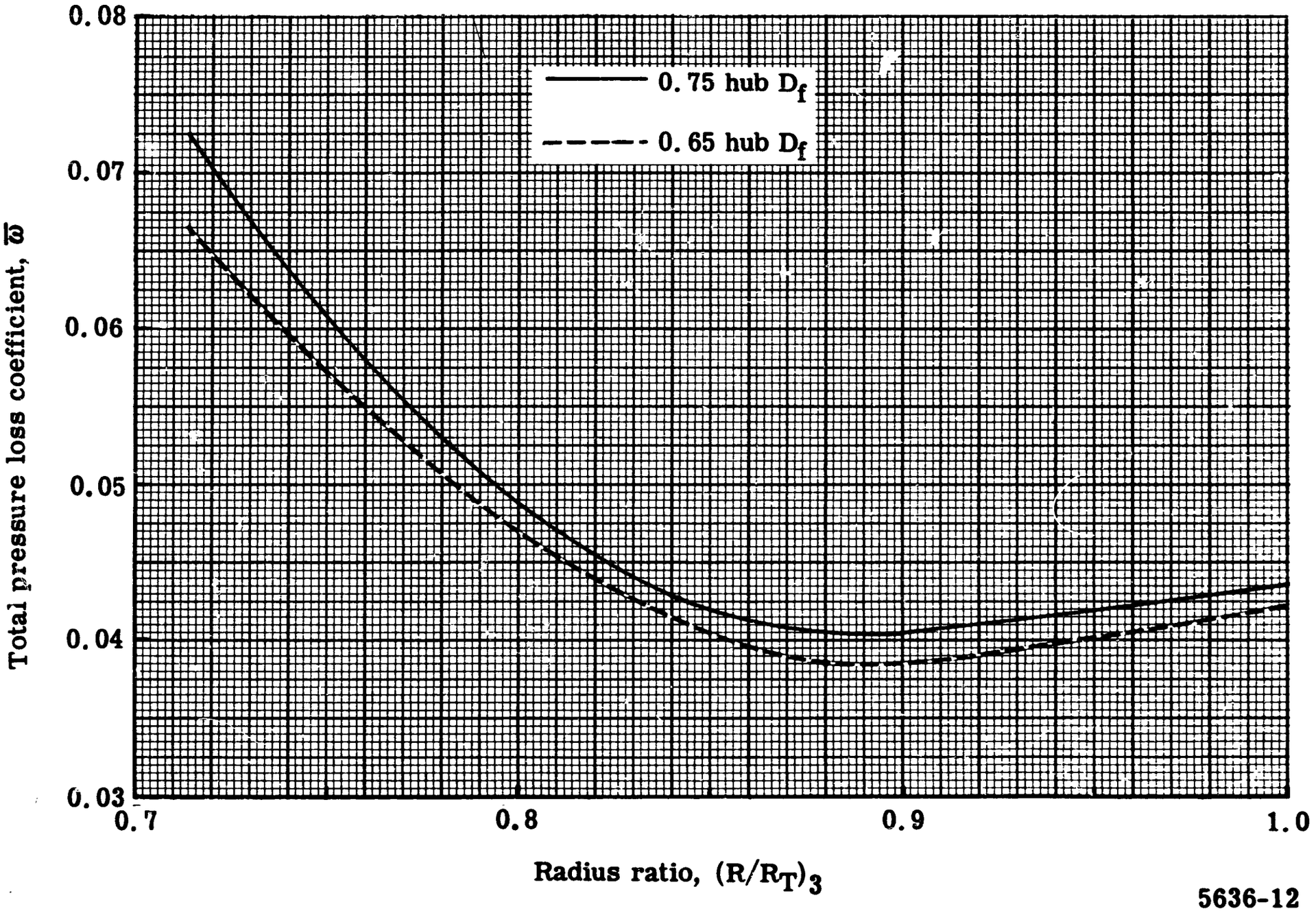

Figure 11. Stator design total pressure loss coefficient distribution.

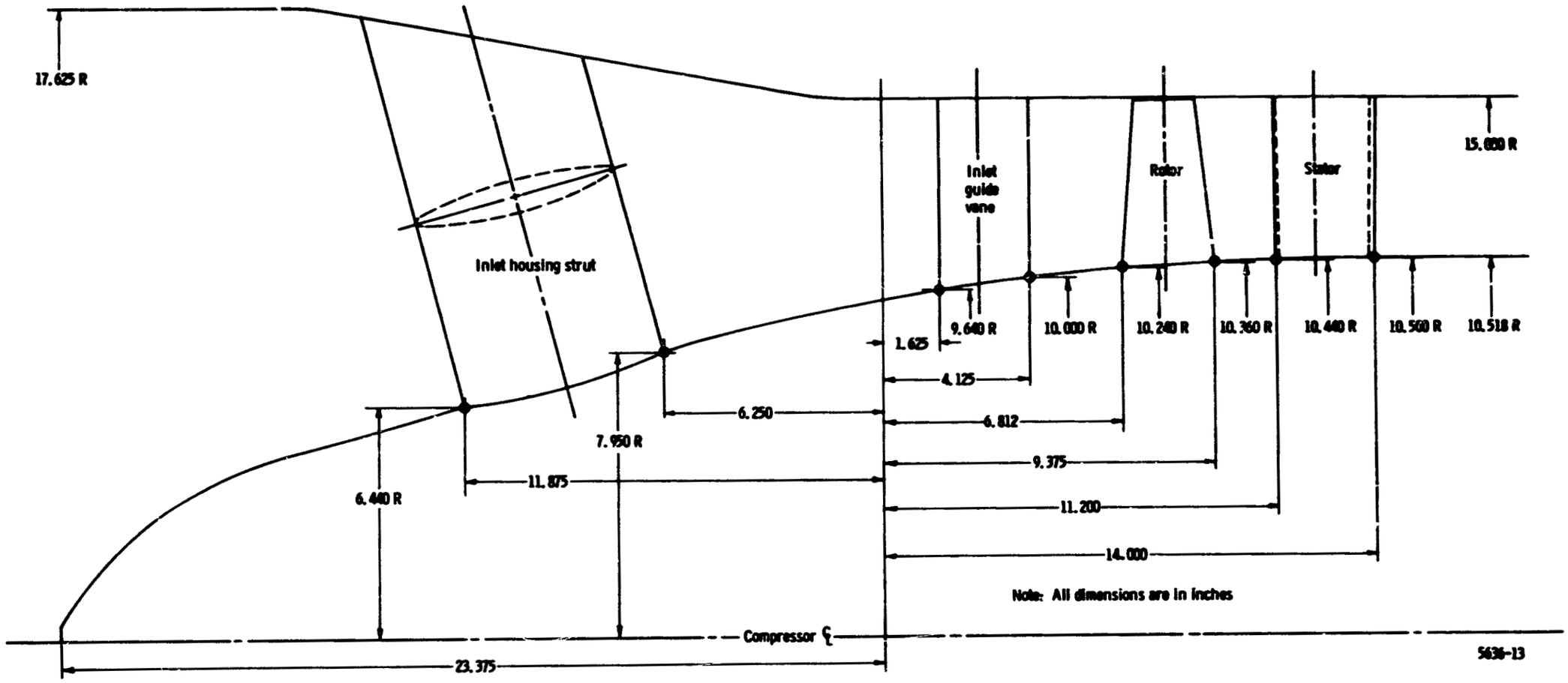

Figure 12. Test rig flow path.

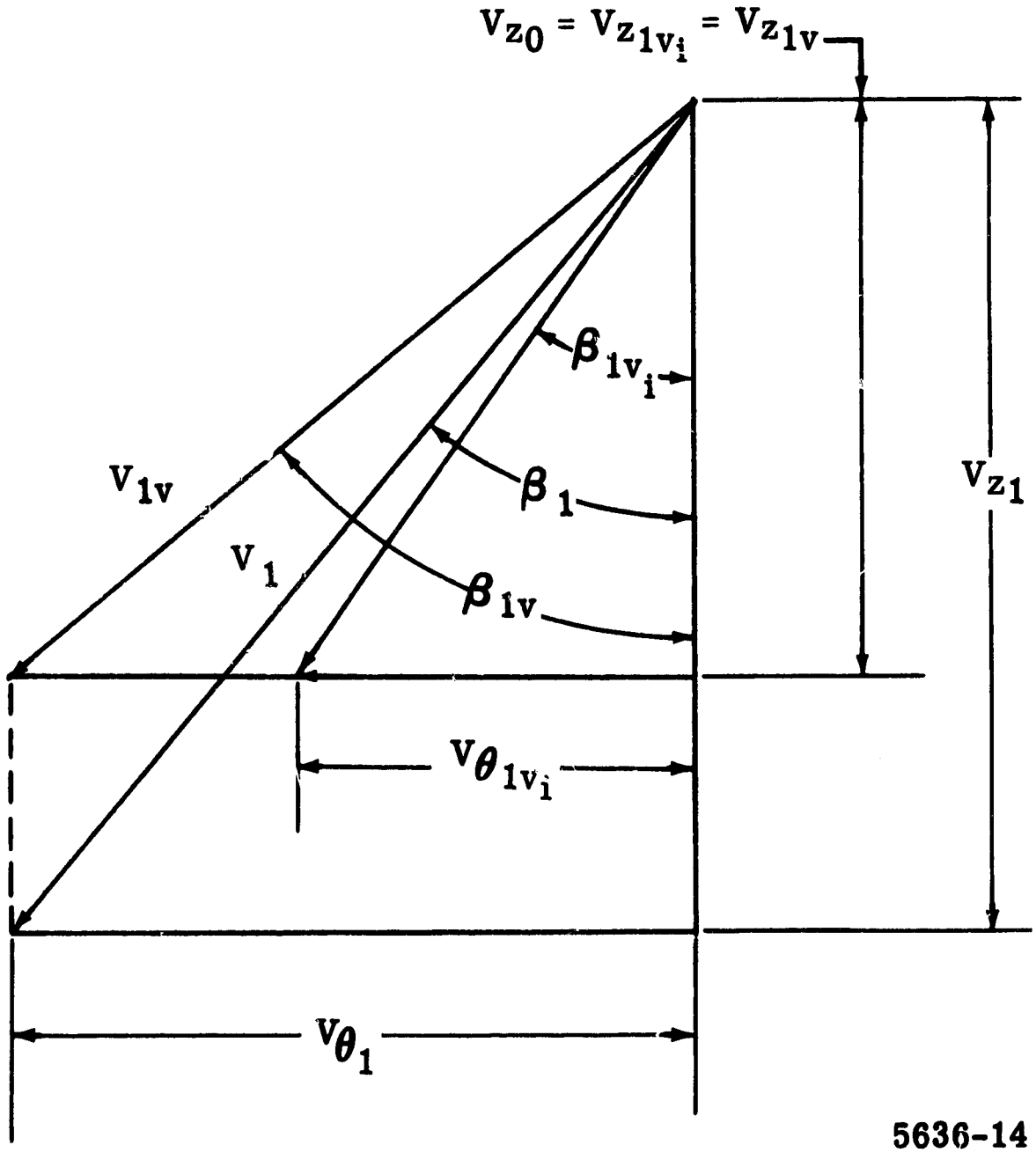

Figure 13. Velocity triangle compressible-incompressible relationship for compressibility effect.

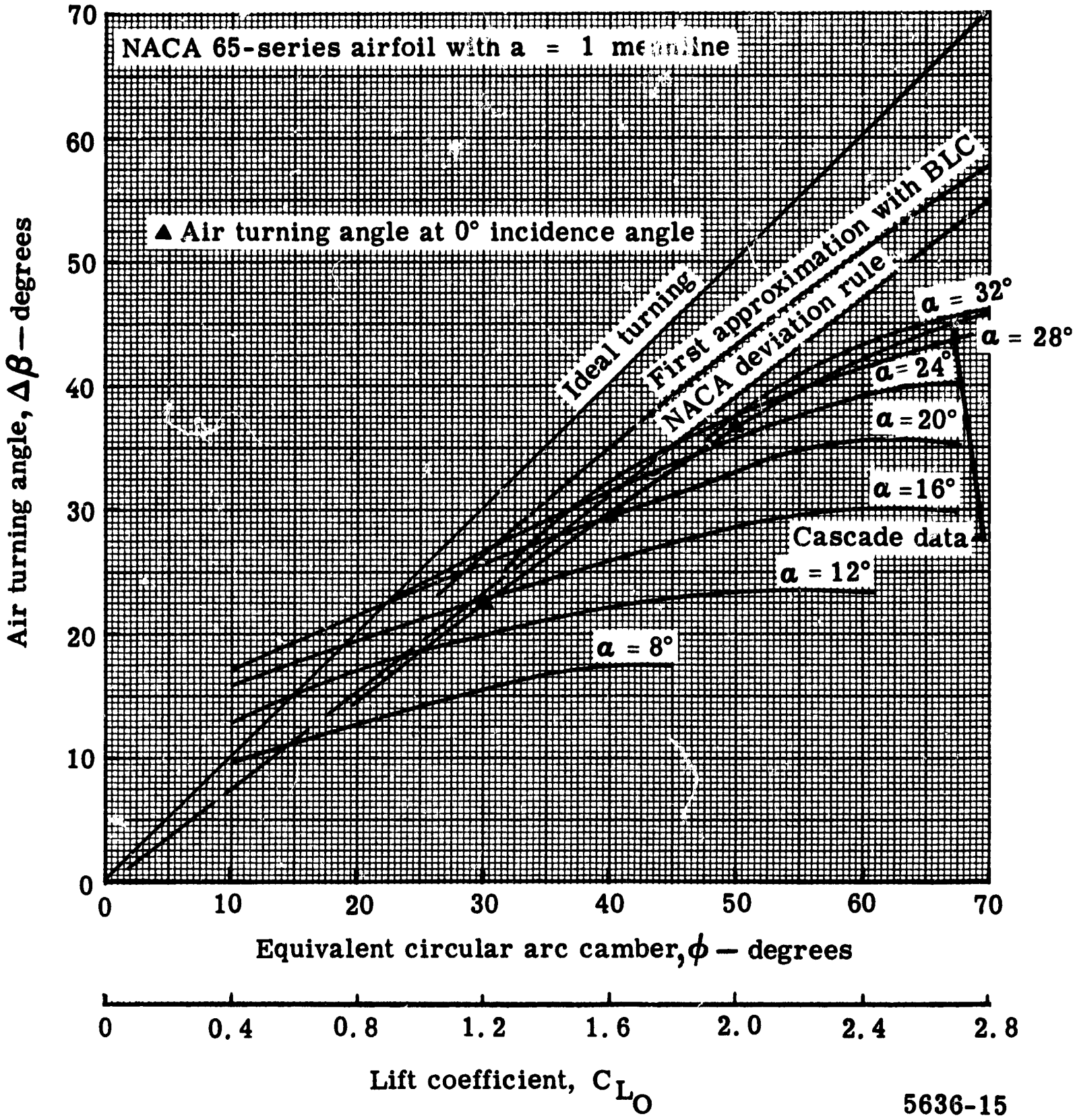

Figure 14. Air turning angle as a function of equivalent circular arc camber with $\beta_2 = 45°$ and $\sigma = 1.0$.

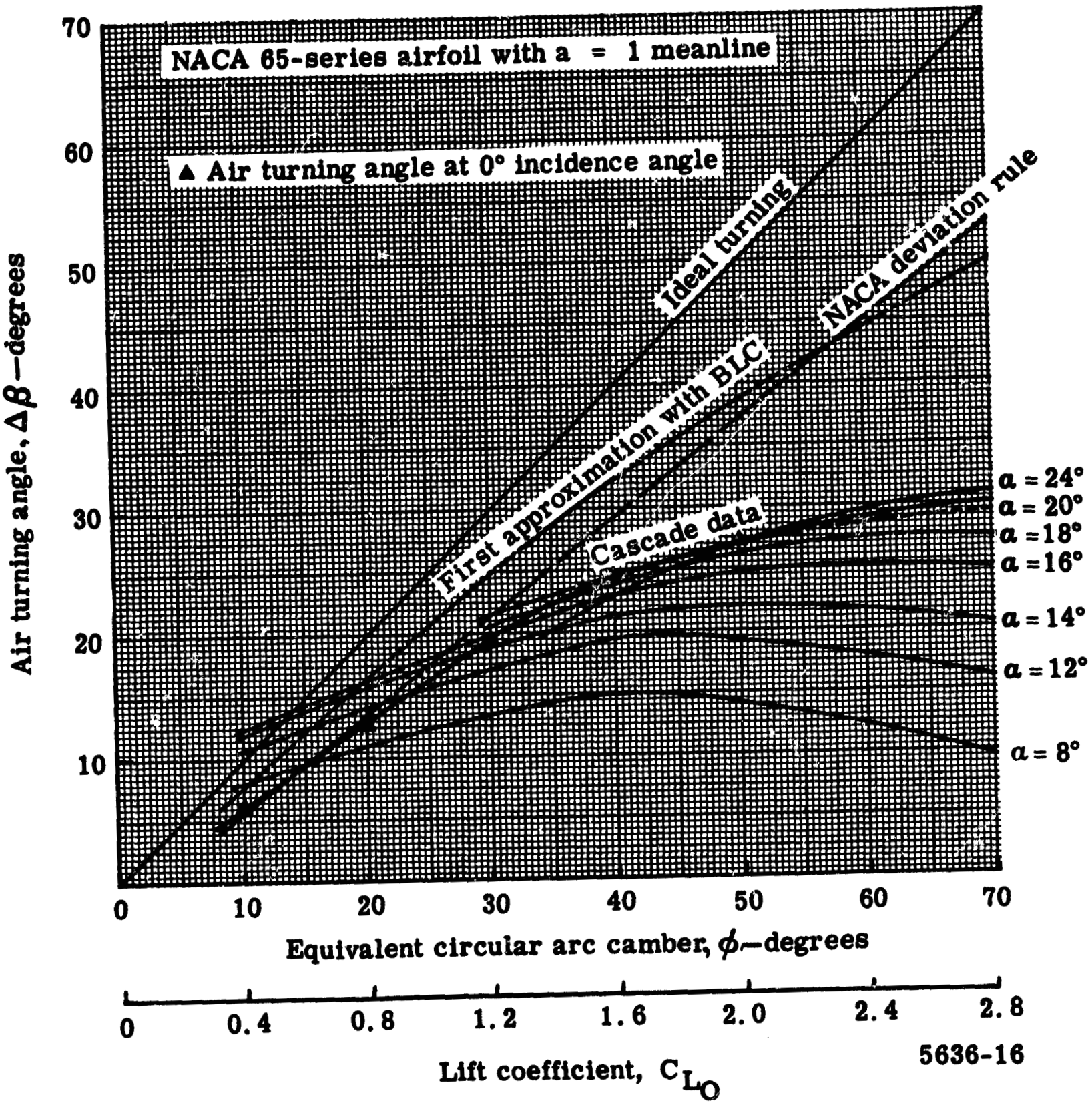

Figure 15. Air turning angle as a function of equivalent circular arc camber with $\beta_2 = 60°$ and $\sigma = 1.0$.

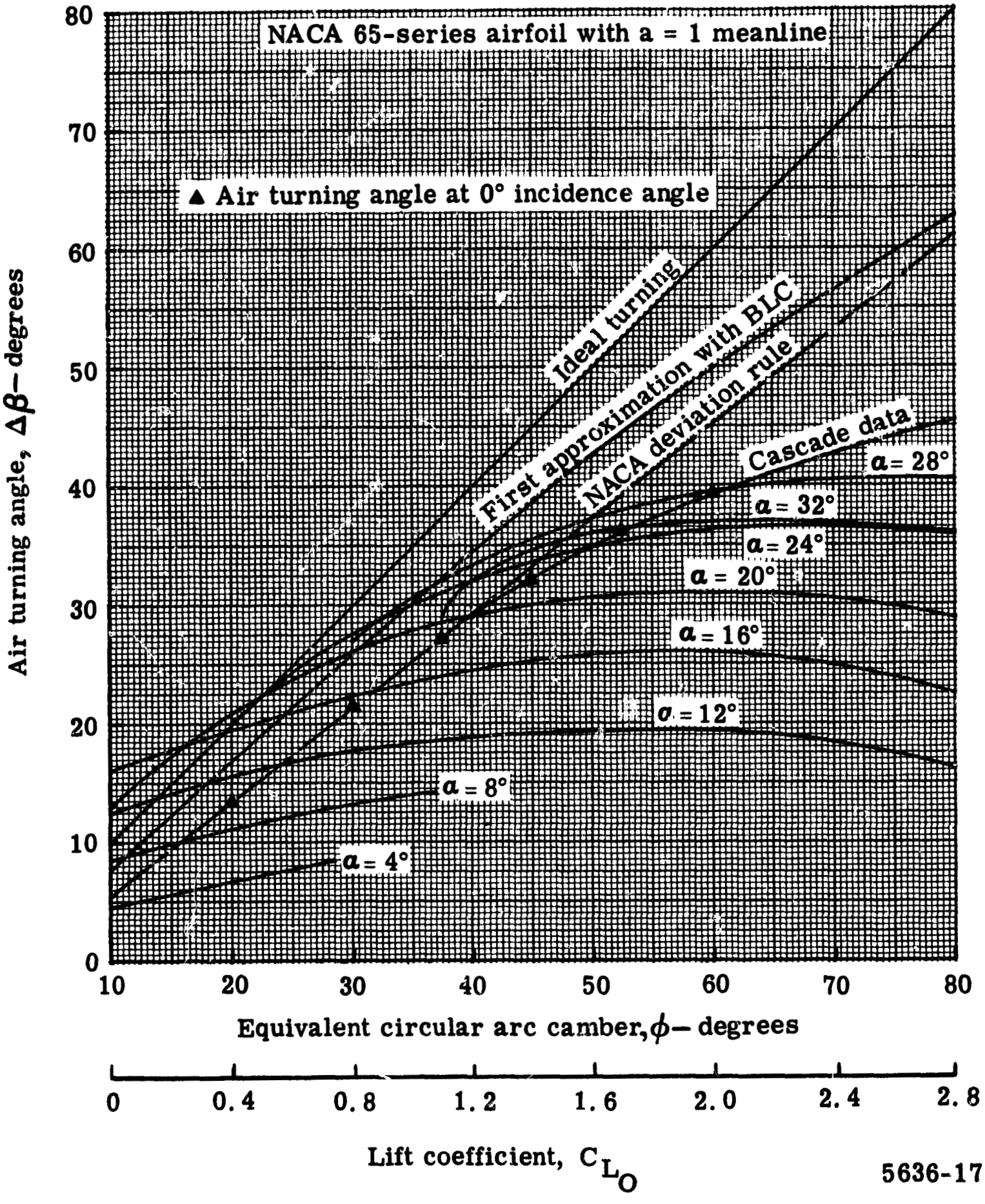

Figure 16. Air turning angle as a function of equivalent circular arc camber with $\beta_2 = 60°$ and $\sigma = 1.5$.

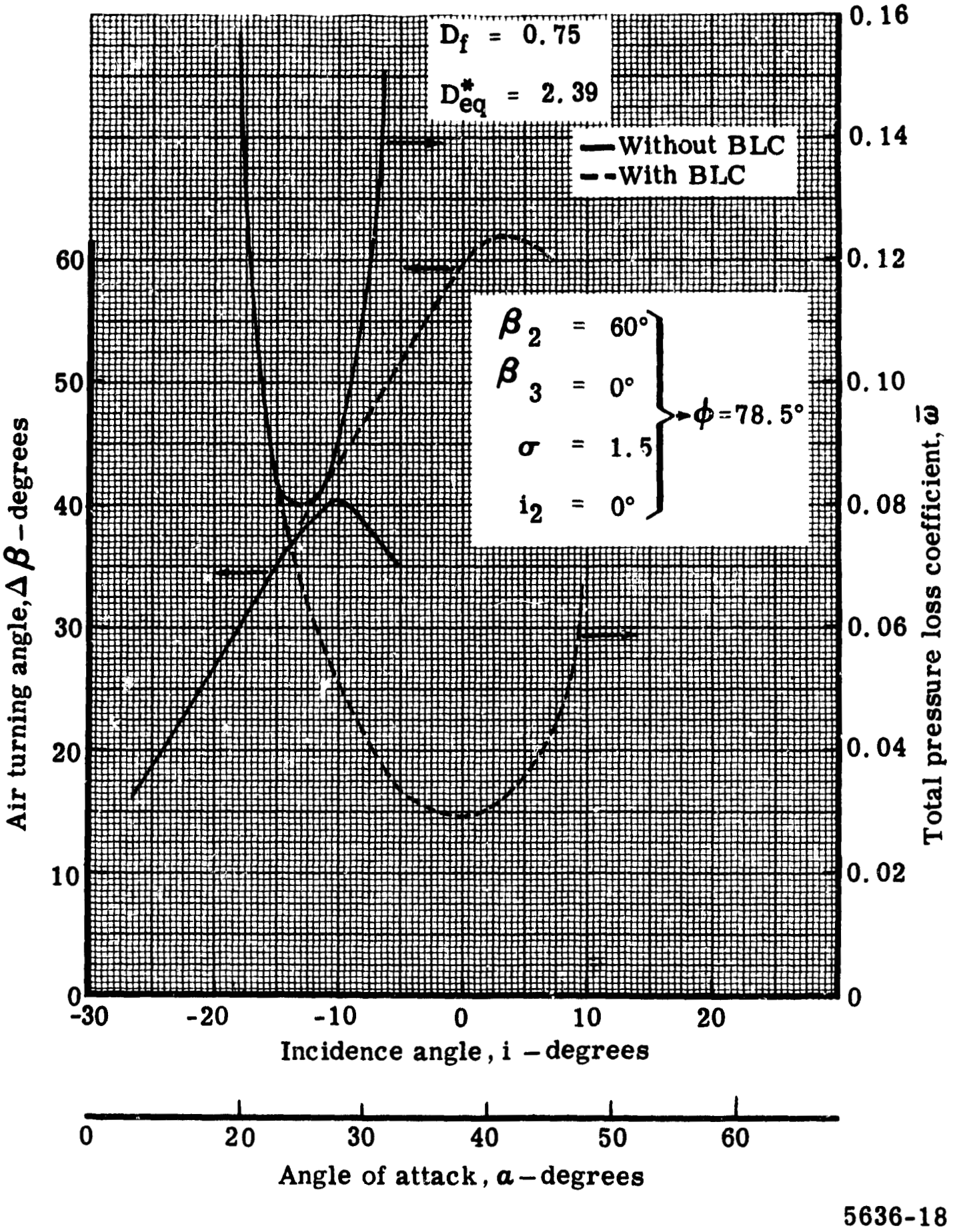

Figure 17. Estimated 0.75 hub D_f stator performance with and without boundary layer control.

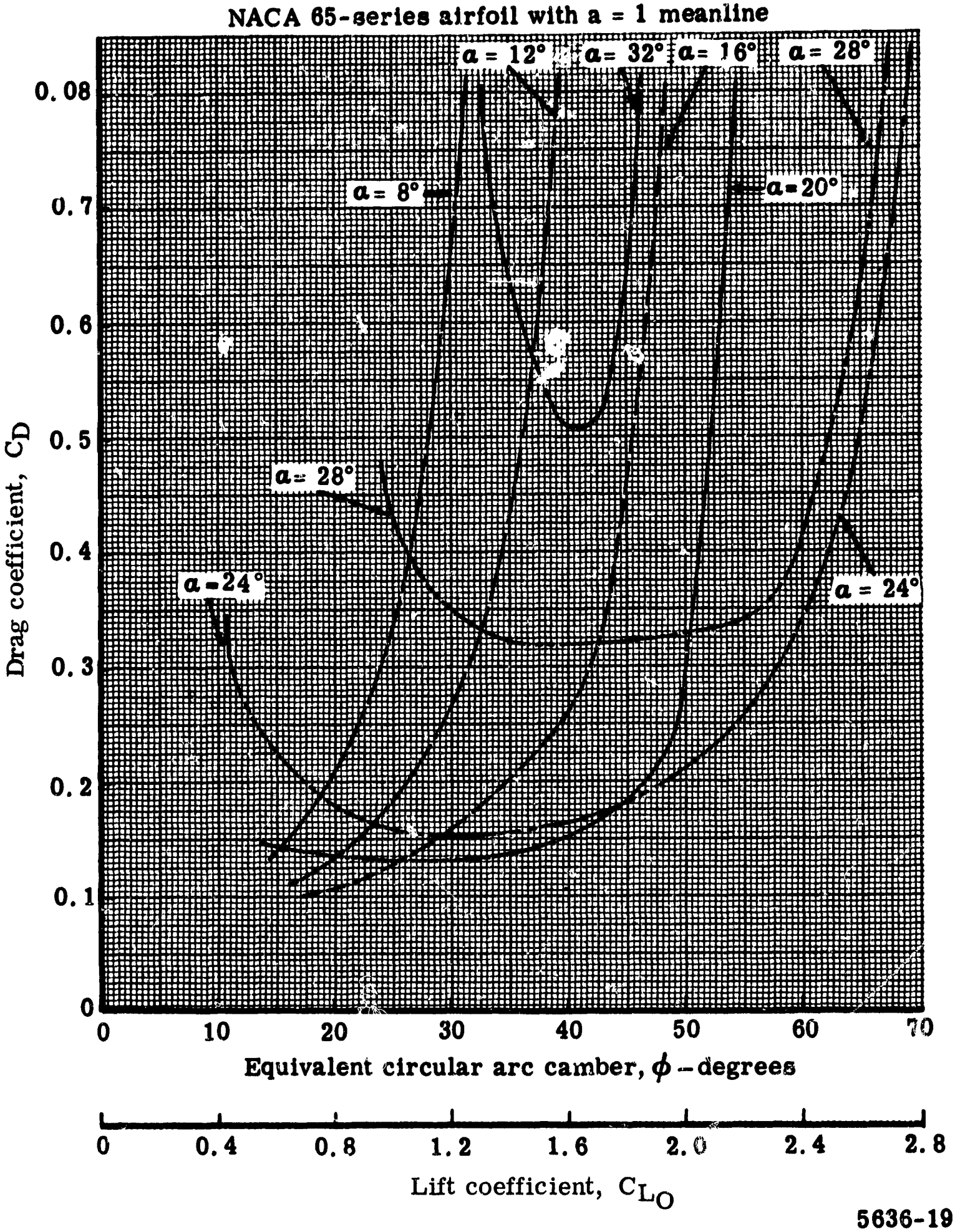

Figure 18. Drag coefficient as a function of equivalent circular arc camber for $\beta_2 = 60°$ and $\sigma = 1.5$.

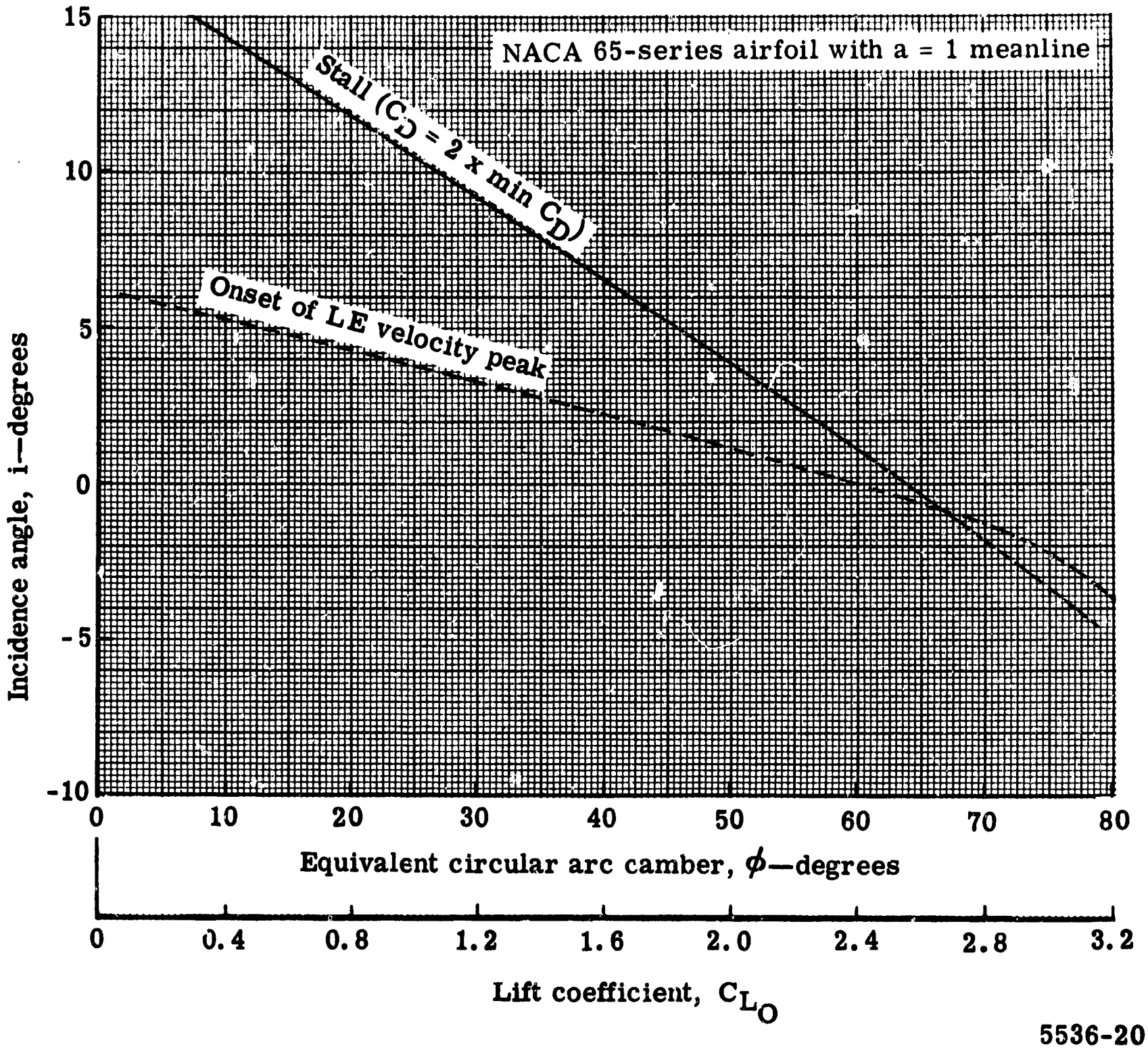

Figure 19. Stalling incidence and onset of leading edge velocity peak for β_2 = 45° and σ = 1.0.

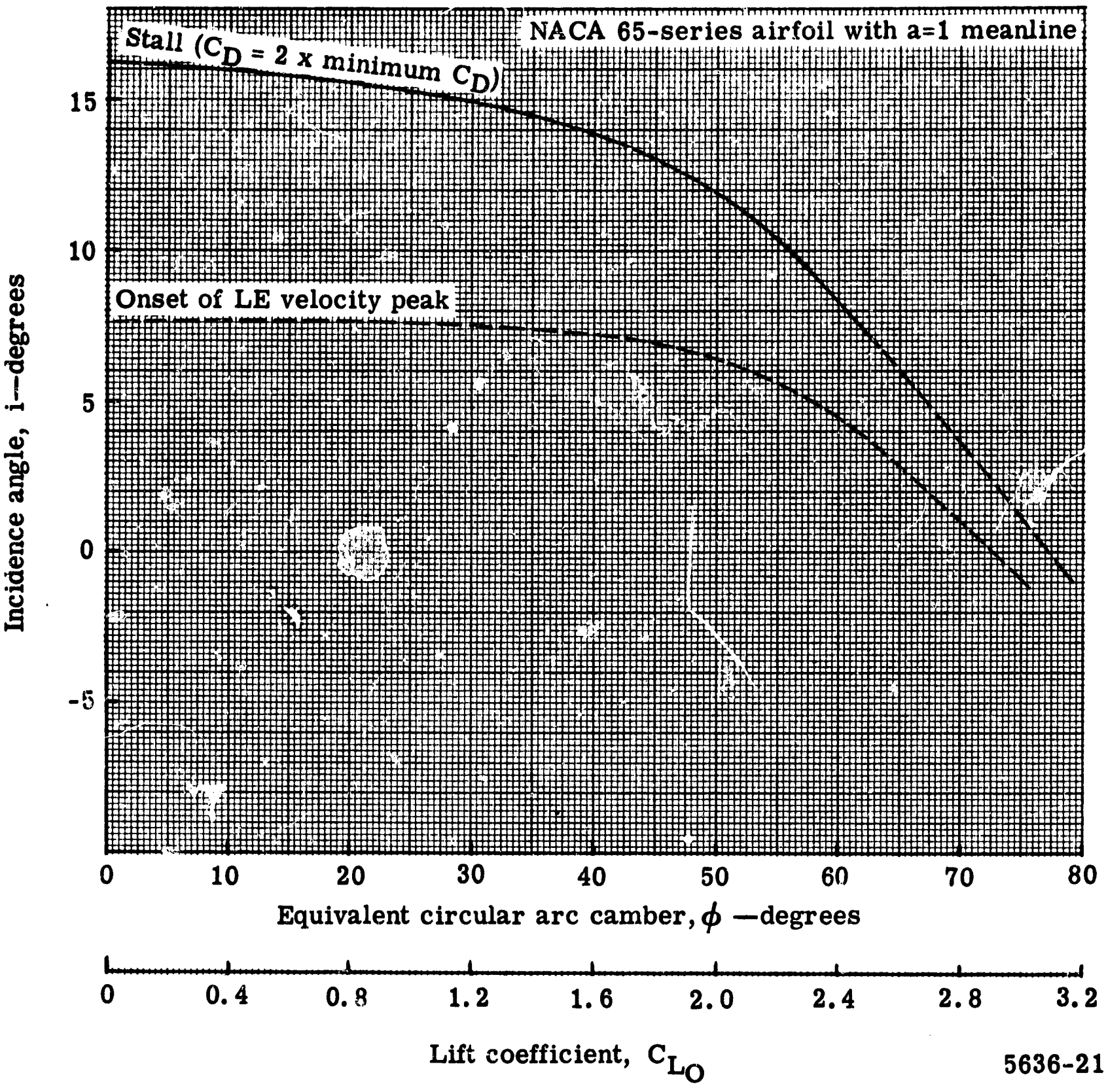

Figure 20. Stalling incidence and onset of leading edge velocity peak for β_2 = 45° and σ = 1.5.

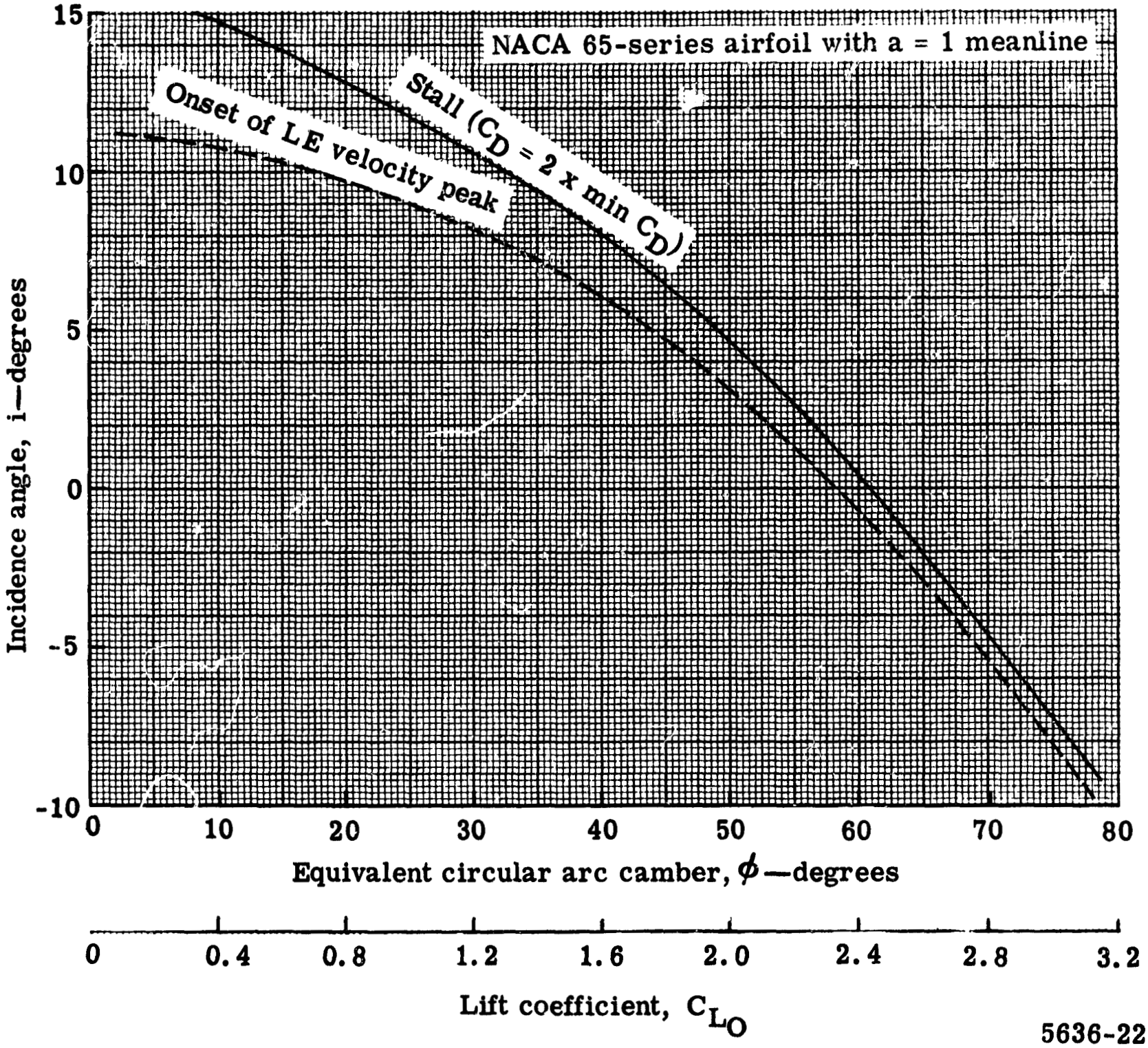

Figure 21. Stalling incidence and onset of leading edge velocity peak for $\beta_1 = 60°$ and $\sigma = 1.5$.

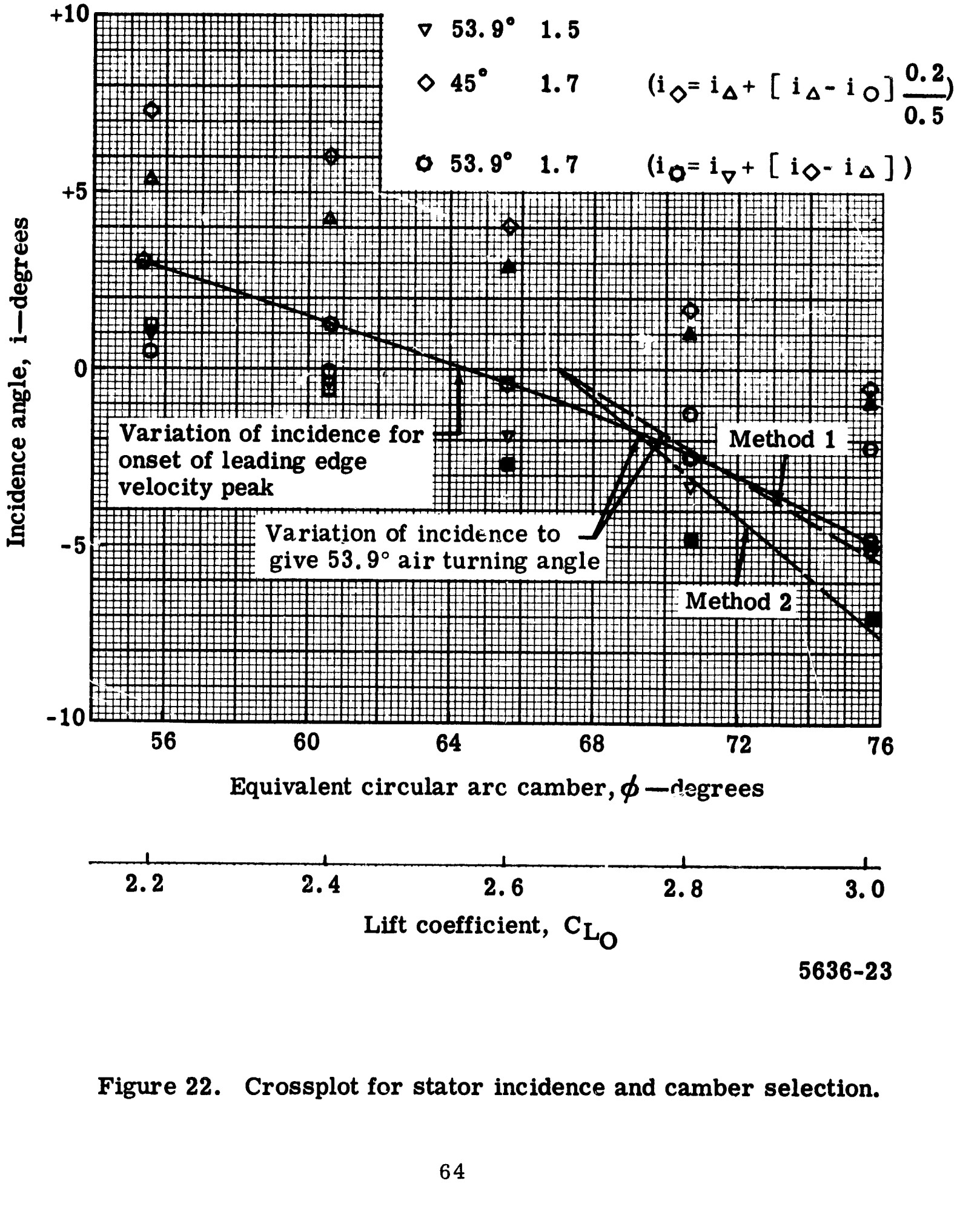

Figure 22. Crossplot for stator incidence and camber selection.

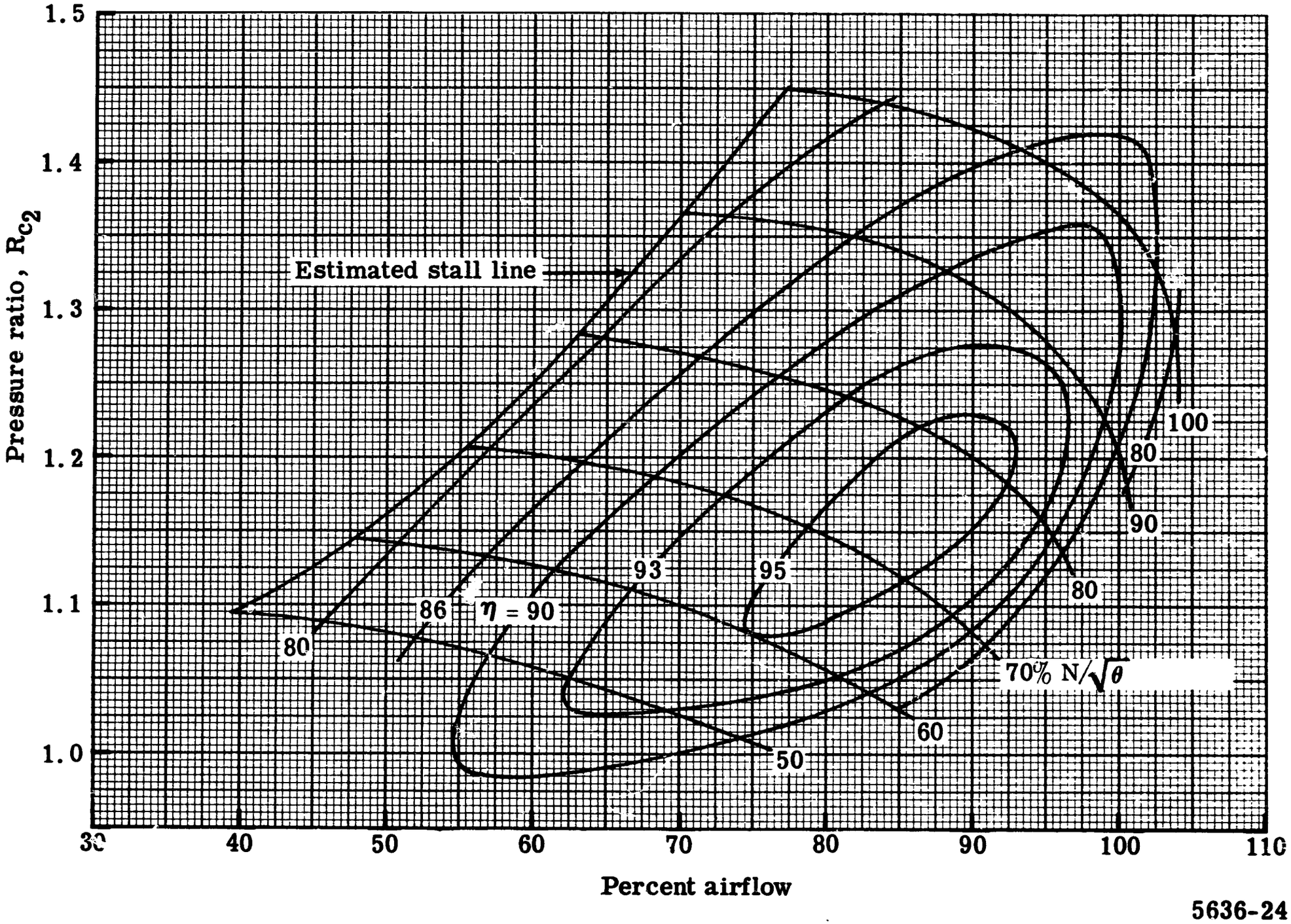

Figure 23. Estimated flow generation rotor performance with design inlet guide vanes.

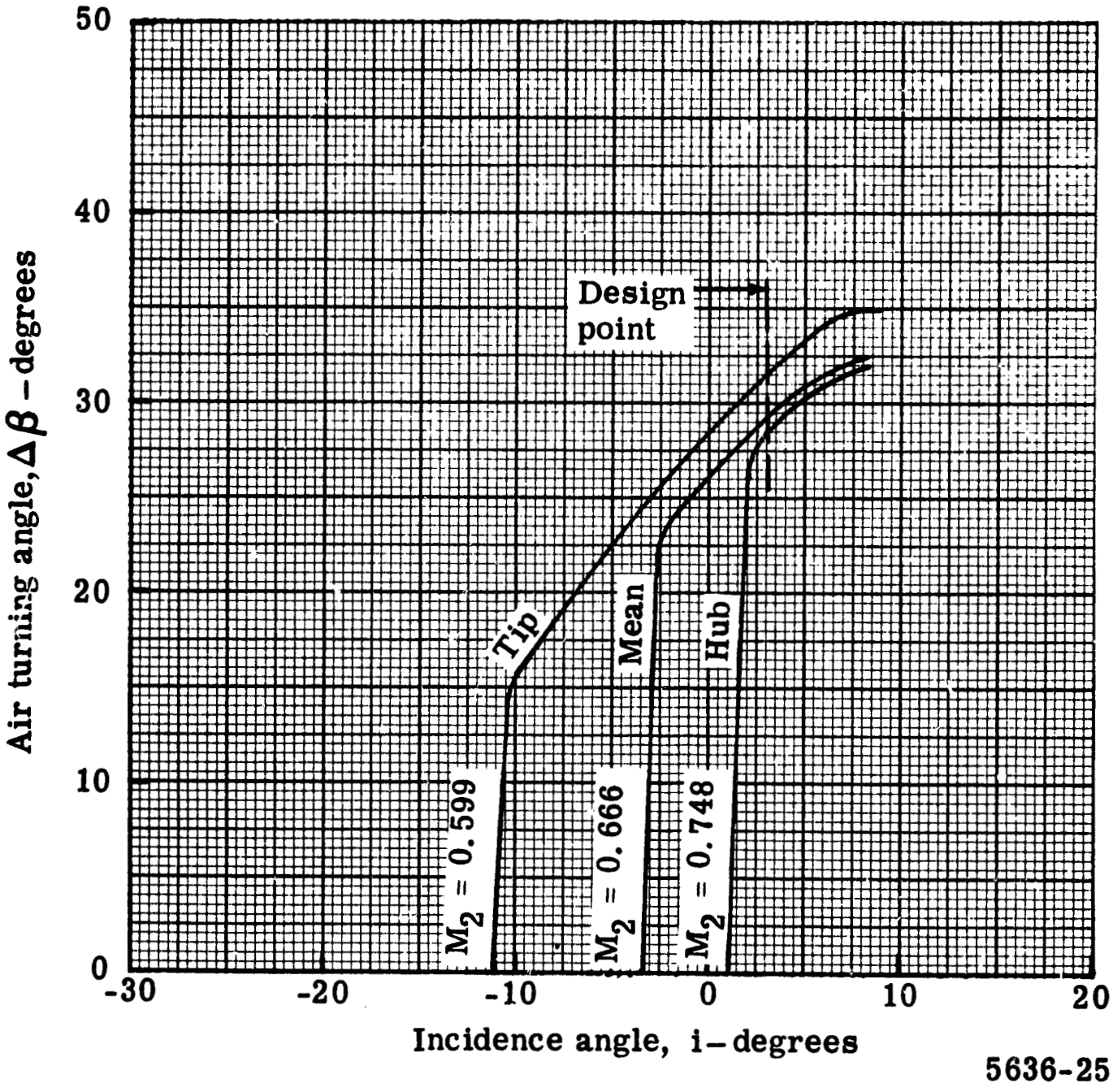

Figure 24. Operating range of 0.65 hub D_f stator at design inlet Mach numbers.

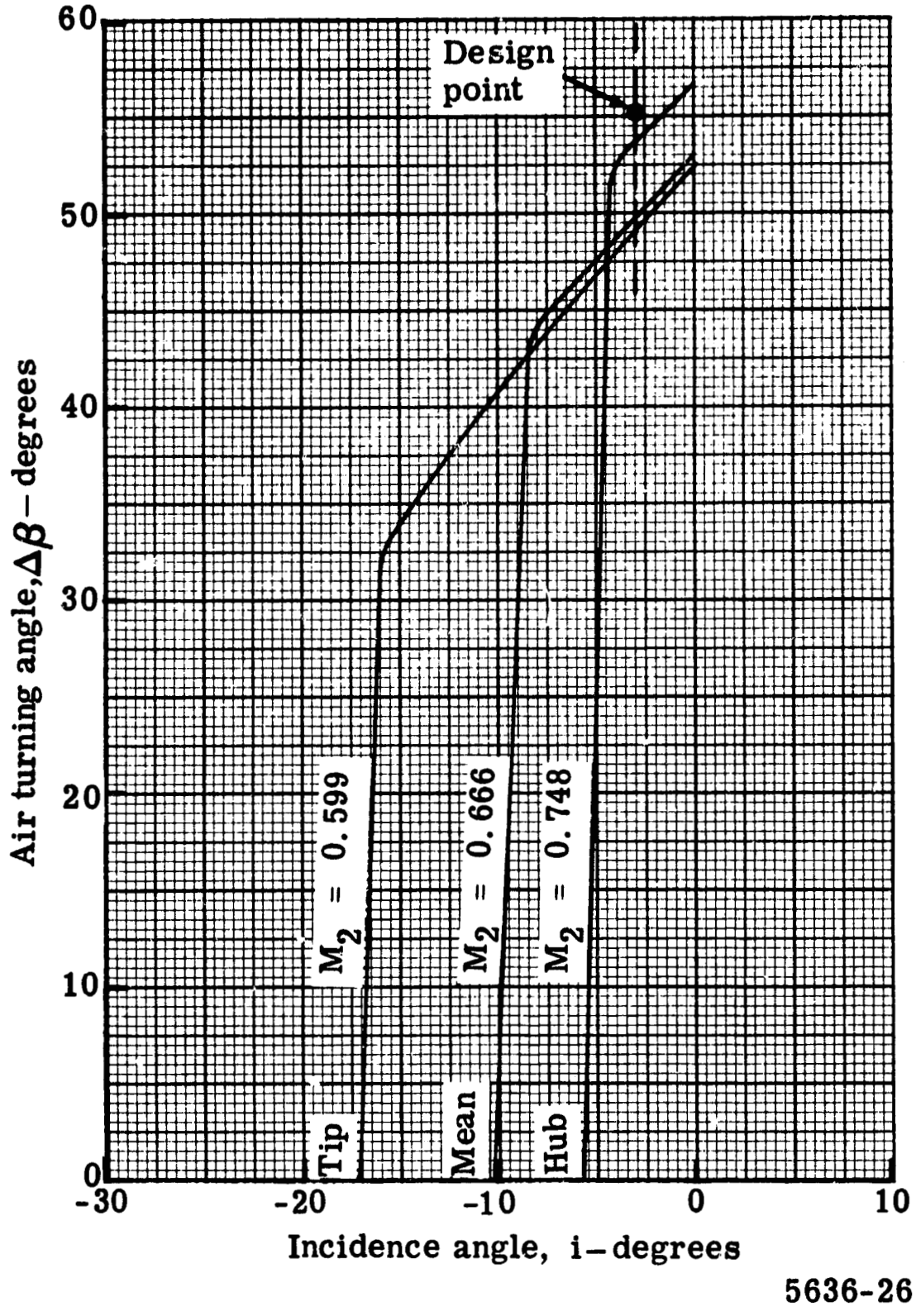

Figure 25. 0.75 hub D_f stator operating range at design inlet Mach numbers.

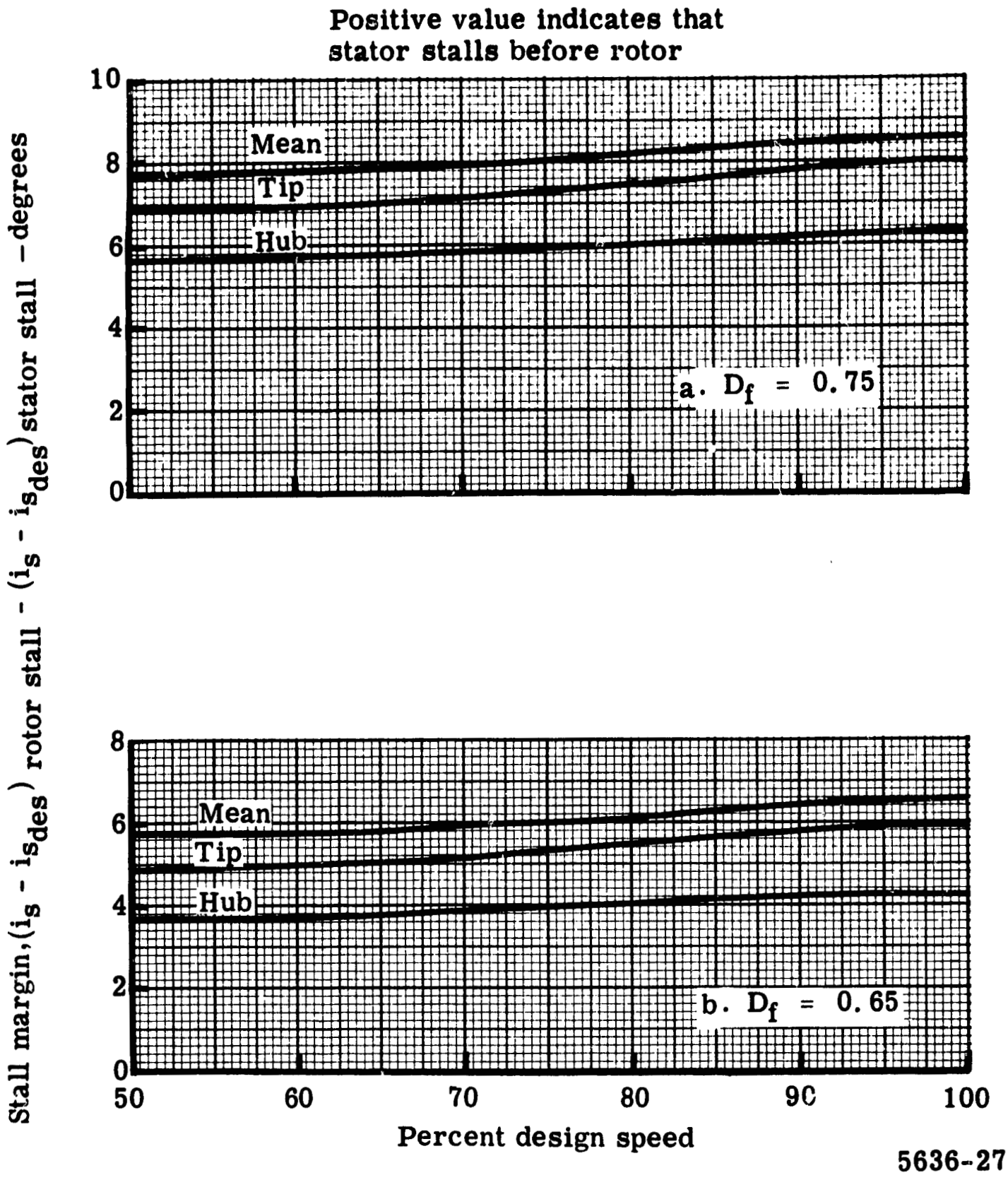

Figure 26. Margin between stator design inlet angle and stator inlet angle at rotor stall—design inlet guide vanes.

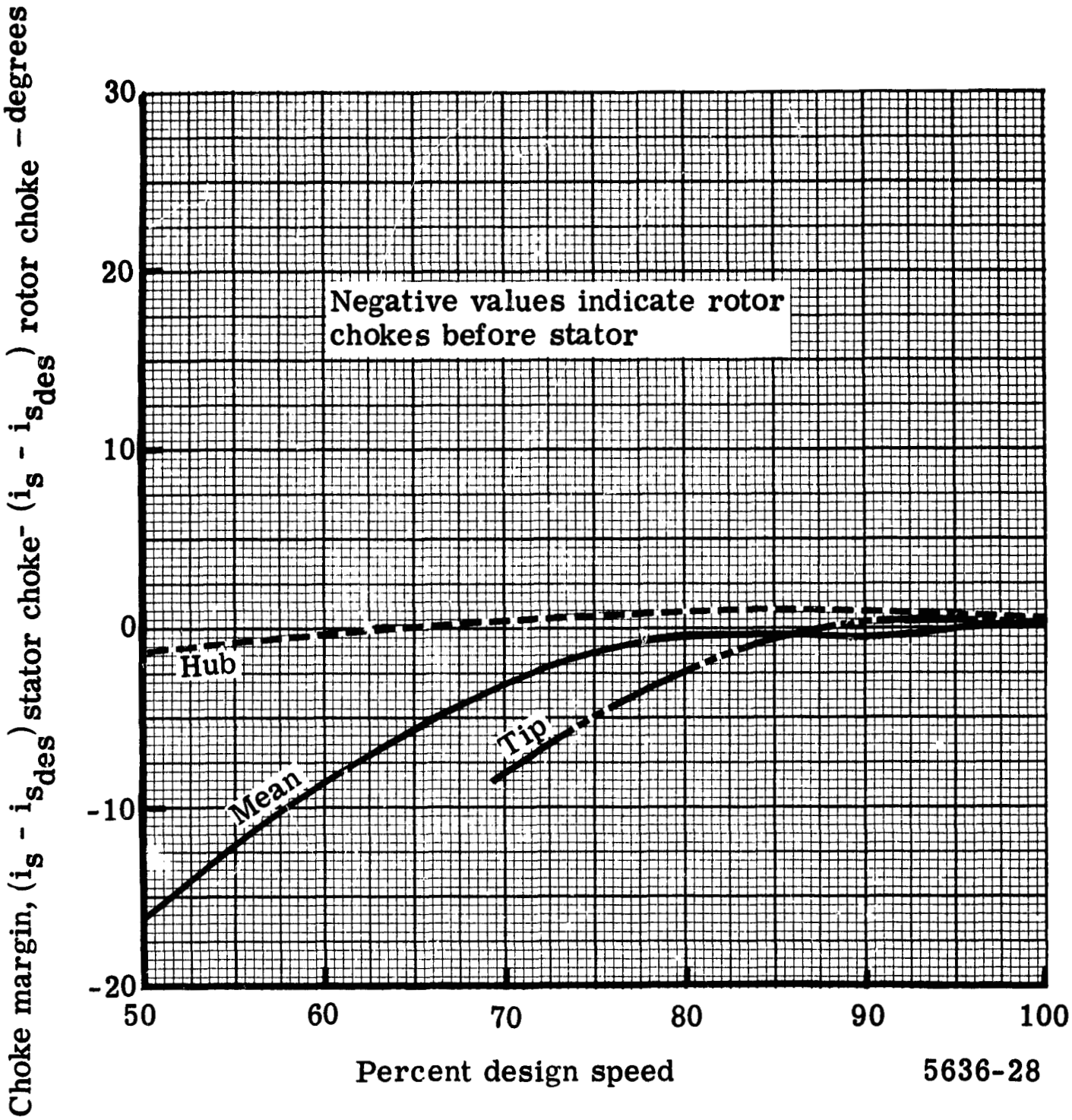

Figure 27. Margin between stator design inlet angle and stator inlet angle at rotor choke point – design inlet guide vanes.

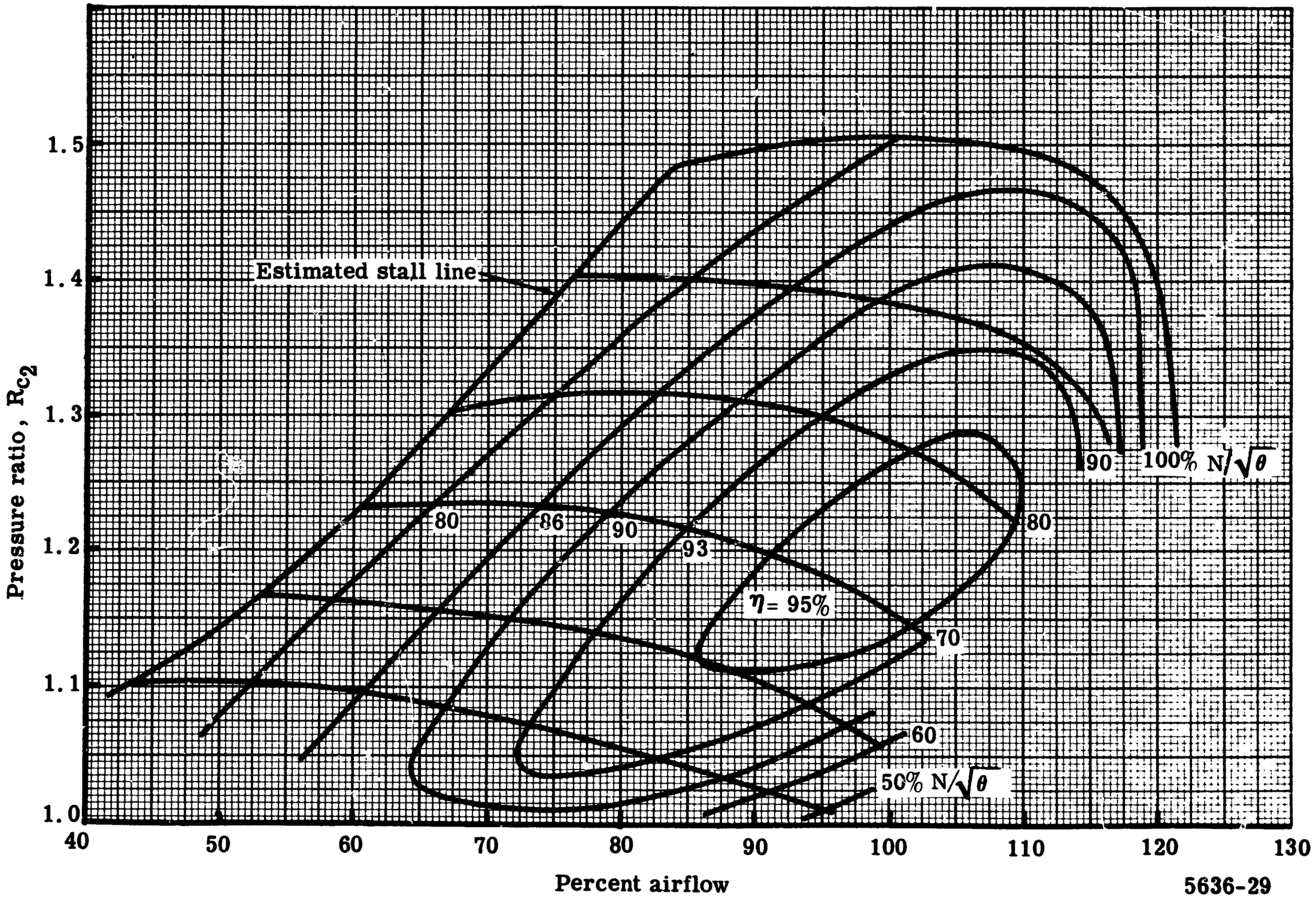

Figure 28. Estimated flow generation rotor performance with off-design inlet guide vanes.

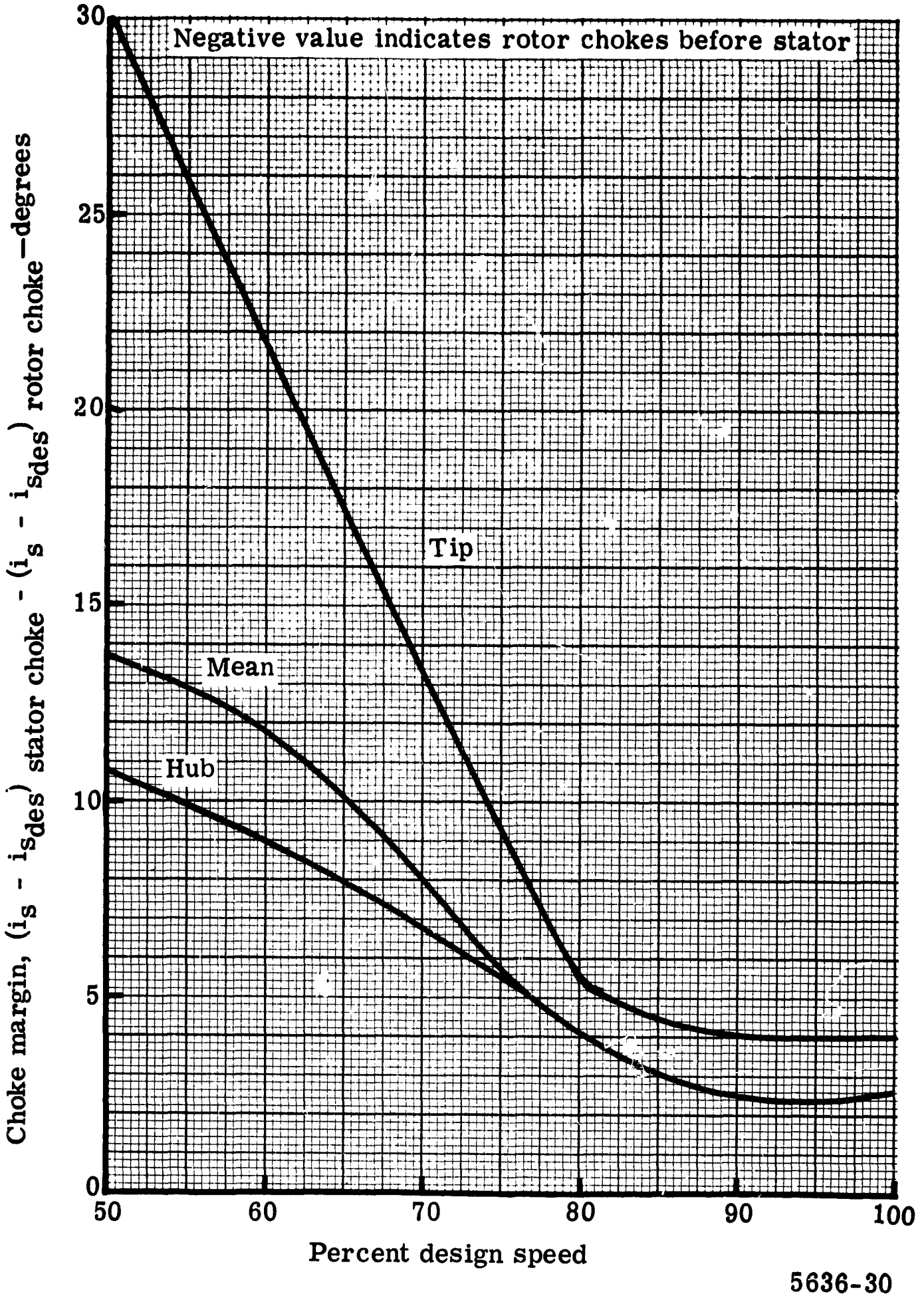

Figure 29. Margin between stator design inlet angle and stator inlet angle at rotor choke point--off-design inlet guide vanes.

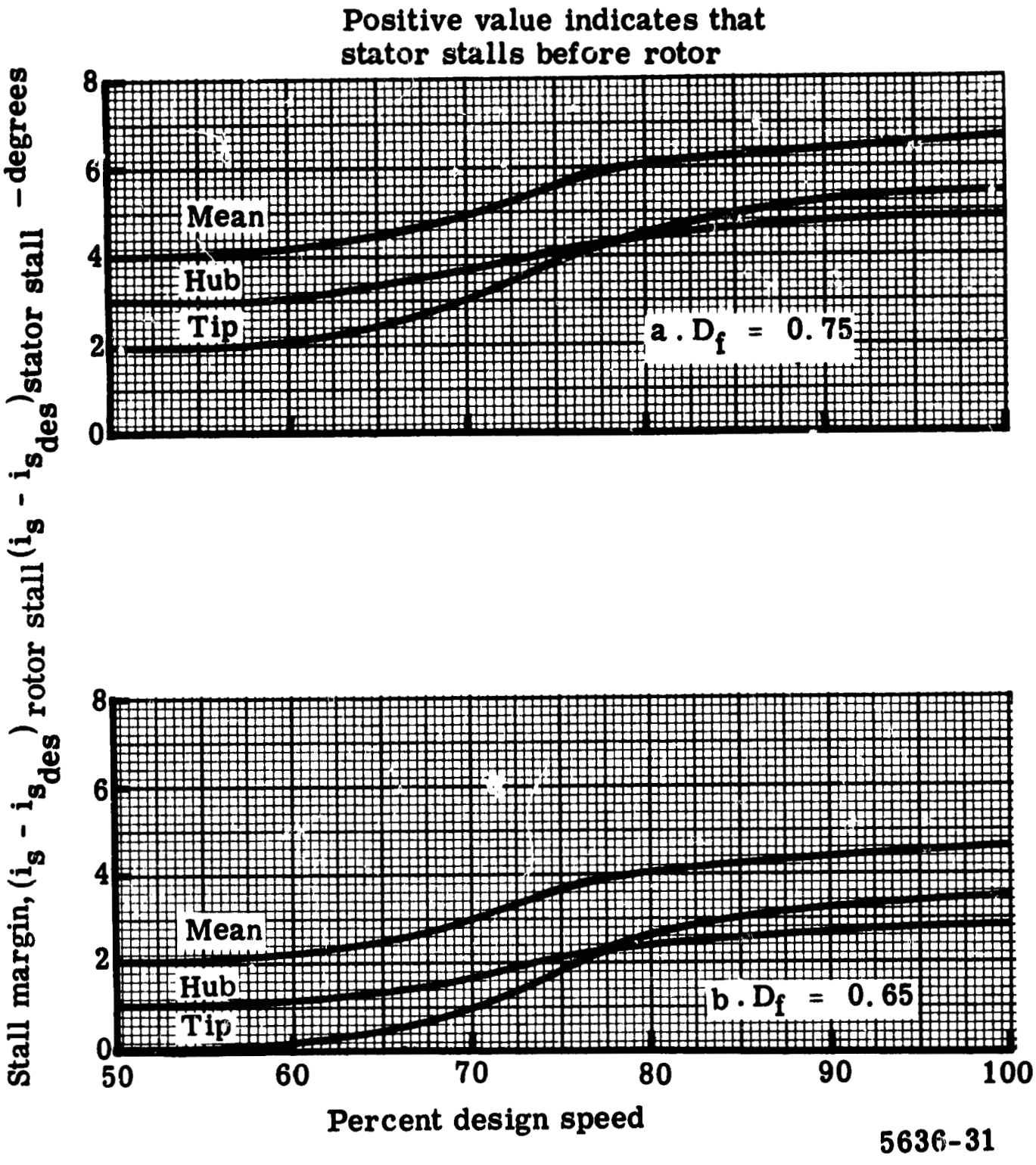

Figure 30. Margin between stator design inlet angle and stator inlet angle at rotor stall—off-design inlet guide vanes.

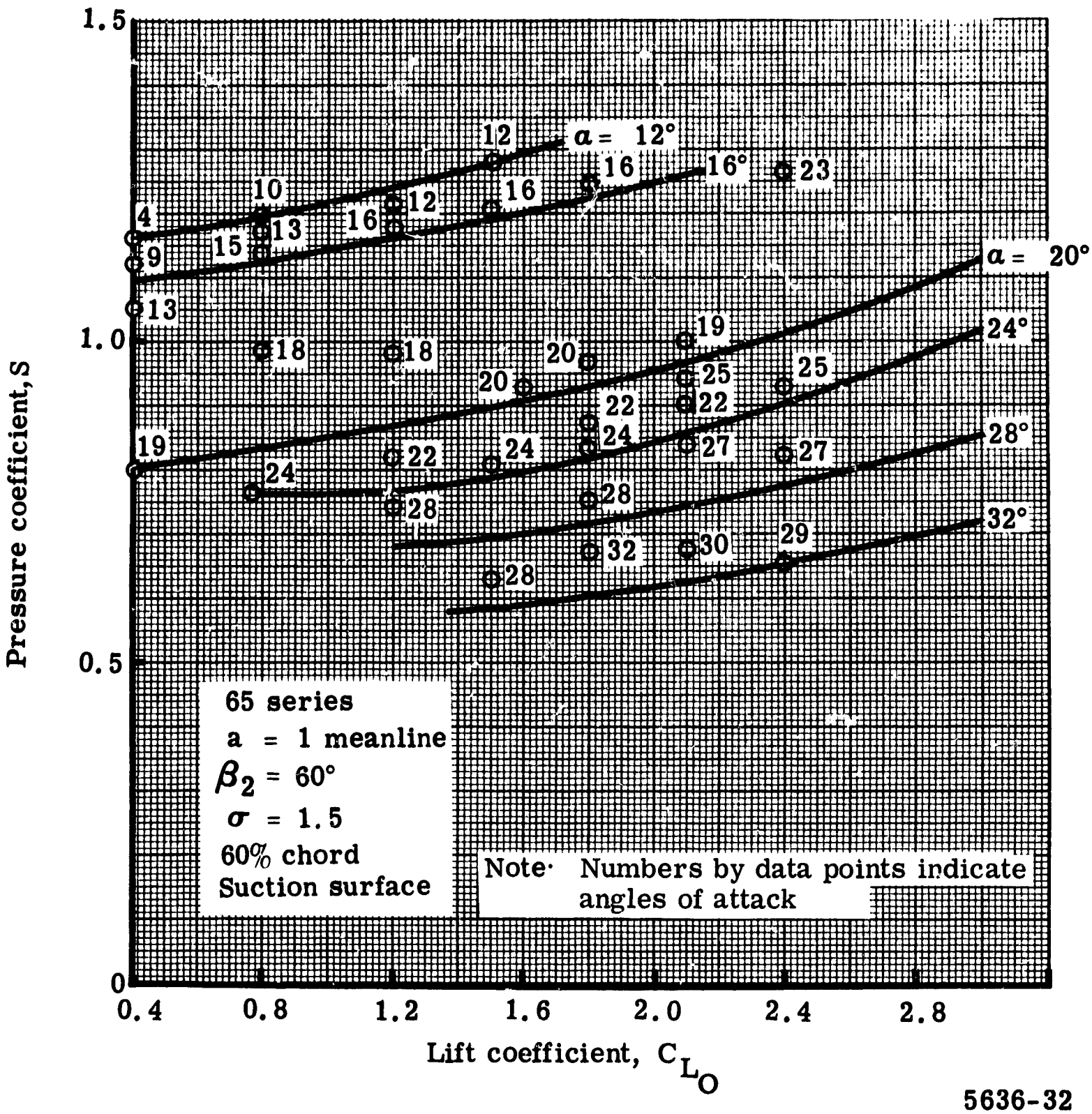

Figure 31. Typical cascade airfoil pressure coefficient variation.

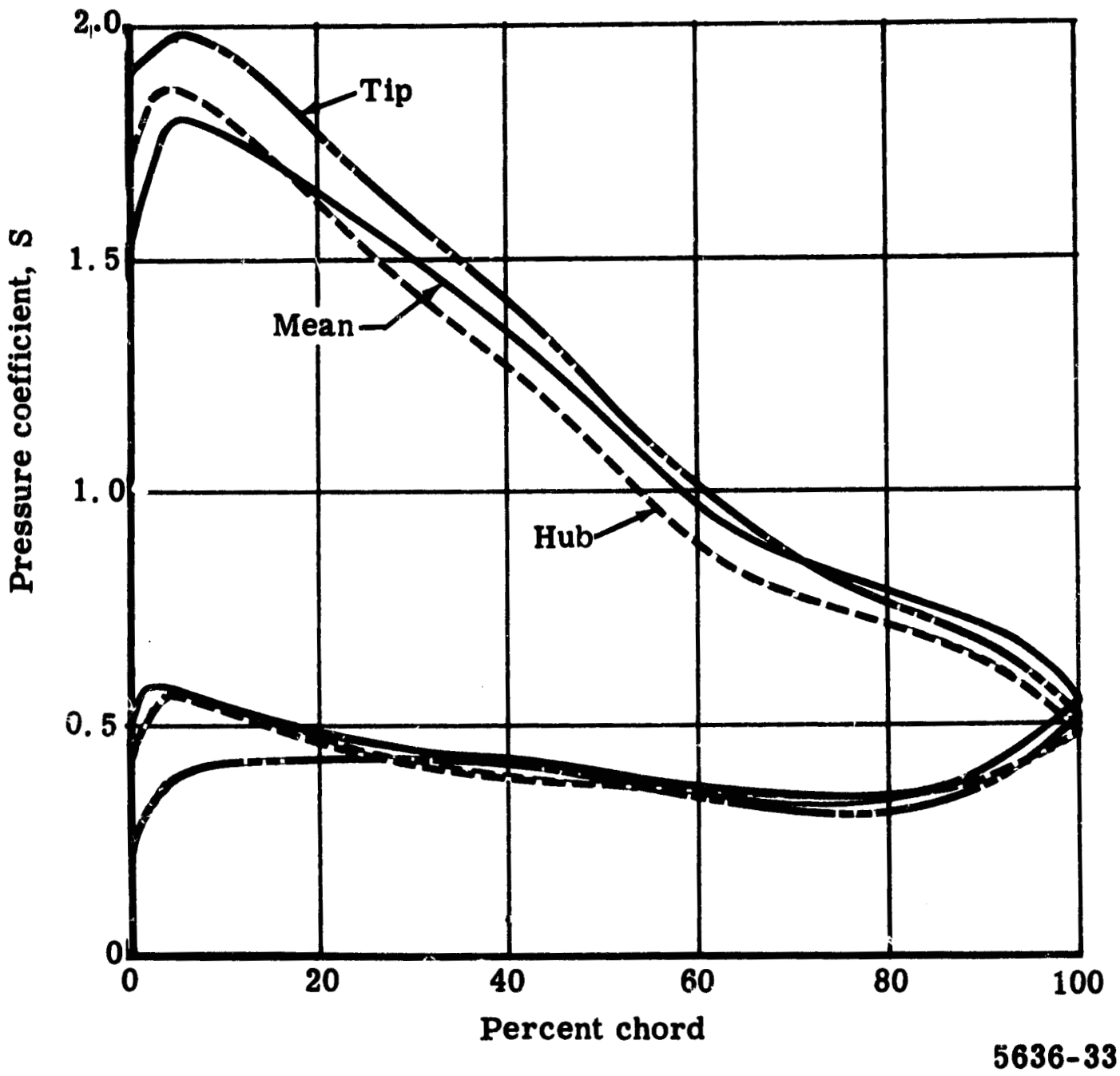

Figure 32. 0.75 hub D_f stator pressure distribution.

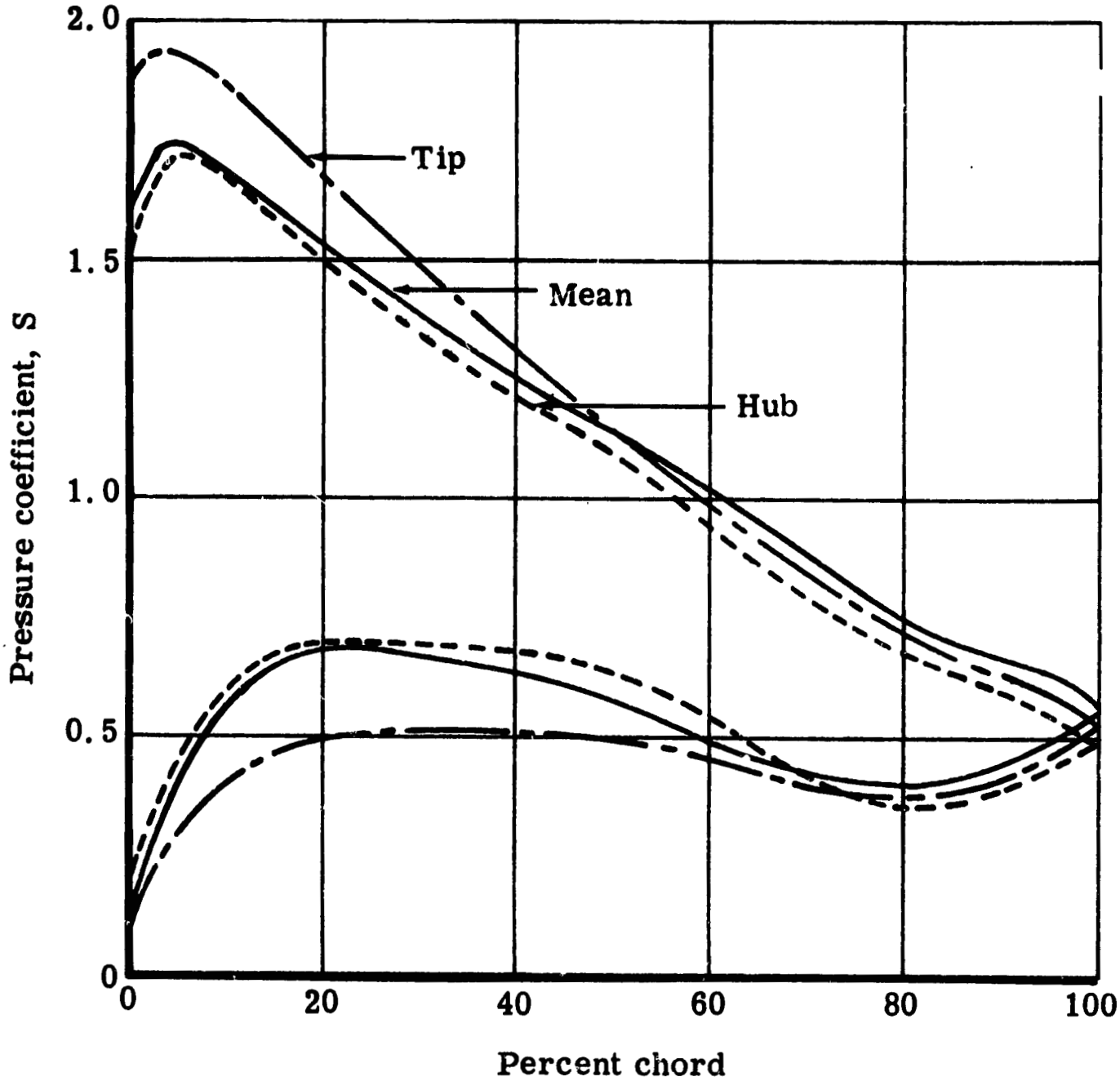

Figure 33. 0.65 hub D_f stator pressure distribution.

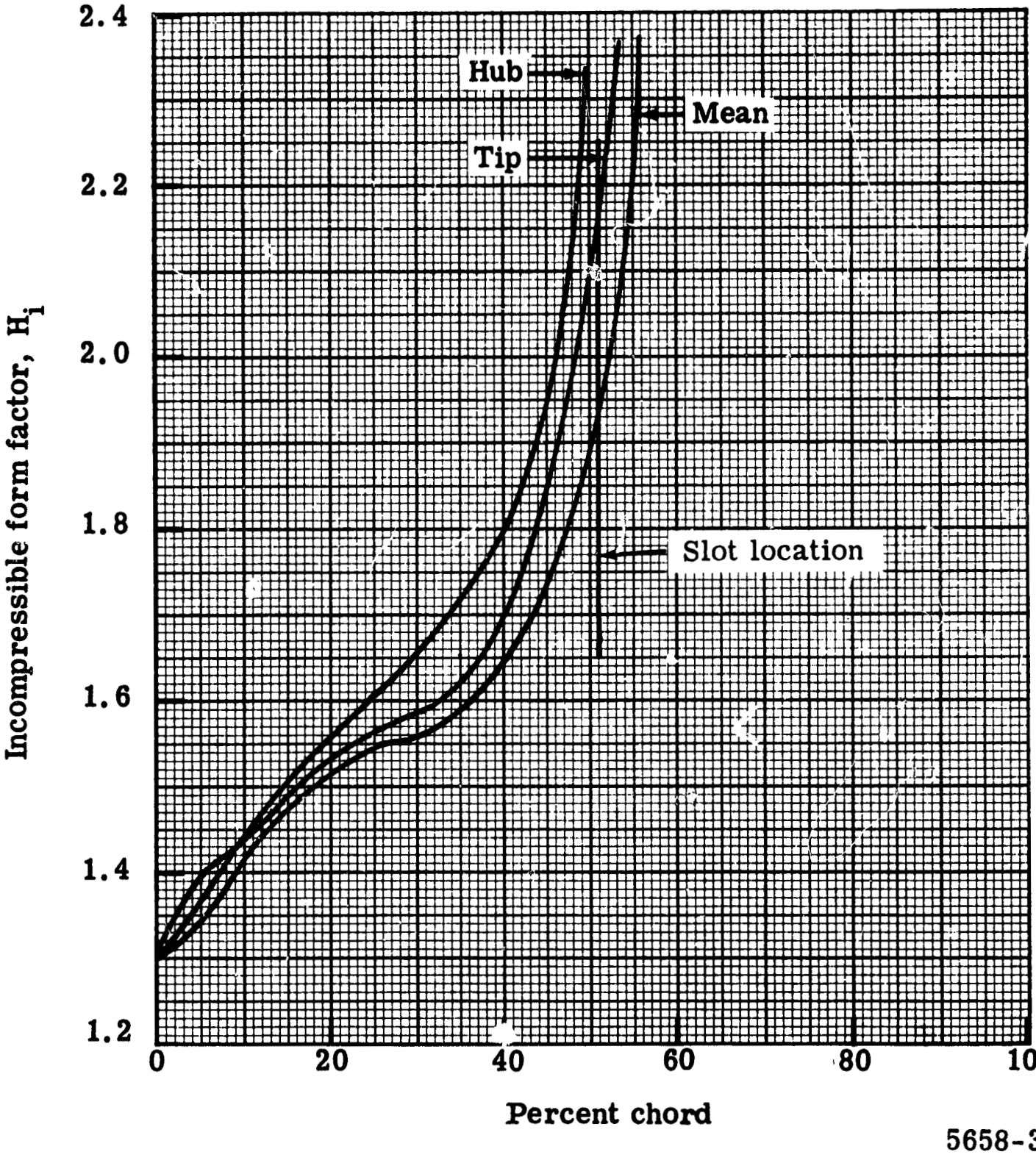

Figure 34. Incompressible boundary layer form factor for 0.75 D_f stator.

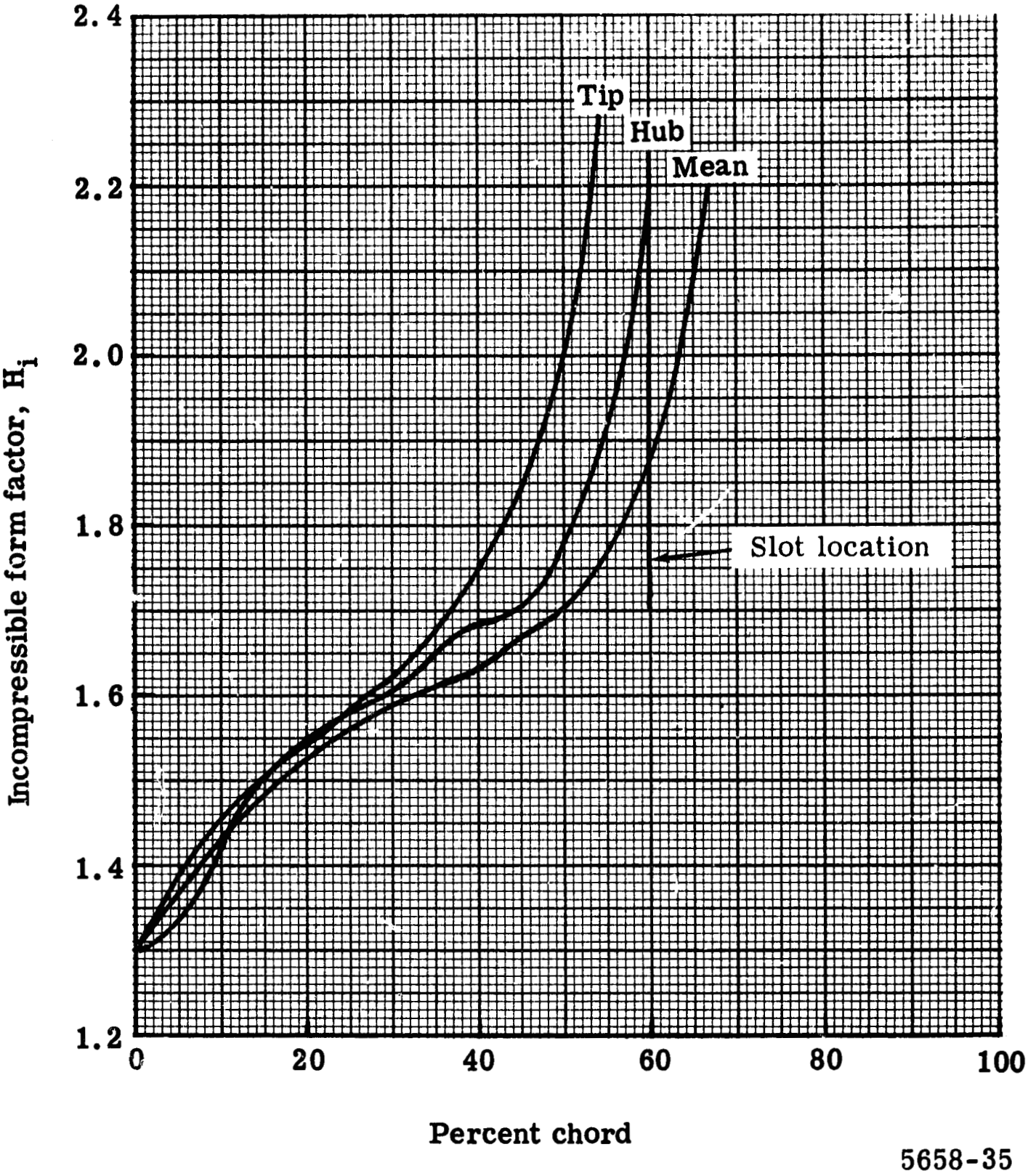

Figure 35. Incompressible boundary layer form factor for 0.65 D_f stator.

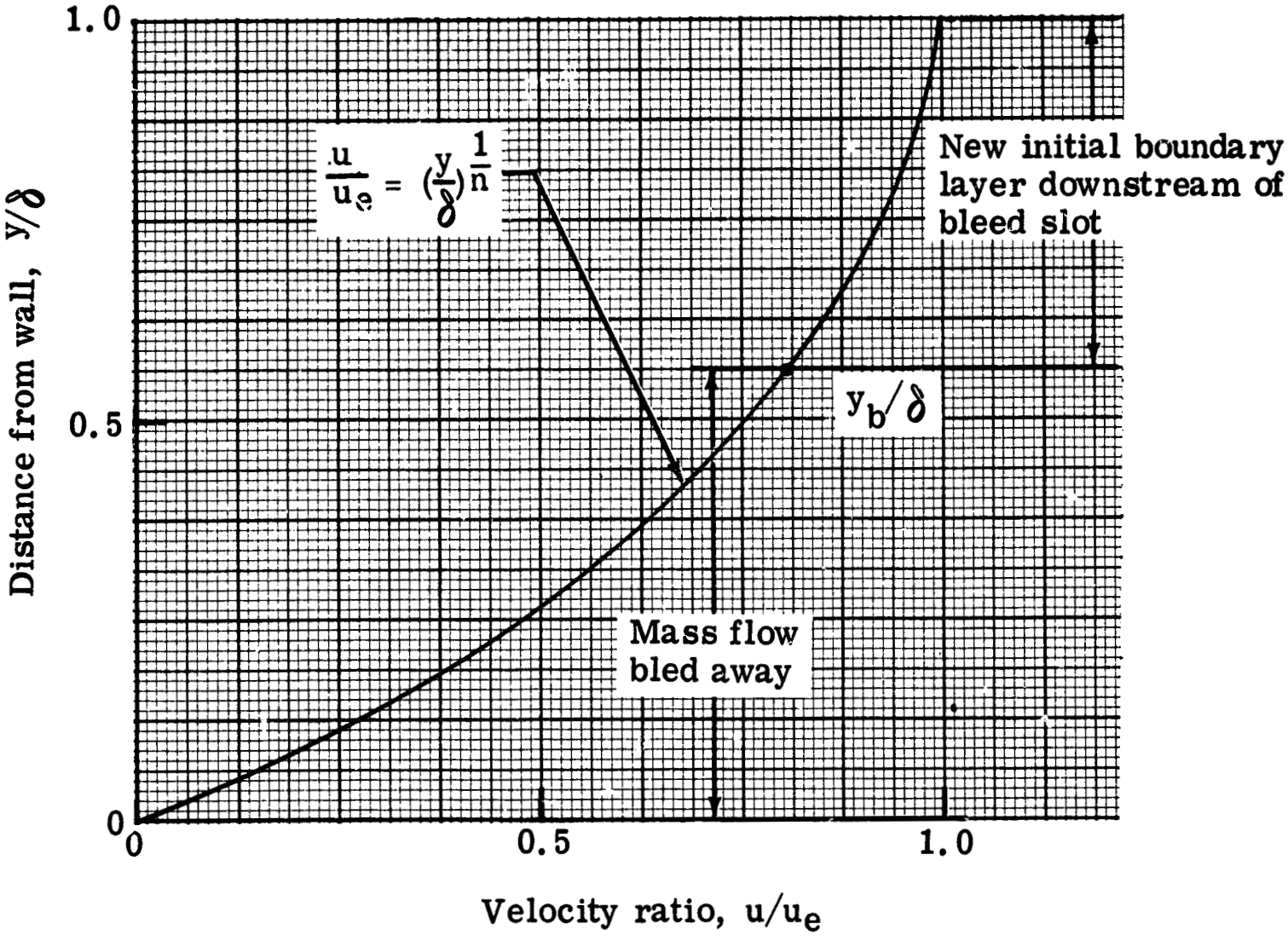

5658-36

Figure 36. Boundary layer schematic at bleed slot location.

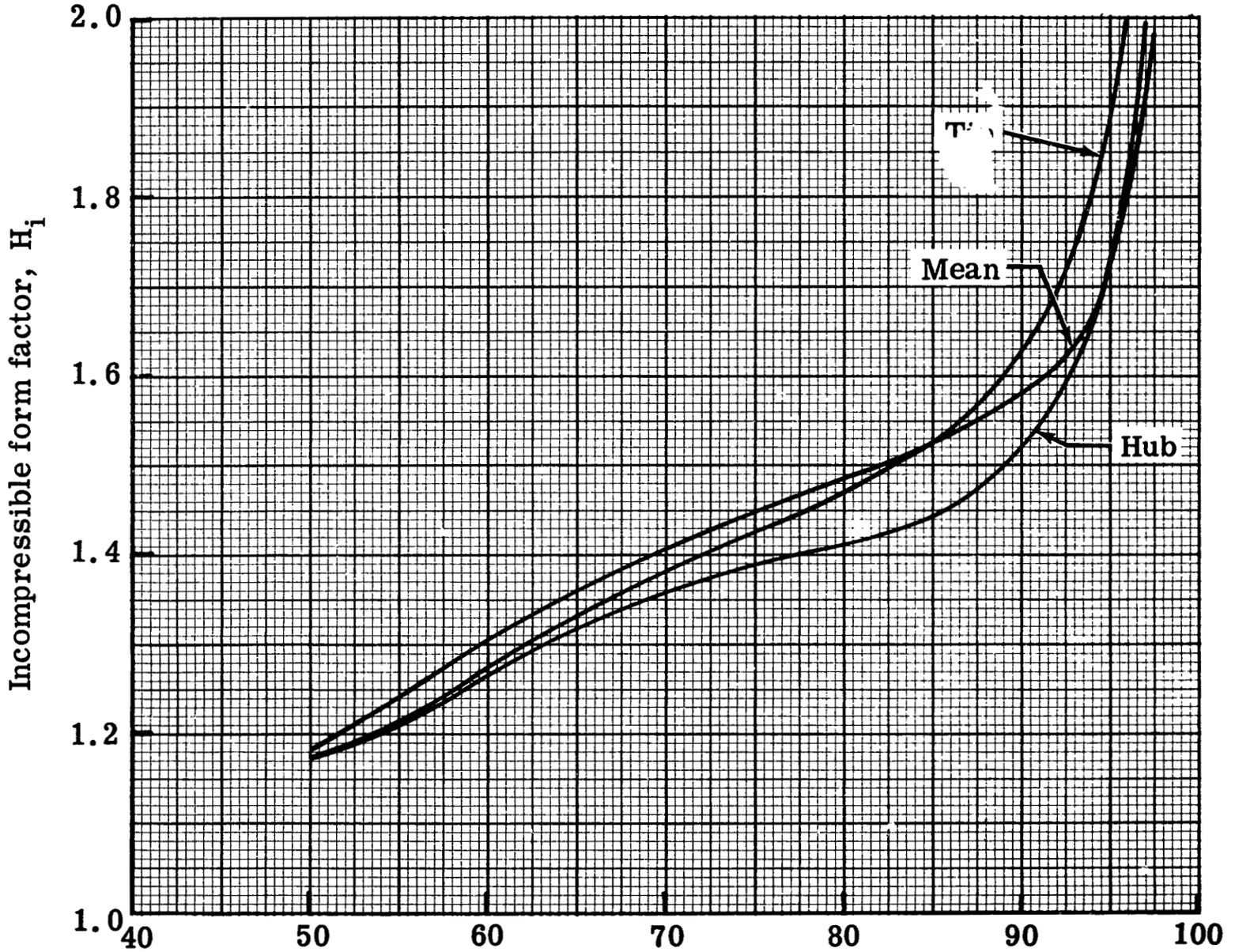

a. $(y_b/\delta) = (1/3)$

Figure 37. Incompressible form factor distribution downstream of bleed slot for 0.75 D_f stator

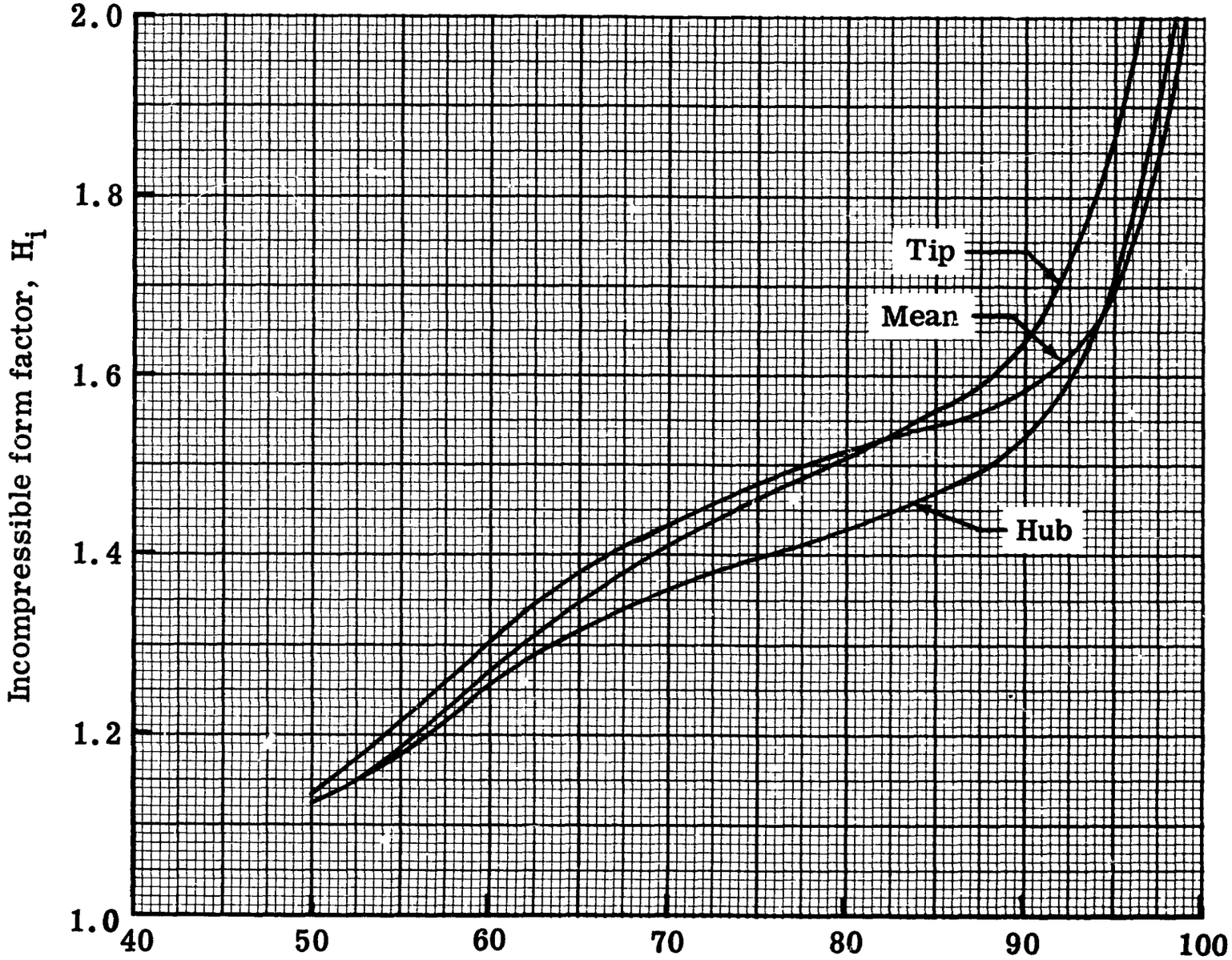

b. $(y_b/\delta) = (1/2)$

Figure 37. Incompressible form factor distribution downstream of bleed slot for 0.75 D_f stator

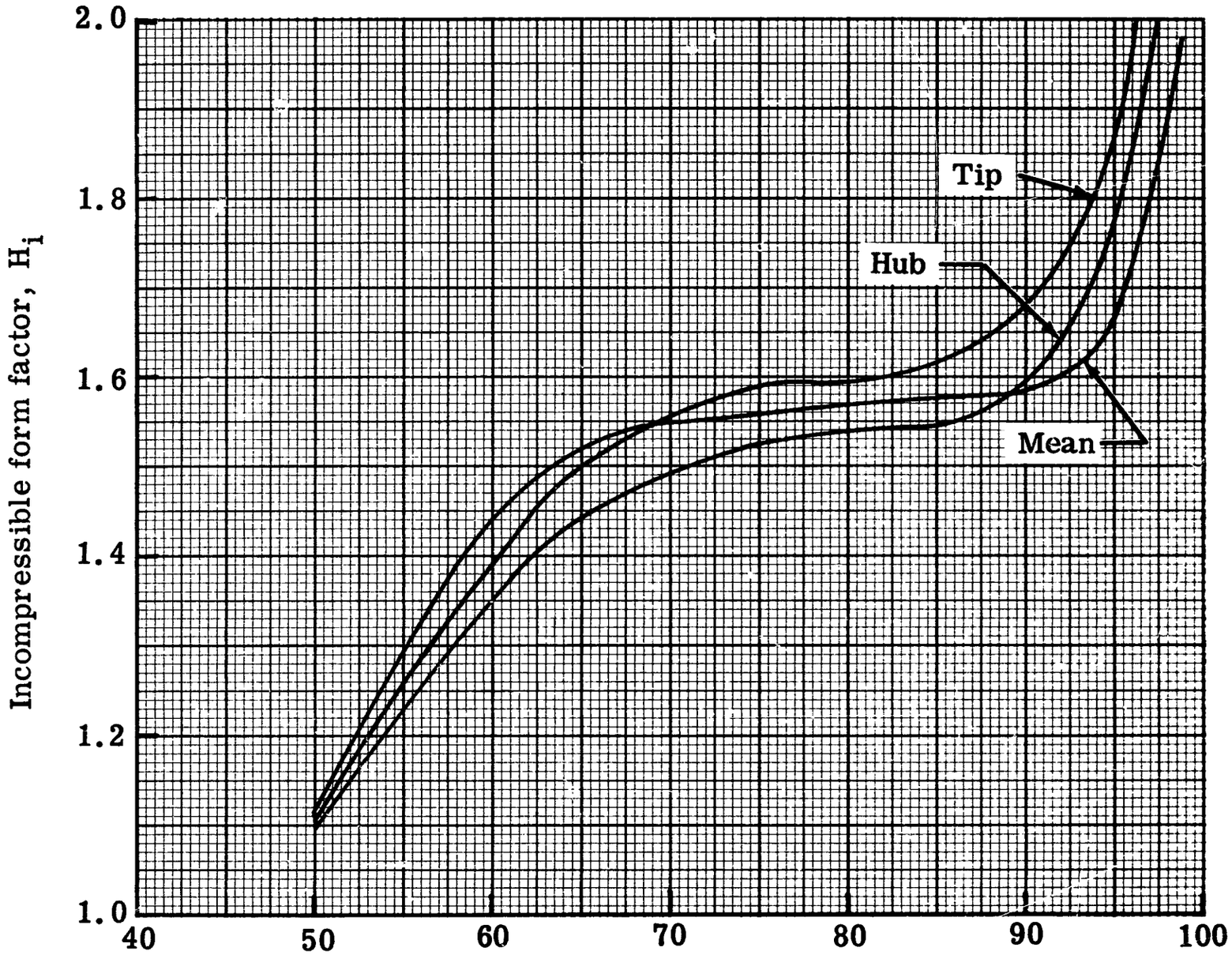

Figure 37. Incompressible form factor distribution downstream of bleed slot for 0.75 D_f stator

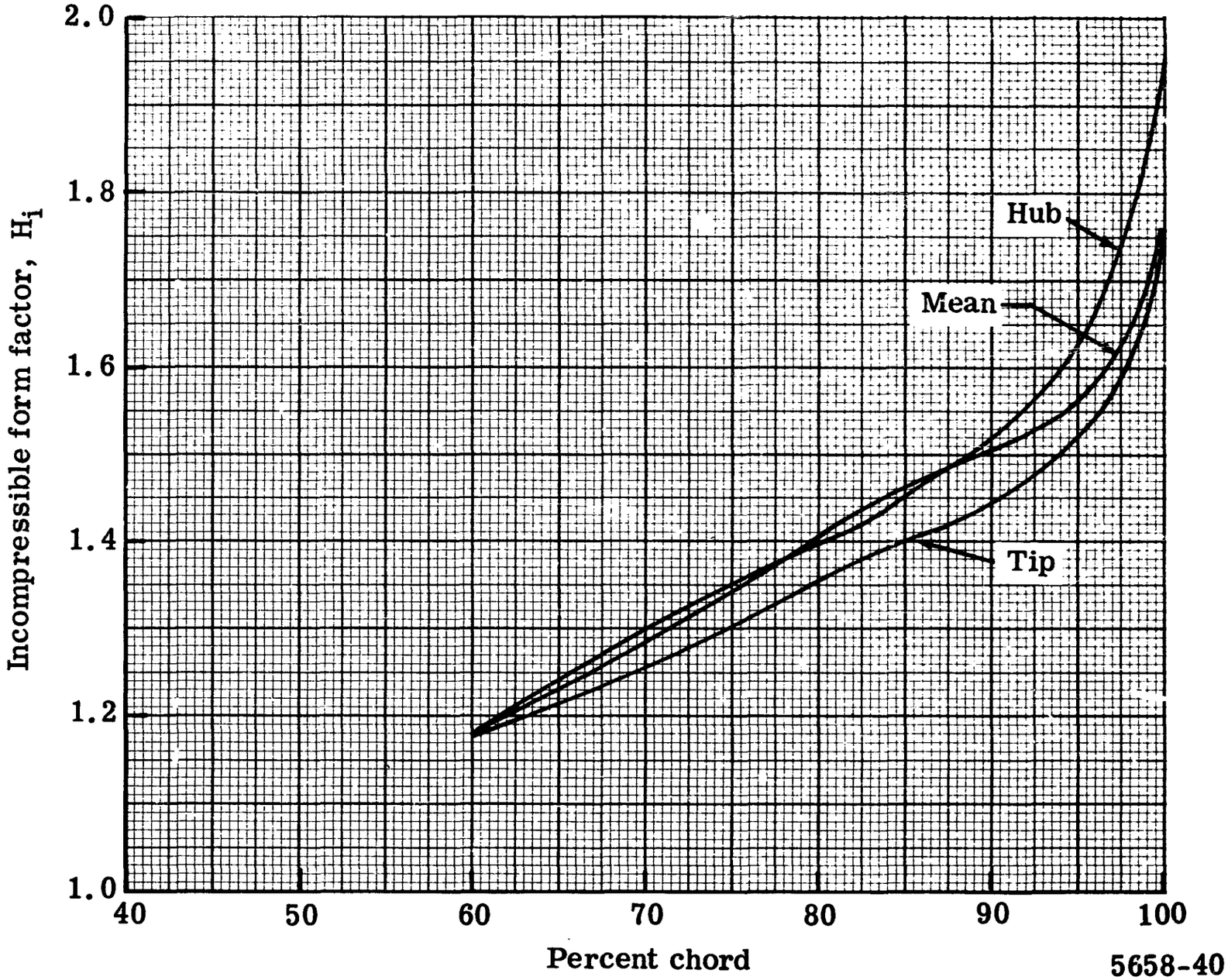

a. $(y_b/\delta) = (1/3)$

Figure 38. Incompressible form factor distribution downstream of bleed slot for 0.65 D_f stator

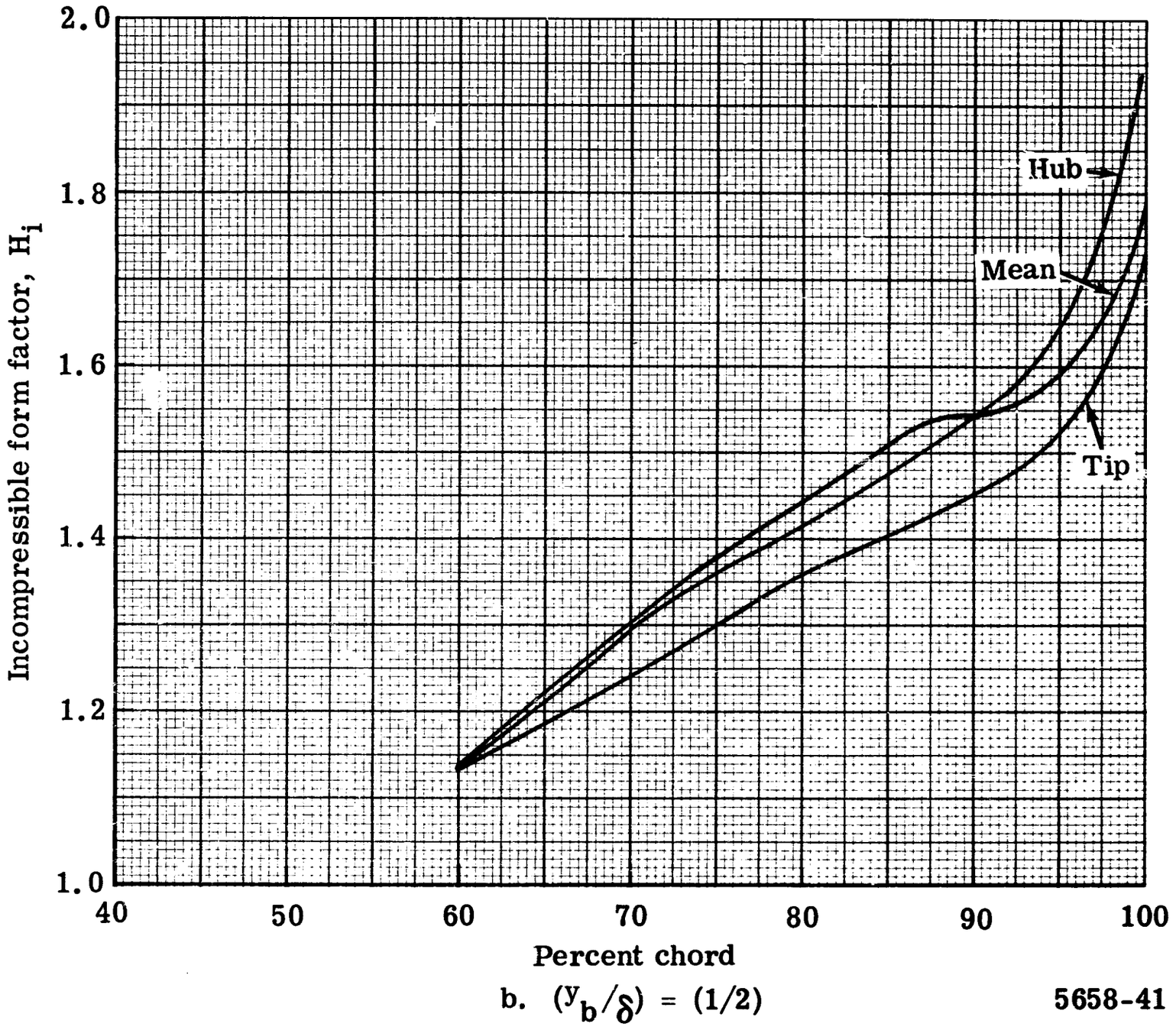

Figure 38. Incompressible form factor distribution downstream of bleed slot for 0.65 D_f stator

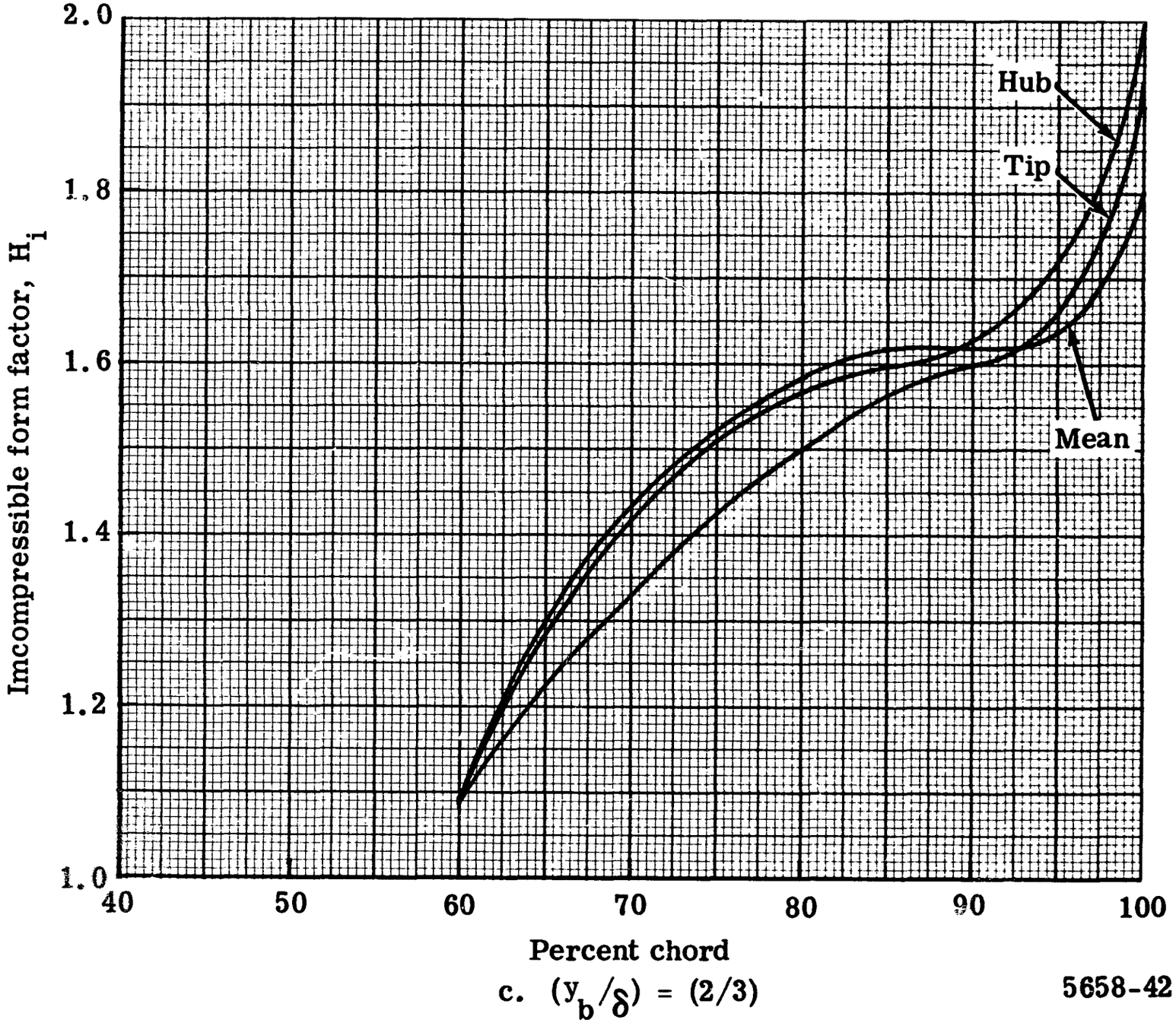

Figure 38. Incompressible form factor distribution downstream of bleed slot for 0.65 D_f stator

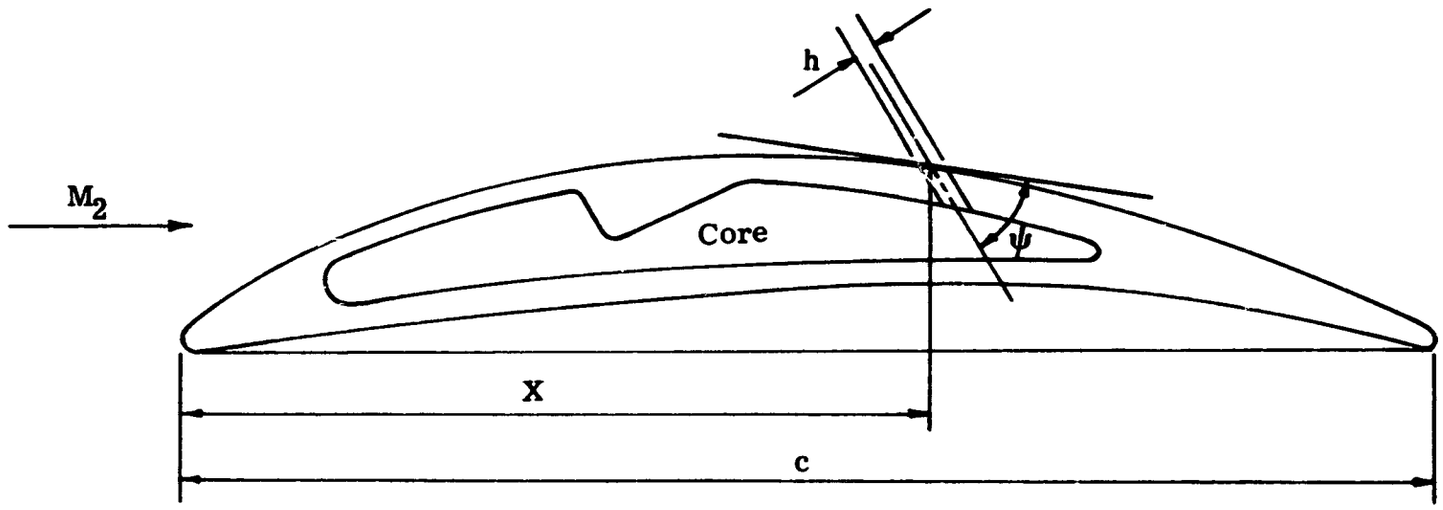

D_{f_H}	Vane	X/c (percent)	h (inches)	ψ (degrees)	$\left(\frac{\dot{m}_b n}{W_a}\right)_{max}$ (percent)	$\left(\frac{\dot{m}_b n}{W_a}\right)_{(Y_b/\delta)=0.33}$ (percent)
0.65	Single slot	60	0.030	45	2.05	1.80
0.75	Single slot	51.2	0.030	45	2.03	1.27
0.75	Triple slot	1. 25.0 2. 41.0 3. 61.0	0.009	45	1.72	1.50

5658-43

Figure 39. Schematic of slot geometry and bleed flow summary.

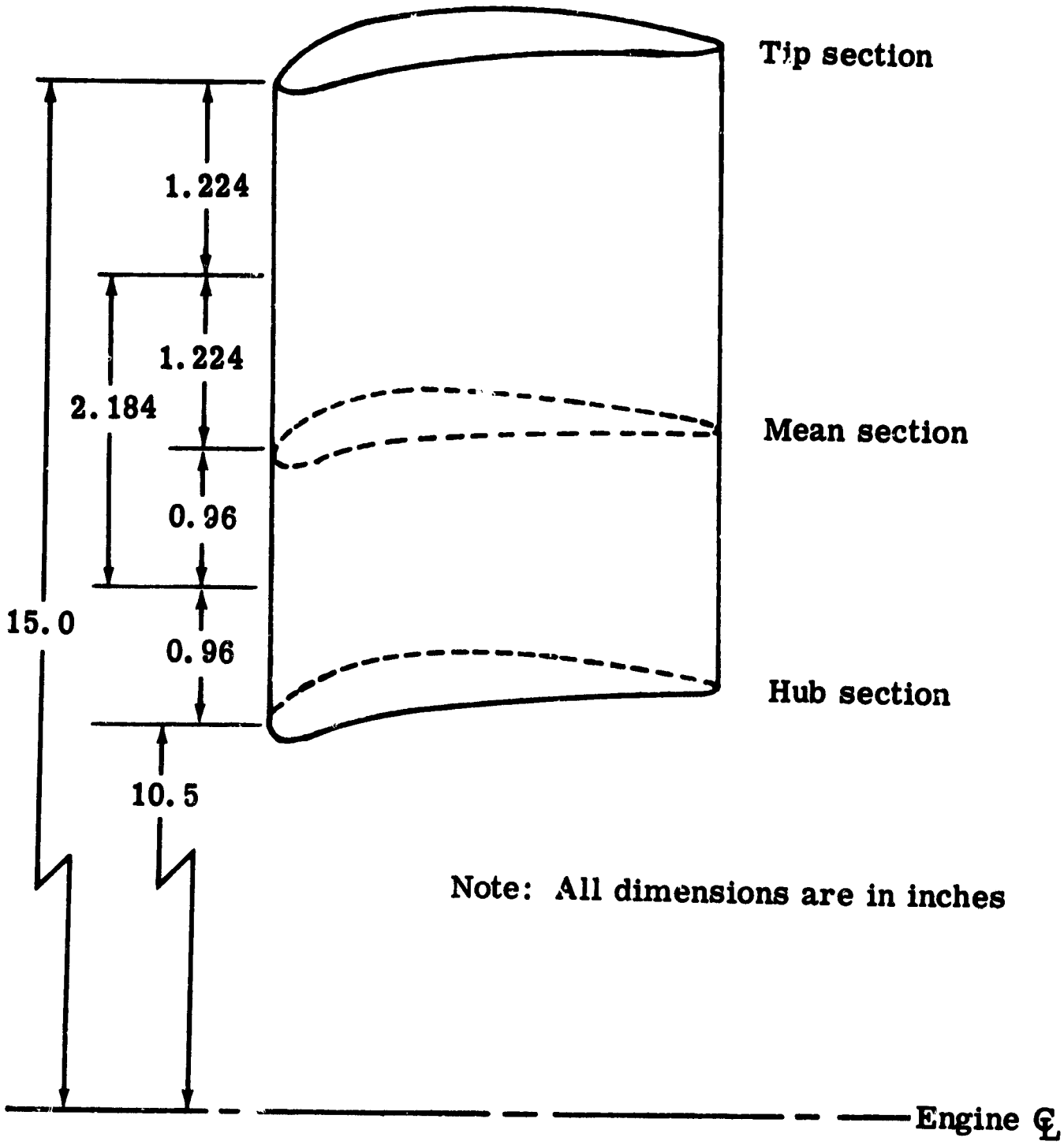

Figure 40. Portions of blade span assigned to hub, mean, and tip sections for slot calculation.

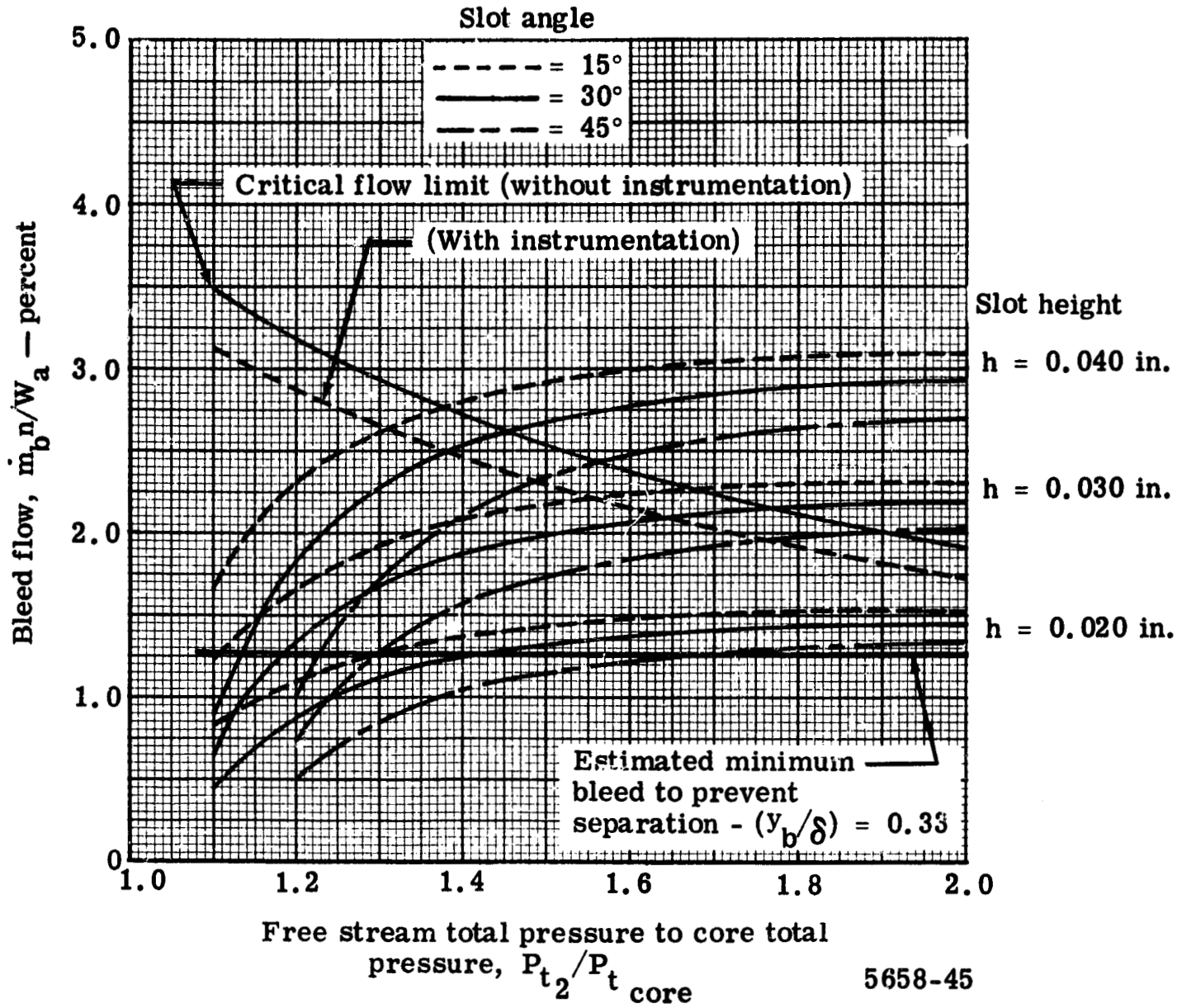

Figure 41. Single-slot bleed flow for various slot configurations for 0.75 D_f stator.

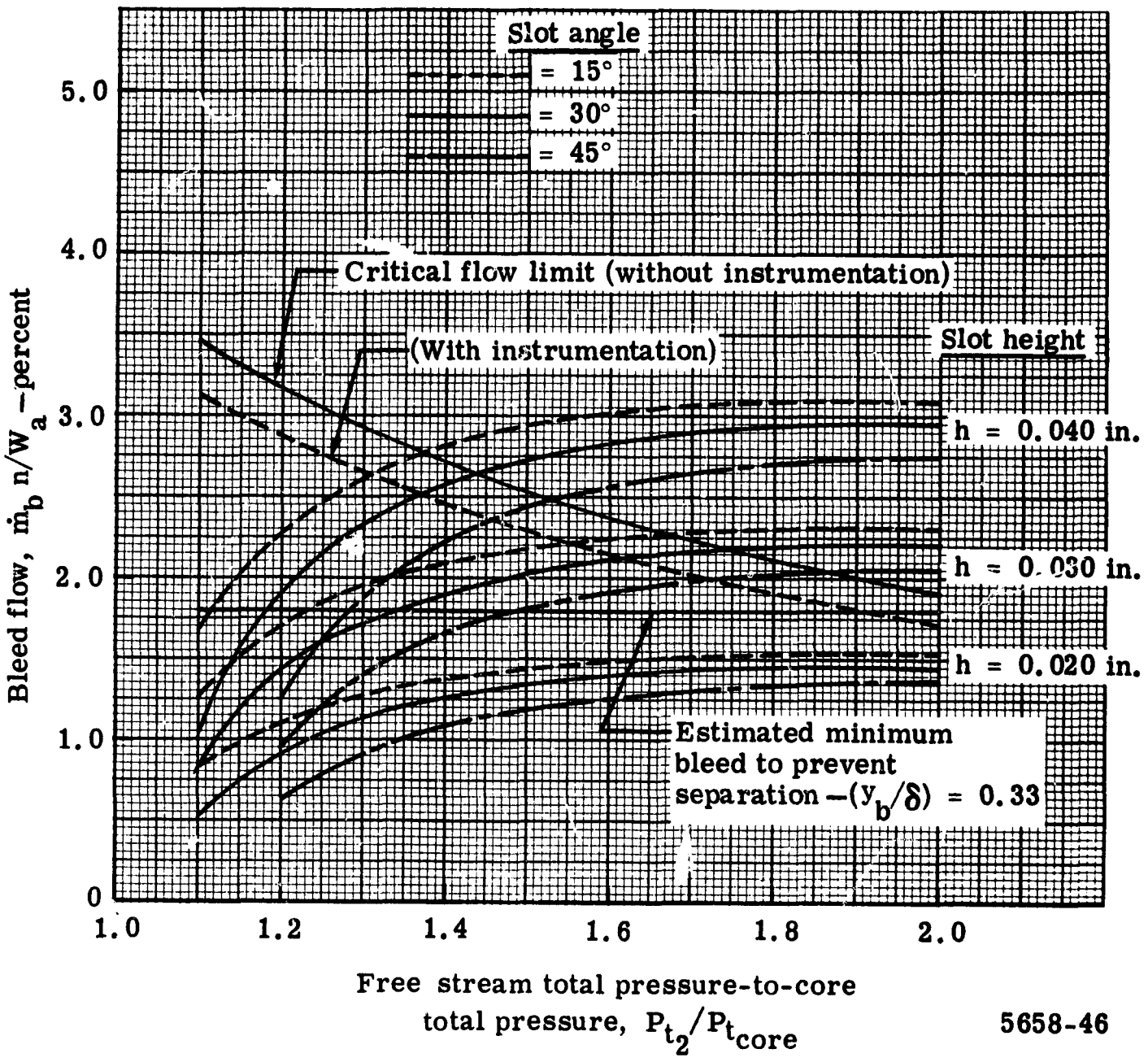

Figure 42. Single-slot bleed flow for various slot configurations for 0.65 D_f stator.

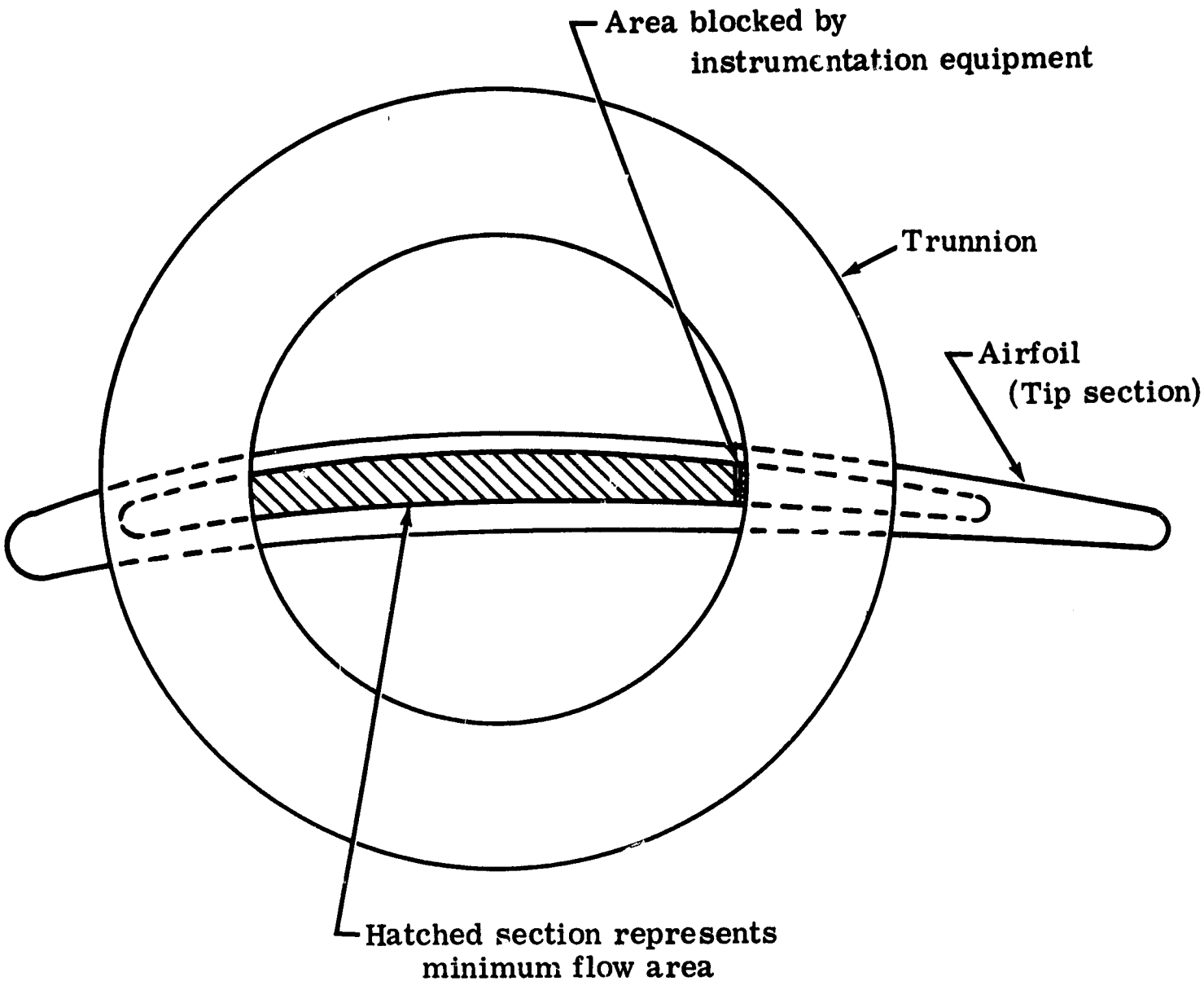

Figure 43. Schematic of minimum area in blade suction path.

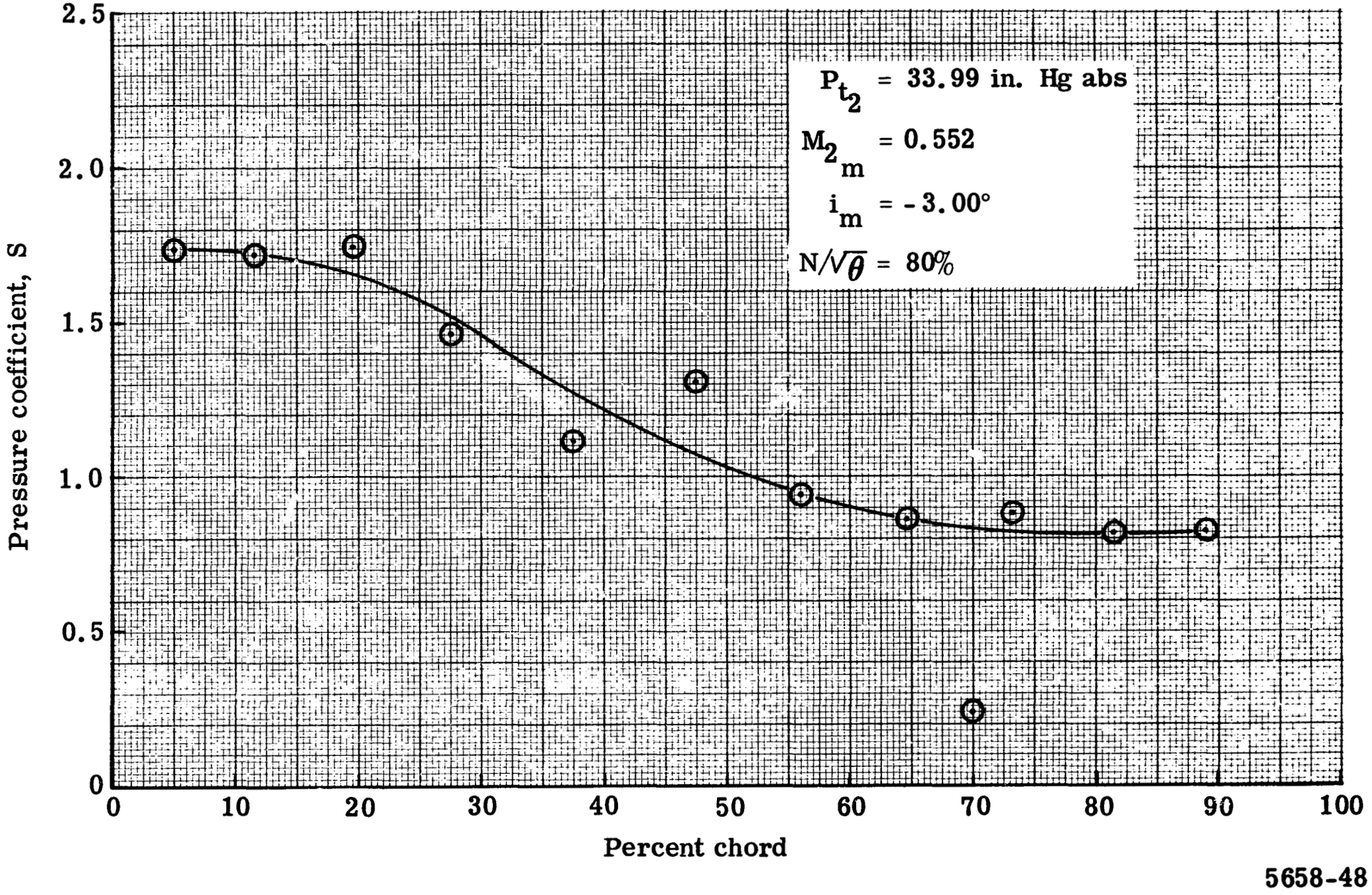

Figure 44a. Unslotted stator suction surface static pressure distribution at 80% speed and 50% streamline.

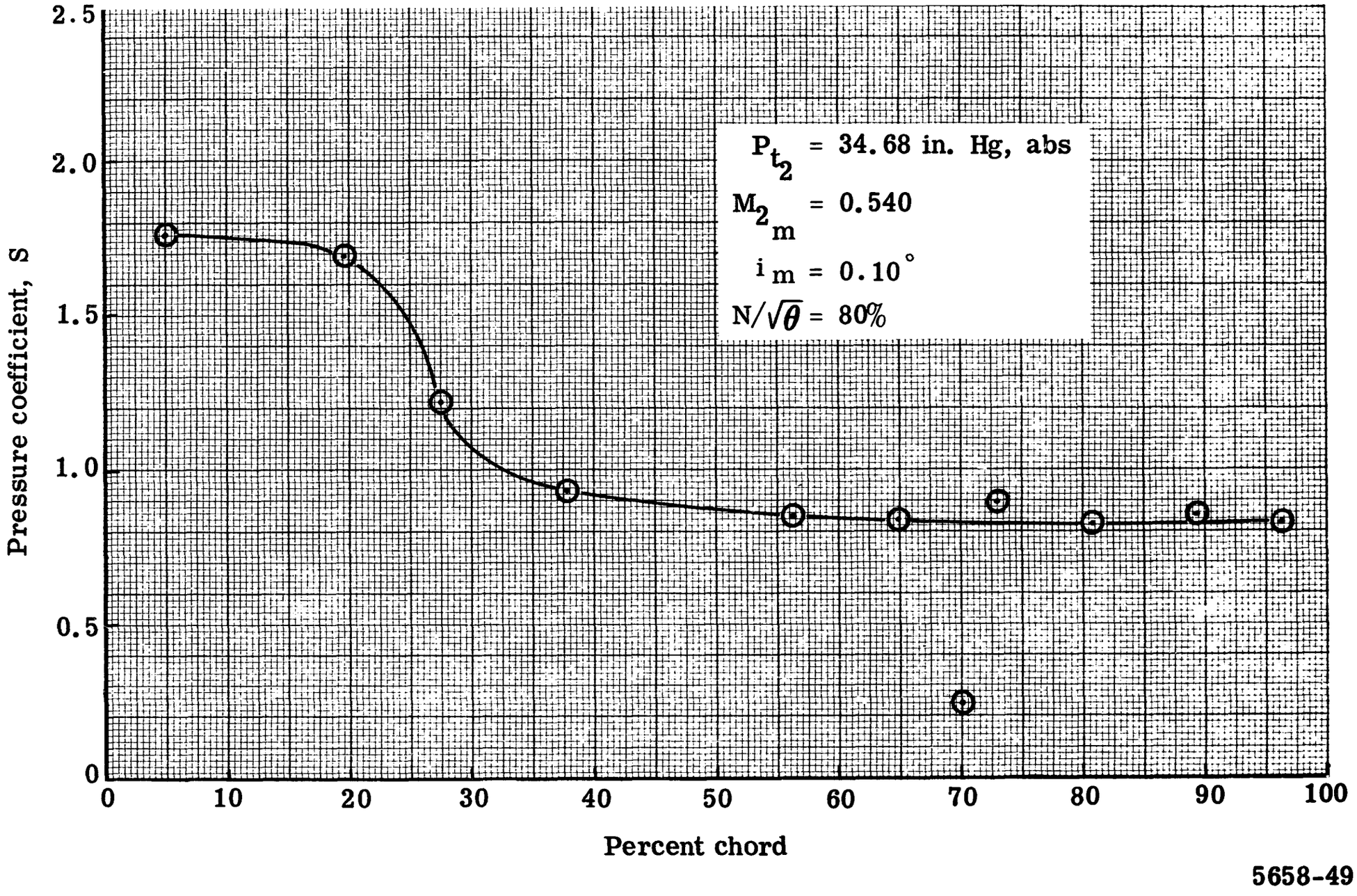

Figure 44b. Unslotted stator suction surface static pressure distribution at 80% speed and 50% streamline.

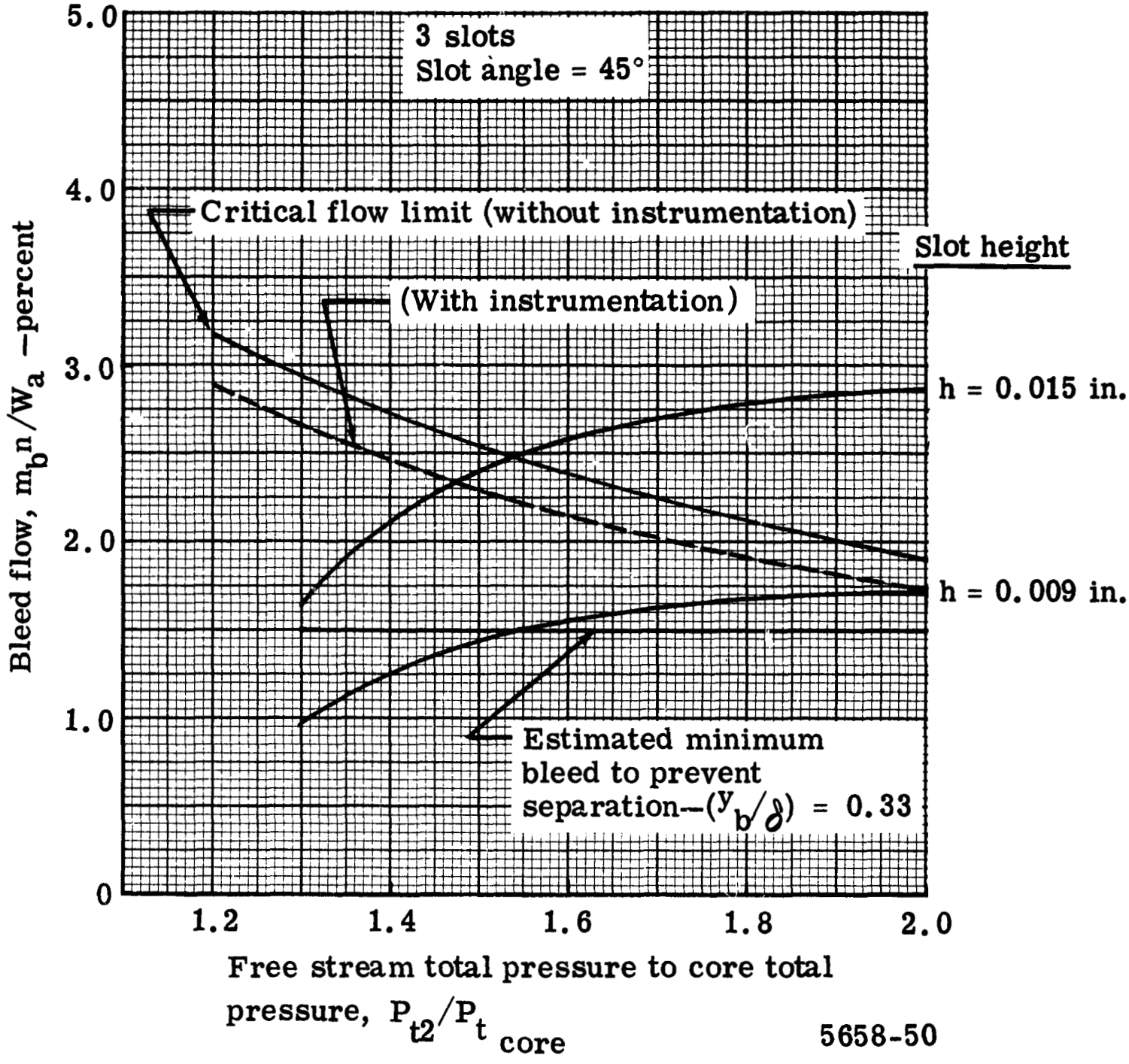

Figure 45. Triple-slot bleed flow for various slot heights for 0.75 D_f stator.

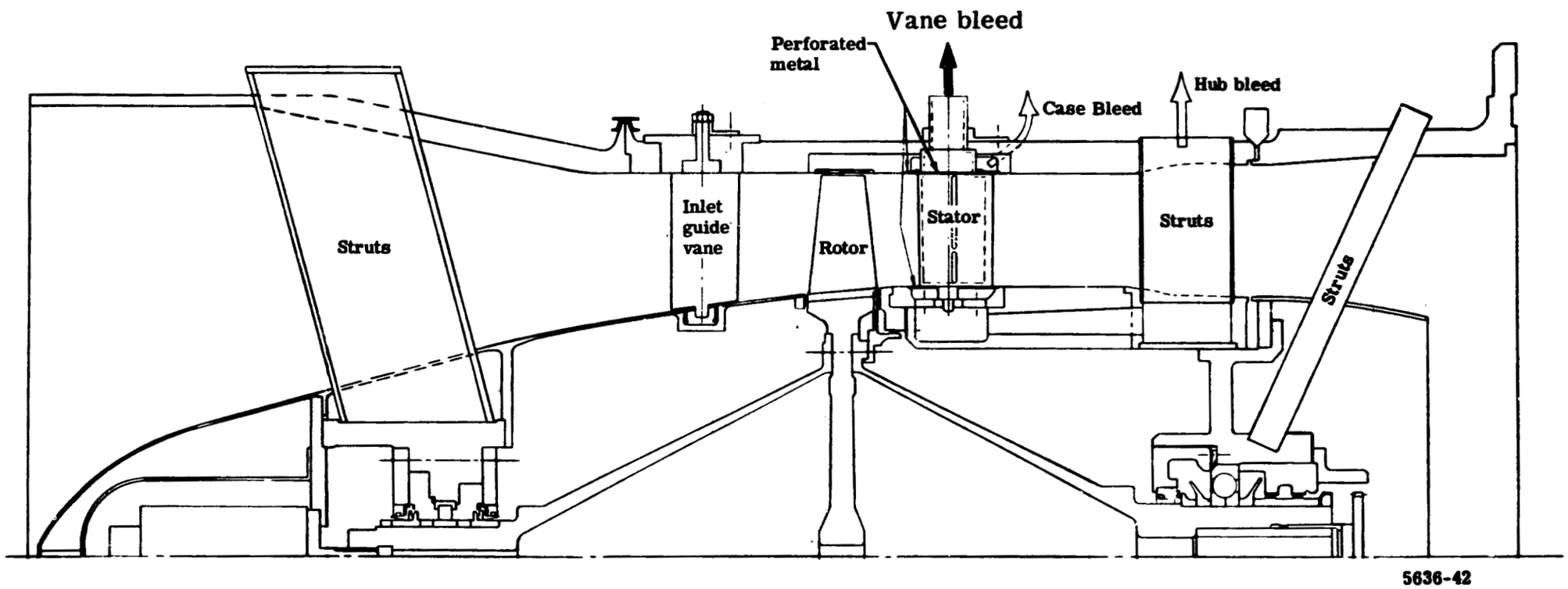

Figure 46. Layout of component test rig.

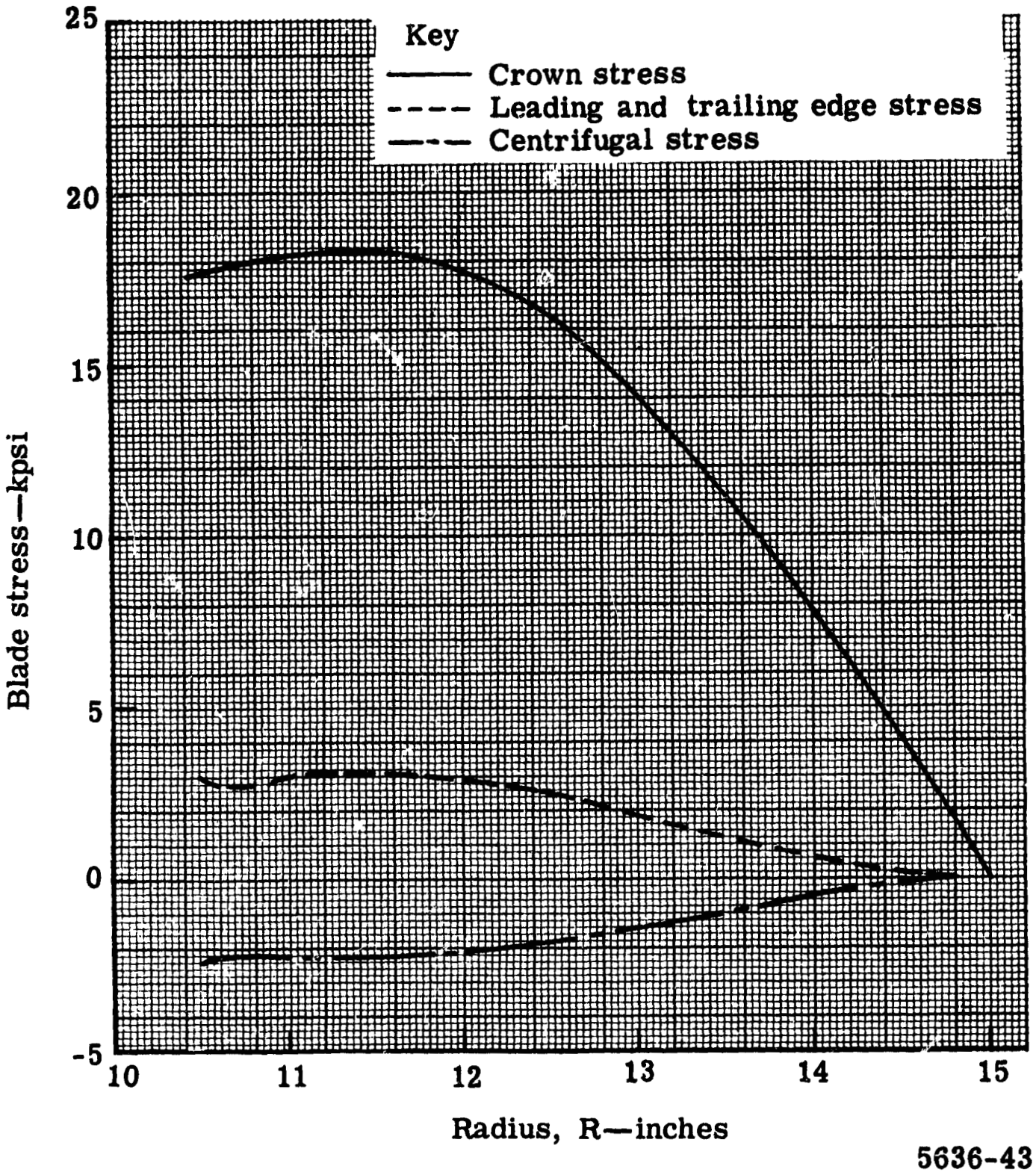

Figure 47. Rotor blade stresses.

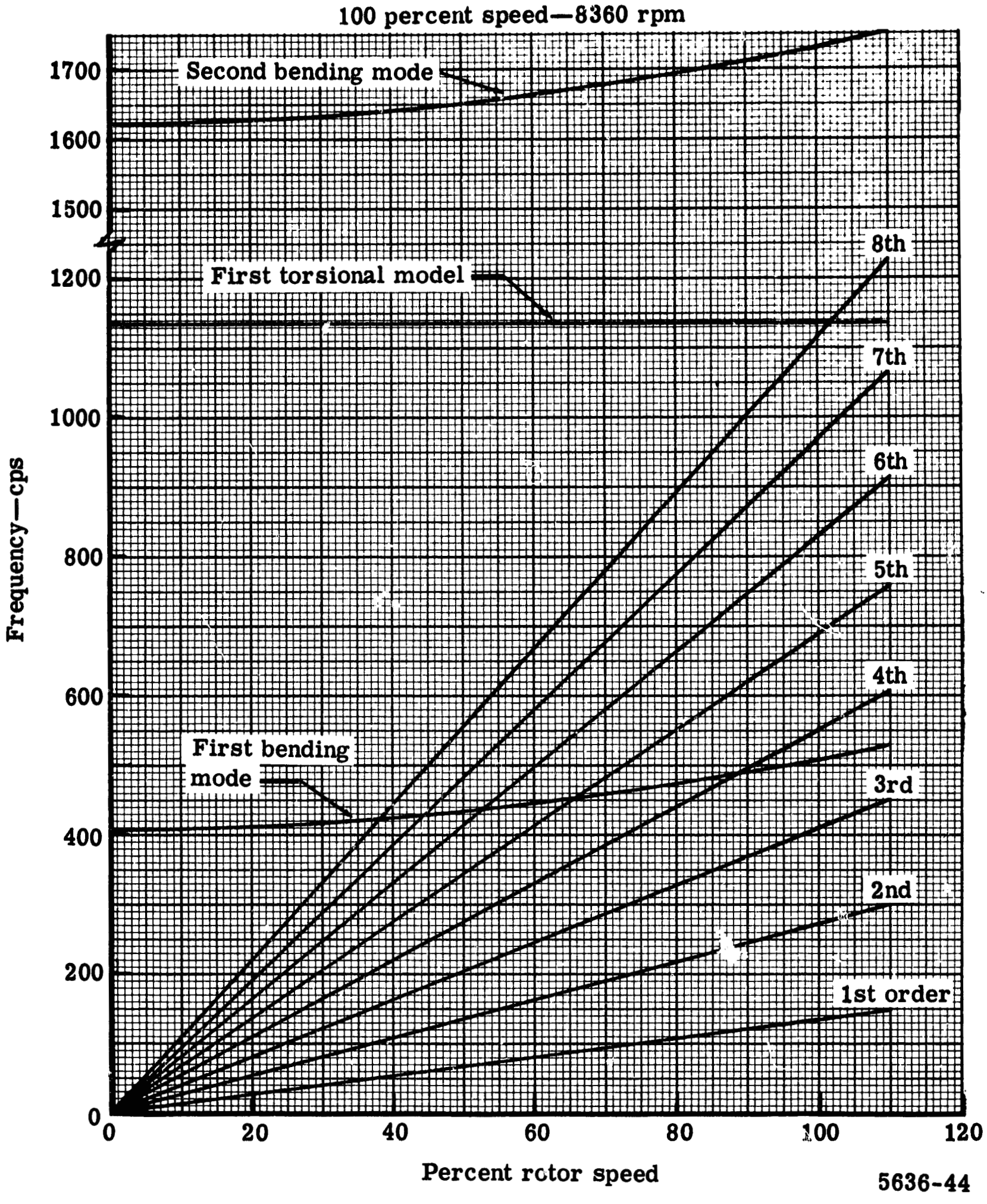

Figure 48. Rotor blade frequencies.

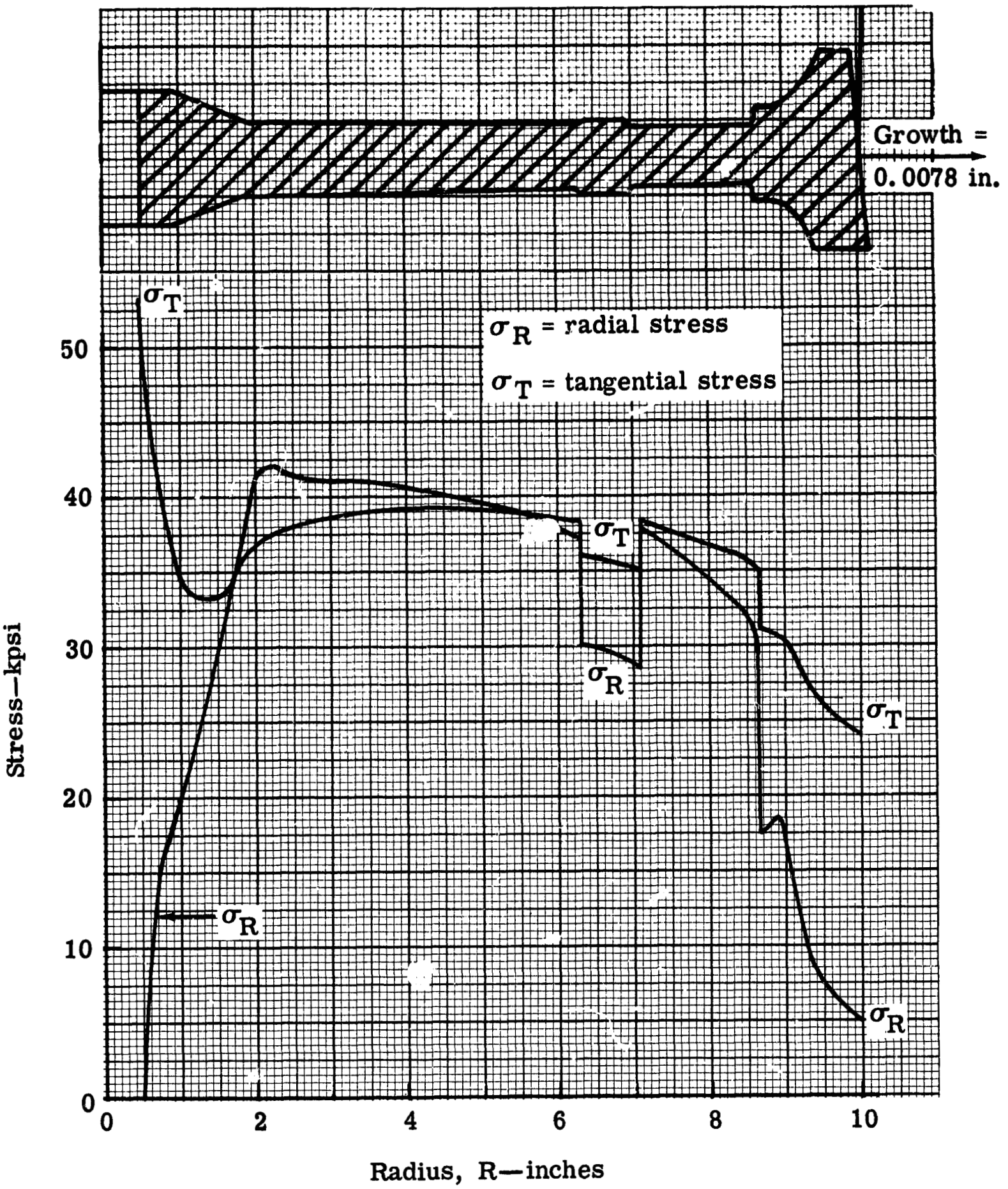

5636-45

Figure 49. Rotor wheel disk stresses at design speed.

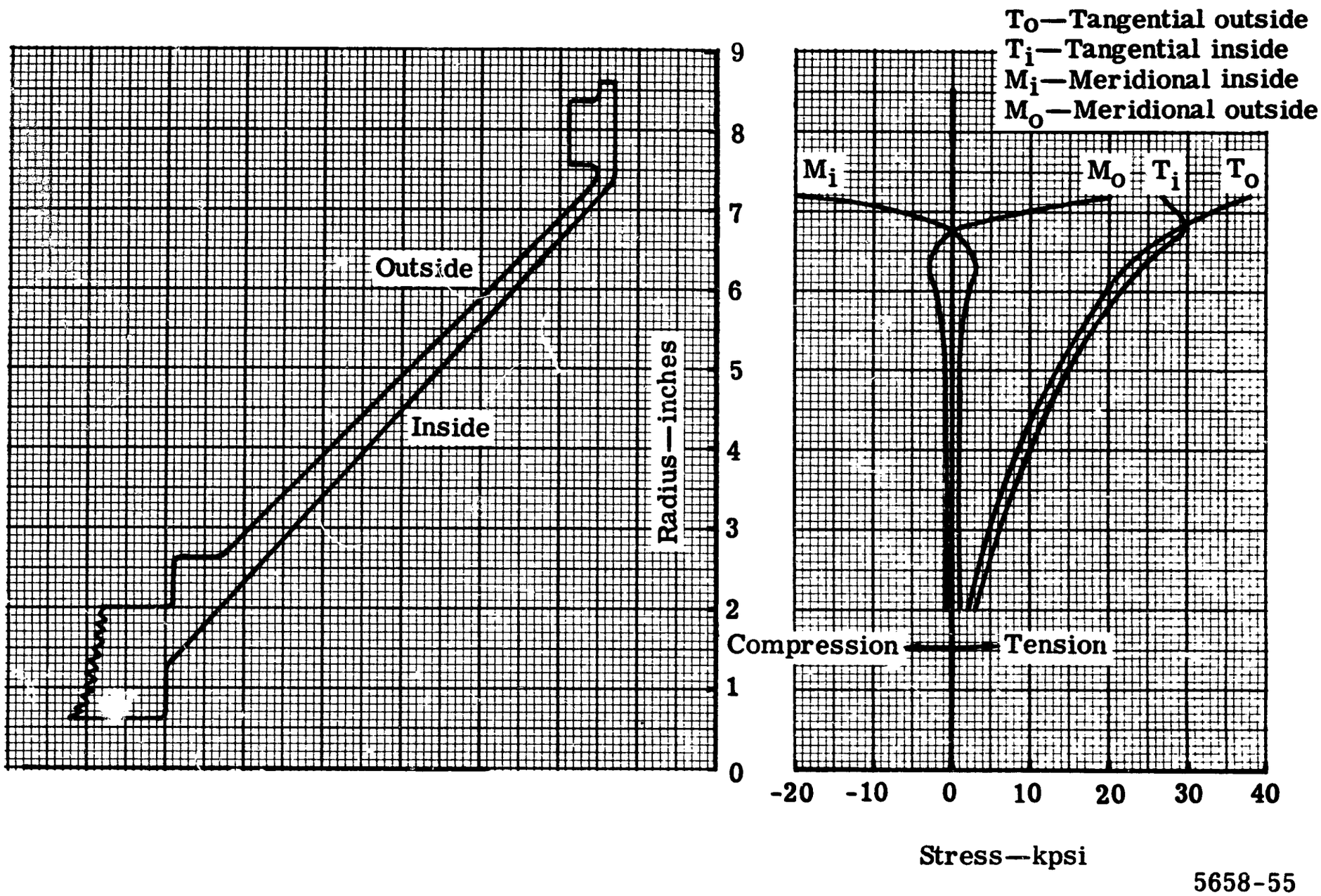

Figure 50. Coned drive shaft stresses at design speed.

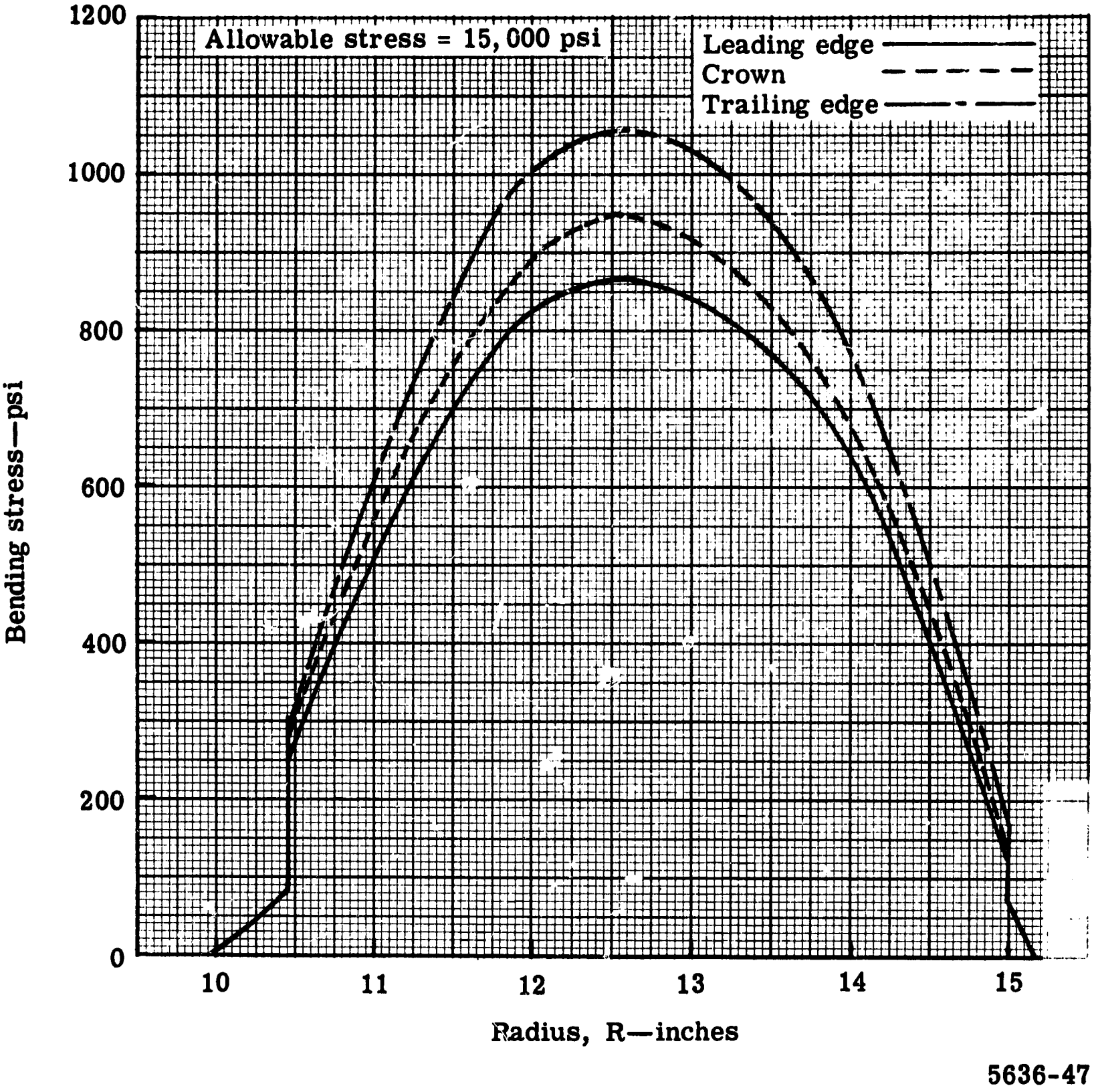

Figure 51. 0.65 hub D_f vane bending stress (unslotted and pinned).

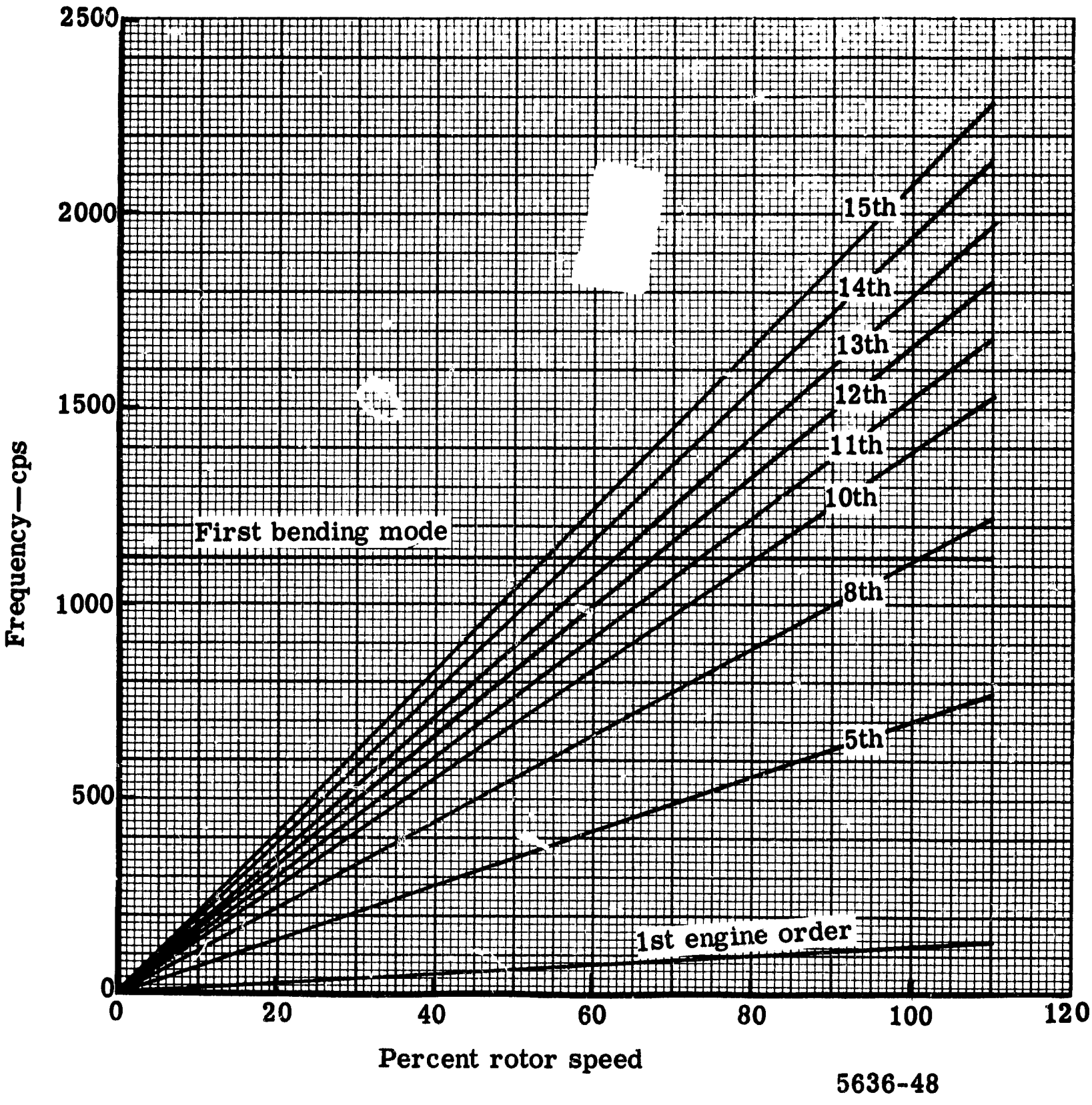

Figure 52. 0.65 hub D_f vane frequency (unslotted and pinned).

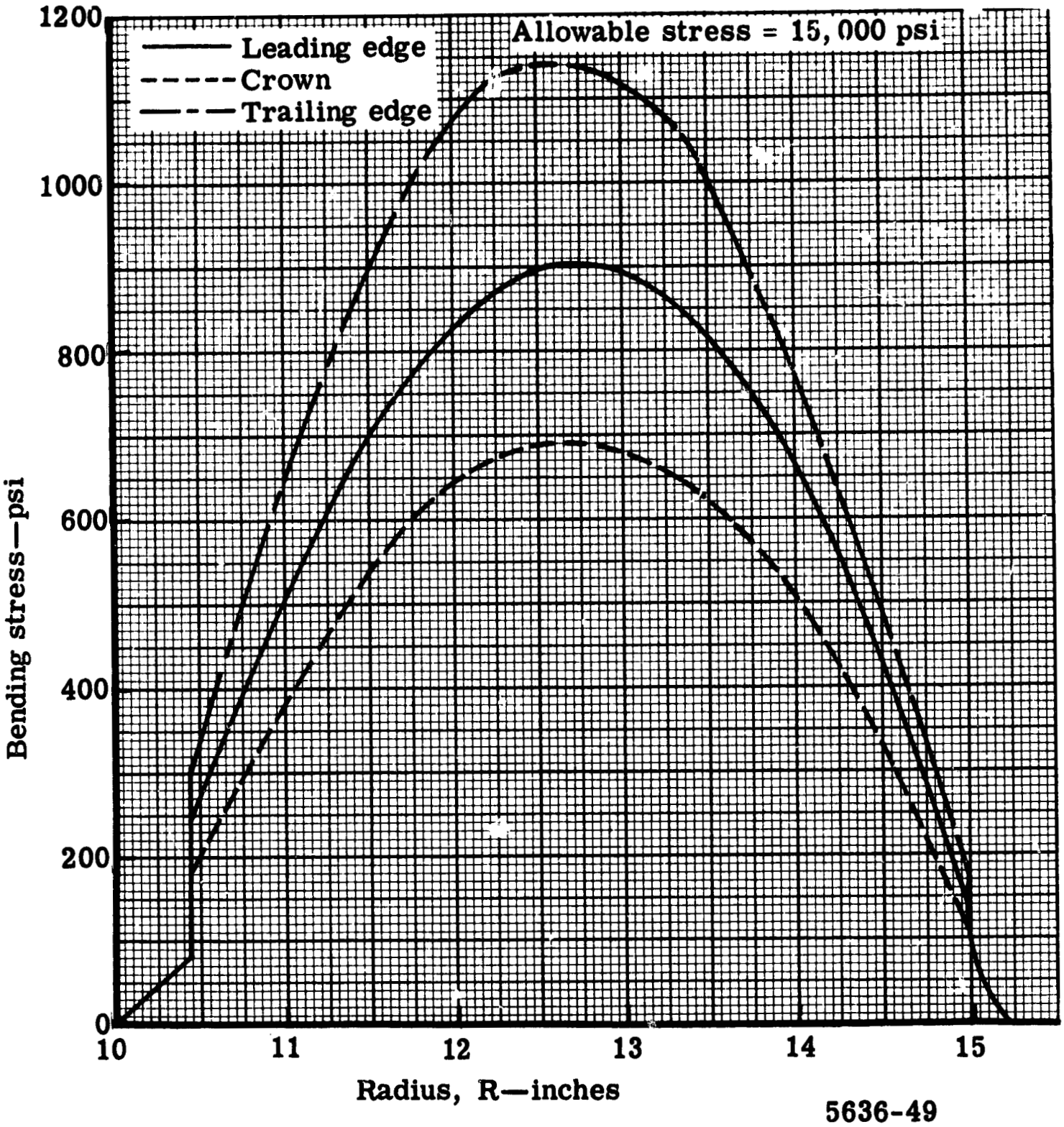

Figure 53. 0.75 hub D_f vane bending stress (unslotted and pinned).

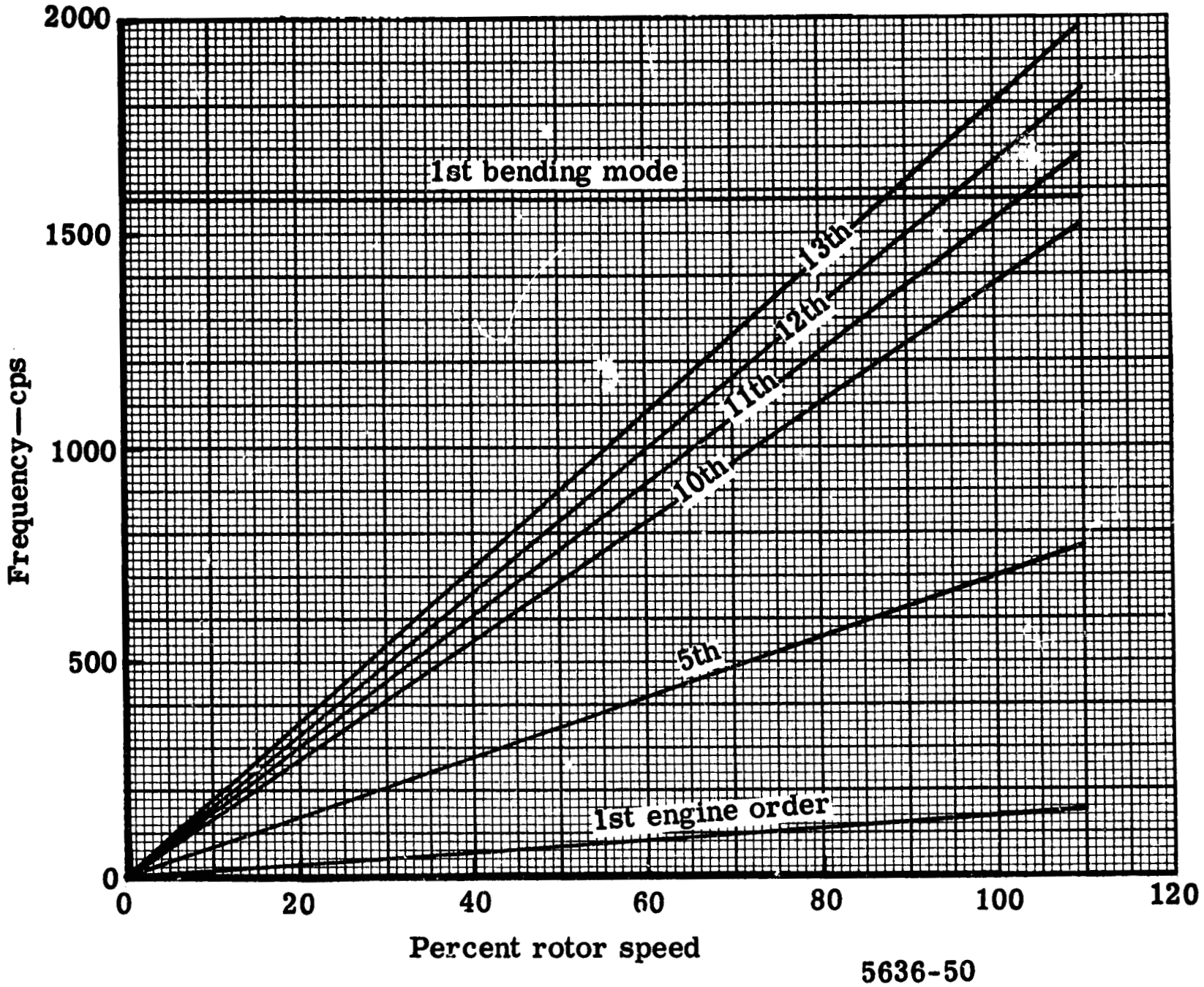

Figure 54. 0.75 hub D_f vane frequency (unslotted and pinned).

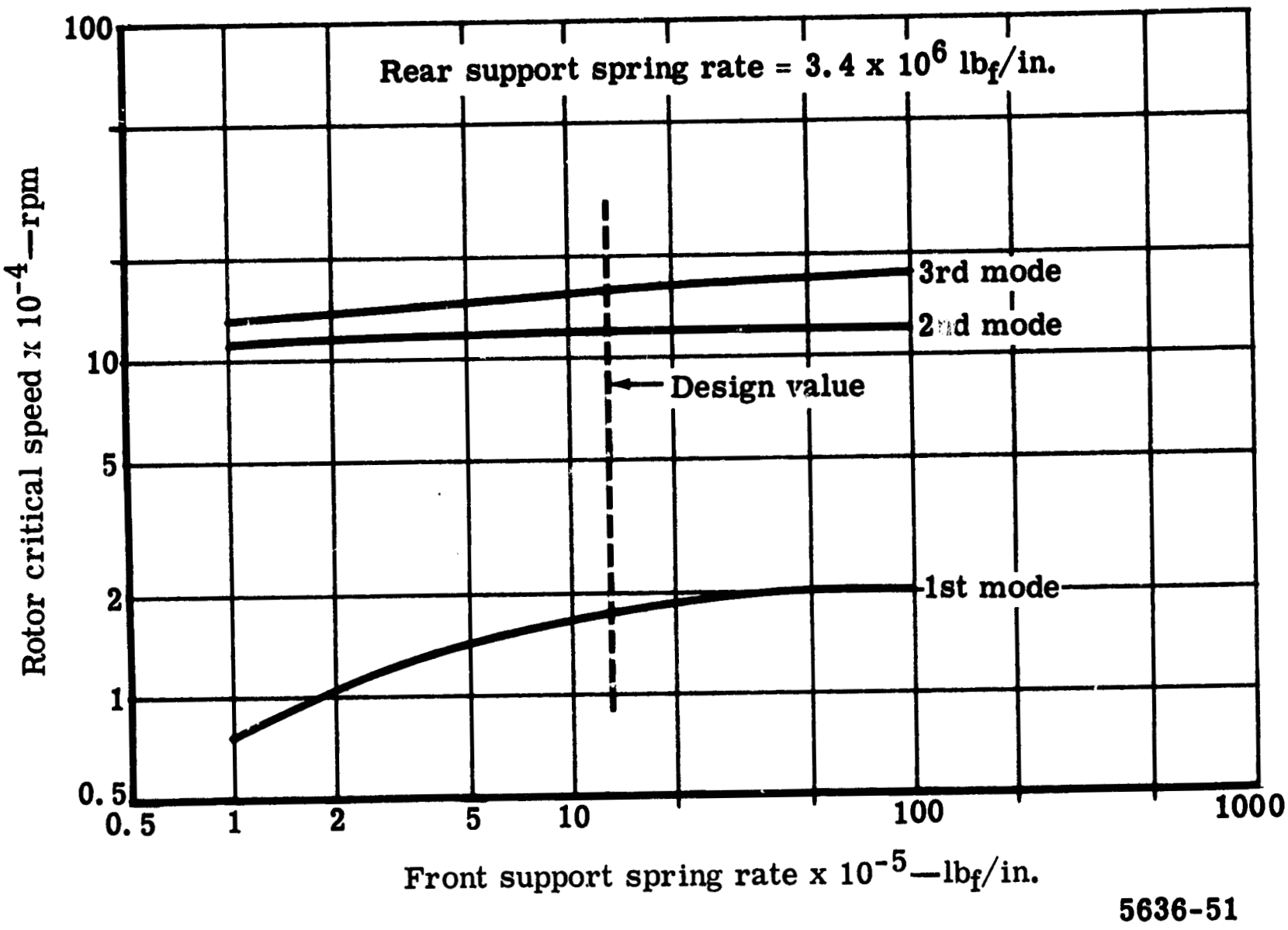

Figure 55. **Test rig critical speeds.**